Seismoelectric Modelling of the Flux-Normalized P-SV-TM Propagation Mode

Gavin Menzel-Jones

Master of Science Thesis

Delft University of Technology

Department of Geotechnology

Seismoelectric Modelling of the Flux-Normalized P-SV-TM Propagation Mode

Master of Science Thesis

For the degree of Master of Science in Applied Geophysics at Delft University of Technology

Gavin Menzel-Jones

August 23, 2011

Faculty of Civil Engineering and Geosciences · Delft University of Technology

Abstract

Elastodynamic and electromagnetic processes are coupled together in saturated, porous media, by a phenomenon known as the electrokinetic effect. In horizontally layered media, the seismoelectric system, which contains the coupled elastodynamic and electromagnetic systems, can be separated into two independent modes of propagation: SH-TE and P-SV-TM. The SH-TE mode contains horizontally polarized shear waves coupled with transverse electric polarized electromagnetic waves. In the P-SV-TM mode, both fast and slow compressional waves are coupled with vertically polarized shear waves and transverse magnetic polarized electromagnetic waves. In this thesis, the P-SV-TM mode of the two-dimensional seismoelectric system was expressed in the form of both the two-way and one-way wave equations. The principle of normalizing energy flux across boundaries was applied, improving the matrix amplitude balance of the system and allowing for the implementation of one-way reciprocity theorems.

We carried out full-waveform modelling of the flux-normalized P-SV-TM seismoelectric system in a 2-D fluid-saturated, horizontally-stratified, porous media. Both one-way and two-way wavefields were modelled, allowing the composition of one-way wavefields into two-way wavefields to be clearly observed. We investigated both the generation of electromagnetic fields due to the propagation of a seismic pertubation and the generation of seismic waves due to the propagation of a diffusive electromagnetic wave. Reciprocity of the wavefields was verified by applying reciprocity theorems to both one-way and two-way wave vectors.

The electromagnetic field that is created when a seismic wave traverses a contrast in medium parameters is rapidly attenuated during propagation. To mitigate the decay in the amplitude of the signal with distance, we modelled a Vertical ElectroSeismic Profiling (VESP) survey, in which receivers could be placed in near proximity to the target layer. In another model, the sensitivity of the seismoelectric method to pore fluid contrasts was tested by simulating the influx of contaminants into an aquifer. It was observed that a small change in the conductivity of the aquifer led to a significant change in the strength of the electromagnetic signal that was generated at the top of the aquifer.

Table of Contents

List of Figures

List of Tables

Acknowledgements

I would like to thank my supervisor Niels Grobbe for always being willing to assist throughout the length of the project. This manuscript benefited from his numerous corrections and suggestions. I would also like to acknowledge Sjoerd de Ridder, who provided the seismoelectric SH-TE modelling code that formed the basis for the P-SV-TM modelling that was carried out in this thesis. The project would certainly not have been possible without Evert Slob, who proposed the topic and provided invaluable guidance throughout it.

I would like to pass on my gratitude to the organizers of the IDEA League Joint Master's in Applied Geophysics program. This Master's program was truly a unique experience that exposed us to a diverse range of material at three European universities. Almost as importantly, it introduced me to people who I would never otherwise have had the pleasure and fortune of meeting. Numerous names come to mind, but especially Dennis, Mengmeng, Jon, Moritz, Gia, and Sara. I gratefully acknowledge the scholarship from Shell/Statoil that helped make my participation in this program possible.

The final thanks is reserved for my family. My parents, my brother, and my sister have unwaveringly supported and encouraged me as I progressed through my studies. Although their presence was too seldom physical, they were never far from mind.

Delft University of Technology — Gavin Menzel-Jones
August 23, 2011

“In every branch of knowledge the progress is proportional to the amount of facts on which to build, and therefore to the facility of obtaining data.”

— *James Clerk Maxwell*

Chapter 1

Introduction

1-1 Motivation

Geophysics is a multifaceted discipline that combines a range of scientific fields to obtain detailed information on the Earth's structure. The specific geophysical method that is applied is determined by the physical properties of the target area. Naturally, a given medium parameter can only be resolved when it has an influential effect on the acquired data. There is consequently a continual search for new tools to probe previously unstimulated media parameters of the subsurface. The seismoelectric method is one such tool that takes advantage of subsurface coupling between seismic and electromagnetic waves.

It has been known since the 1930s (Thompson, 1936) that seismic and electromagnetic waves can be coupled in a fluid-saturated porous subsurface, a phenomenon called electrokinetic coupling. More recently, it was shown that the coupling occurs via a coefficient that is controlled by a range of subsurface parameters (Pride, 1994). Numerous potential applications of seismoelectrics have been suggested to take advantage of the additional information provided by both the sensitivity of the coupling coefficient to various subsurface parameters and the creation of an independent electromagnetic wave from a seismic wave, and vice versa. The sensitivity of seismoelectrics to permeability and fluid chemistry properties would make it possible to distinguish interfaces that would otherwise be overlooked (Haines et al., 2007). For example, its strong sensitivity to viscosity contrasts could be applied to the detection of gas-water contacts. Other uses would be in the detection, characterization and monitoring of aquifers (Garambois and Dietrich, 2002). Work by Haines and Pride (2006) has numerically shown that the seismoelectric method is capable of resolving layers that are significantly smaller than the seismic wavelength.

The potential applications and limitations of the seismoelectric method can best be examined by numerical modelling. This thesis builds upon work done by De Ridder (2007) on the SH-TE propagation mode of seismoelectric fields in a horizontally layered earth. The aim of this thesis is to numerically simulate the propagation of the other mode present in the seismoelectric system of a layered earth, the P-SV-TM mode, and address some of the potential applications of the seismoelectric method.

1-2 Seismoelectric coupling

Frenkel (1944) was the first to postulate equations relating the generation of an electrical signal from a seismic source. However, it was not until Pride (1994) that a complete set of macroscopic governing equations describing the coupling between electromagnetic and elastodynamic waves in porous media was derived. These governing equations represent the interrelation between electromagnetics, mechanical energy and fluid flow.
The mechanism for this coupling can be attributed to the electrical double layer created in two-phase (solid and fluid) porous media, in which the phases are considered to be continuously distributed. The electrical double layer refers to the microscopic interface between the grain surface and the fluid electrolyte and consists of two layers, the Stern layer and the diffuse layer. The Stern layer (composed of the inner and outer Helmholtz layers) is a layer of ions adsorbed on to the grain matrix, creating a region of excess charge. To balance this charge, a parallel layer of mobile counter-ions is created in the pore fluid (Lyklema, 1995) (see Figure 1-1). This diffuse layer is free to move, such that a flow of the fluid relative to the fixed solid grains can cause charge separation (Russell et al., 1997).

Electrokinetic phenomena can be separated into EM-to-seismic conversions and seismic-to-

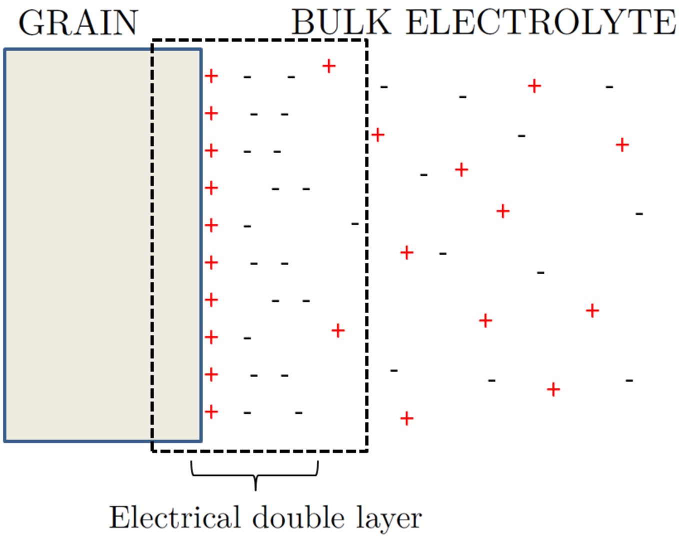

Figure 1-1: Schematic of electrical double layer showing positive ions adsorbed onto grain surface, balanced by negative ions in the diffuse layer of the bulk electrolyte. Figure adapted from Hiemenz and Rajagopalan (1997).

EM conversions; both conversions can be attributed to the nanometer-scale charge separation discussed above (Haines and Pride, 2006). EM-to-seismic conversions have an electromagnetic disturbance as a source function. The disturbance, generally caused by an electrical current source, propagates an EM wave through the subsurface, polarizing the electrical field present at the electrical double layer. This polarization causes relative motion between the fluid electrolyte and the grain matrix and produces pressure gradients, which act as a macroscopic-mechanical pressure disturbance to create an observable coelectric seismic response (Pride, 1994; Hornbostel and Thompson, 2007). This seismic disturbance travels within the confines of the electromagnetic wave. (Note that throughout the thesis we will refer to the behaviour as the electromagnetic field in conductive media as wave propagation; however, the reader should keep in mind that at the frequencies being considered, the waves are highly dispersive and strongly attenuated (Loseth et al., 2006)). At an interface, where there is a discontinuity in either the elastic properties (e.g. porosity), fluid chemistry (e.g. electrolyte concentration) or transport properties (e.g. permeability) (Haartsen and Pride, 1997), the aforementioned pressure gradient will transfer stress to the grain matrix. The time-dependent stress field that is created then, in-turn, generates an independently propagating seismic wave (Thompson and Gist, 1993). Due to the high velocity of the electromagnetic wave, the electromagnetic wave is essentially incident at all points on the interface simultaneously, such that the interface can be considered an exploding reflector. A summation of the infinite point sources creates a plane wave travelling at the seismic wave velocity, as shown in Figure 1-2.

Seismic-to-EM conversions occur for both compressional and shear waves. A seismic perturbation causes movement between the fluid and solid phases; this relative motion of the counter ions of the diffuse layer induces streaming electrical currents. The streaming current sheets produce, albeit small, magnetic fields that induce secondary electrical fields. A further electrical field is created during the propagation of a compressional wave. The peaks and troughs of the P-wave set up regions of excess positive and negative charge in the diffuse layer through the compression and expansion of the electrically charged fluid (Haartsen and Pride, 1997). The electric field produced from this half-wavelength scale charge separation drives a conduction current, which, in homogeneous material, counterbalances the aforementioned streaming current (Pride and Garambois, 2002). Thus, the total current goes to zero and no magnetic field or independent electromagnetic wave is generated. The local electric field that travels within the support of the seismic wave is known as the coseismic field. In the case of an equivolumunal shear wave, no charge separation occurs and the magnetic field is carried within the support of the seismic signal (Pride and Haartsen, 1996; Garambois and Dietrich, 2002). It was found by Garambois and Dietrich (2002) that the coseismic field of the compressional wave is sensitive to the electrical properties of the pore fluid (particularly the electrolyte concentration and the fluid's dielectric permittivity), whereas the shear wave's magnetic field is sensitive to the shear modulus of the framework of grains as well as the viscosity and dielectric permittivity of the pore fluid.

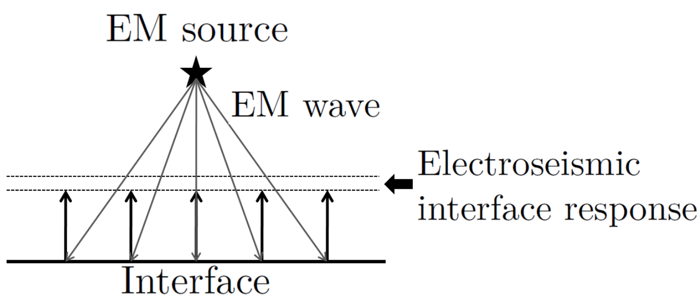

Figure 1-2: Creation of a seismic plane wave at an interface due to an electromagnetic source. The EM wave is incident at all points on the interface simultaneously, each of which acts as a seismic point source. Figure adapted from Shaw (2005).

The second seismoelectric phenomenon occurs at an interface. When the spherical wavefront of a compressional wave traverses an interface, the symmetry of the charge density distribution is broken and a charge separation is created across the interface. In a similar manner, a shear wave that propagates across an interface will create a dynamic current imbalance, thereby forming a charge separation. In both cases, the charge separation acts as an oscillating electric dipole, thereby creating an independently propagating electromagnetic wave that can be recorded almost simultaneously at all receivers, due to the negligible electromagnetic traveltime. This electromagnetic disturbance is called the interface response (Pride and Garambois, 2002; Haines et al., 2007) and is illustrated in Figure 1-3.
In the case of a laterally homogeneous medium, the seismoelectric system can be separated into two independent modes of propagation: SH-TE and P-SV-TM. SH-TE coupling describes the coupling of horizontally polarized shear waves (SH-) and transverse electric polarized electromagnetic waves (TE-). An SH- or TE-wave incident on an interface will generate a total of four wavefields (two reflected and two transmitted). In regards to the P-SV-TM mode, it is known from seismic theory that in horizontally layered media compressional waves (P-) are coupled with vertically polarized shear waves (SV-) and, with the introduction of seismoelectric coupling, these waves are in turn coupled to the transverse magnetic polarized electromagnetic wave (TM-) (Haartsen and Pride, 1997). The fast (dilational wave of the first kind) P-wave is the traditionally recorded compressional motion, travelling through the framework of grains, whereas the slow (dilational wave of the second kind) P-wave travels through the pore fluid as a diffusive pressure wave, thereby propagating slower and attenuating faster (Biot, 1956). In the P-SV-TM system, an incident wavefield will generate up to four reflected and four transmitted wavefields at an interface, for a total of eight wavefields.

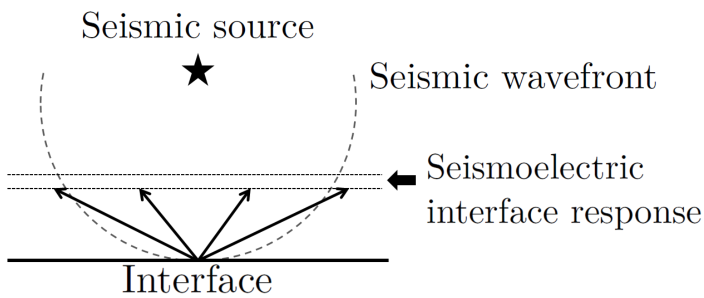

Figure 1-3: Creation of an electromagnetic wave at an interface due to a seismic source. When a seismic wavefront is incident on an interface, a charge separation is created, which acts as a source for an independently propagating EM wave. Figure adapted from Shaw (2005).

1-3 Flux Normalization

The total two-way wavefields that are normally physically registered at receivers can be transformed into a coupled set of oppositely propagating one-way wavefields using so-called one-way wave theory. This theory lends itself well to applications in geophysical surveying for two main

reasons: the vertical direction, depth, can be defined as the "preferred direction of propagation" and the medium variations in the vertical direction are generally more defined, due to stratigraphy, than the variations in the orthogonal directions (i.e. horizontally) (Wapenaar and Grimbergen, 1996). Thus, with one-way wave theory, the total wavefield can be decomposed into its separate upgoing and downgoing consituents, from which one-way wavefield propagators and one-way reflection and transmissions matrices can be derived. A decomposition operator is used to carry out this decomposition and the nature in which the decomposition and composition operators are normalized characterizes the one-way wavefields. An approach for normalizing the reflection and transmission coefficients based on conserving the energy flux across interfaces was introduced for horizontally layered media by Frasier (1970). Under this approach the transmission coefficient at an interface is seen to be independent of the direction of propagation and is equal to $\sqrt{1-R^2}$, where R is the reflection coefficient of the interface. Ursin (1983) applied this flux-normalized decomposition to one-way wavefields in lossless media, stipulating that energy flux in the vertical direction is constant. He pointed out that the inverse of the composition matrix can be determined through the use of a transpose operator, a numerically faster and more stable operator. Wapenaar and Grimbergen (1996) applied flux-normalization to one-way wavefields in the process of deriving reciprocity theorems for one-way wave vectors and they noted that flux-normalization is a prerequisite for using reciprocal one-way propagators. For a more complete explanation of one-way wave theory and flux-normalization, the reader is referred to Ursin (1983); Wapenaar and Berkhout (1989); Wapenaar and Grimbergen (1996).
In this thesis, flux-normalization is applied to the composition and decomposition operators to take advantage of the benefits mentioned above; the inverse of the composition operator can be replaced by the numerically less expensive and more stable transpose operator and since flux-normalized one-way propagators in horizontally layered media obey reciprocity, one-way reciprocity theorems can be applied to the P-SV-TM system.

1-4 Mathematical conventions

1-4-1 Summation convention

In Chapter 2 of this thesis, Einstein's summation convention for repeated indices will be used. Repeated Latin indices (subscripts) indicate a summation from 1 to 3,

$$\frac{\partial v_i}{\partial x_i} \text{ stands for } \sum_{i=1}^{3} \frac{\partial v_i}{\partial x_i}, \tag{1-1}$$

whereas repeated Greek indices indicate a summation from 1 to 2,

$$\frac{\partial v_\alpha}{\partial x_\alpha} \text{ stands for } \sum_{\alpha=1}^{2} \frac{\partial v_\alpha}{\partial x_\alpha}. \tag{1-2}$$

The Levi-Civita symbol, ϵ_{ijk}, is also applied. It takes on the values of -1, 0 or 1 depending on the values of the indices, i.e.

$$\epsilon_{ijk} = \begin{cases} +1 & \text{if } (i,j,k) \text{ is an even permutation of } (1,2,3), \\ -1 & \text{if } (i,j,k) \text{ is an odd permutation of } (1,2,3), \\ 0 & \text{if any index is repeated.} \end{cases} \tag{1-3}$$

For example, the Levi-Civita symbol can be used in combination with Einstein notation to express the curl of the magnetic field vector,

$$\epsilon_{ijk}\frac{\partial H_k}{\partial x_j} = \nabla \times \mathbf{H}. \tag{1-4}$$

1-4-2 Notations

The Cartesian coordinate system is used to uniquely specify positions in space. Throughout the first chapters of this thesis, the three-dimensional coordinates are referred to with the use of subscripts, where x_1, x_2 and x_3 coordinates are used, allowing the concise use of Einstein notation. In Chapters 4 and 5, we no longer make use of index notation and need to refer to a range of different depths levels. For these reasons, we switch the naming convention to refer to the x, y and z axes. In both cases the coordinate system is right-handed, with the x_3 (or z) axis being oriented positive downwards. Consequently, in the context of the one-way wave equation, a $+$ or $-$ superscript denotes a wave travelling in the downward or upward direction, respectively.
Accents are used to specify the domain in which the term is being considered. Terms in the spatial-time domain, (x_i, t), do not have an accent. After transformation to the spatial-frequency domain (x_i, ω) through the use of a temporal Fourier transformation, the terms adopt a hat, $\hat{}$. Finally, a one-dimensional horizontal spatial Fourier transformation will be used to transform the spatial x_1 coordinate to the wavenumber domain. The resulting terms are in the (k_1, x_2, x_3, ω) domain and adopt a tilde, $\tilde{}$.

1-4-3 Fourier Transform

The temporal and spatial Fourier transformations are mathematical functionals that are used to linearly transform terms from one domain to another. Note that although the transformations have a similar form, they differ in the choice of sign of the exponential. The temporal Fourier transformation transforms a time domain function into a frequency domain function according to the following formula:

$$\hat{f}(x_i, \omega) = \int_{-\infty}^{\infty} f(x_i, t)e^{-j\omega t}dt, \tag{1-5}$$

where ω denotes the angular frequency, t is the time, $x_i = (x_1, x_2, x_3)$ represents the spatial coordinates and j is the imaginary unit. To convert a frequency domain function back to a time domain function, an inverse temporal Fourier transformation is performed,

$$f(x_i, t) = \frac{1}{2\pi}\int_{-\infty}^{\infty} \hat{f}(x_i, \omega)e^{j\omega t}d\omega. \tag{1-6}$$

Since the frequency spectrum is complex conjugate symmetric (Hermitian symmetric) around the frequency axis, we can rewrite the inverse temporal Fourier transform as (Bracewell, 1999)

$$f(x_i, t) = \mathrm{Re}\left(\frac{1}{\pi}\int_{0}^{\infty} \hat{f}(x_i, \omega)e^{j\omega t}d\omega\right). \tag{1-7}$$

In carrying out a Fourier transformation one must also take into account the action of the transformation on any operators. After a temporal Fourier expansion, the temporal differential operator, $\frac{\partial}{\partial t}$, is effectively replaced by $j\omega$.
The spatial Fourier transform is used to express a spatial coordinate in terms of its wavenumber and it can be applied to any combination of the spatial coordinates. The one-dimensional spatial Fourier transformation of the x_1 coordinate is given by

$$\tilde{f}(k_1, x_2, x_3, \omega) = \int_{-\infty}^{\infty} \hat{f}(x_i, \omega) e^{jk_1 x_1} dx_1, \tag{1-8}$$

where k_1 is the wavenumber in the x_1 direction. The one-dimensional inverse spatial Fourier transformation is

$$\hat{f}(x_i, \omega) = \frac{1}{2\pi} \int_{-\infty}^{\infty} \tilde{f}(k_1, x_2, x_3, \omega) e^{-jk_1 x_1} dk_1. \tag{1-9}$$

After applying a spatial Fourier transformation, the spatial differential operator, $\frac{\partial}{\partial x_i}$, over which the transform was done is effectively replaced by $-jk_i$, where the subscript i denotes the spatial coordinate of the transform.

1-5 Thesis Outline

This thesis is divided into six chapters. In the first Chapter we have provided a general introduction into the topic. Chapter 2 starts from the macroscopic governing equations of the seismoelectric system, as derived by Pride (1994). These equations are rewritten in the form of the one-way wave equation; in which vertical derivatives of the continuous field vector quantities are expressed in terms of the horizontal variations of the same field vector quantities plus contributions from source terms. We then consider a reduced two-dimensional case and take advantage of symmetry properties of the derived system matrix to decouple the system into its SH-TE and P-SV-TM modes. The P-SV-TM mode is explored in further detail in Chapter 3. The eigenvectors of the P-SV-TM system are introduced and combined into a flux-normalized composition matrix. With the use of the composition matrix and its inverse, the decomposition matrix, we decompose the P-SV-TM mode into its one-way downgoing and upgoing wavefield constituents. Chapter 4 presents the reflection formalism that is used to compute the total upgoing and downgoing wavefields at a receiver location due to an arbitrarily located source. This reflection formalism is applied to the system of Chapter 3 to carry out seismoelectric simulations of the P-SV-TM propagation mode, which are presented in Chapter 5. The final chapter presents conclusions.

Chapter 2

Seismoelectric equations

In this chapter Pride's macroscoping governing equations are introduced and expressed in the form of the two-way wave equation, in which the field vector of the two-way wave equation contains the field quantities that are continuous across interfaces. We simplify the system by considering horizontally layered homogeneous media, for which the system decouples into two independent modes of propagation: SH-TE and P-SV-TM. Chapter 3 continues on with the P-SV-TM mode of the two-dimensional seismoelectric system.

2-1 Governing equations

The complete set of macroscopic governing equations of the coupled electromagnetic elastodynamic system in an arbitrary inhomogeneous porous medium were derived by Pride (1994) through the use of volume averaging techniques. His electrokinetic formulation has been extensively modelled (e.g. Haartsen and Pride (1997); Garambois and Dietrich (2002); Haines and Pride (2006), among others) and experimentally validated (Schoemaker et al., 2011). The governing equations can be grouped into pairs of transport equations, stress-strain relations and electromagnetic constitutive laws, all interrelated through a coupling coefficient. The coupling is a consequence of two postulates: first, that an electrical double layer is present, and secondly, that at initial conditions there is no net charge in a volume of the porous material. The term "macroscopic" refers to the assumption that the wavelengths of the applied disturbances are significantly greater than the grain dimension, such that there is no scattering from individual grains. This restricts the maximum frequency to the order of 10^6 Hz. Further assumptions of the derived theory are the following: only linear disturbances are considered, the fluid is assumed to be an ideal electrolyte, and wave-induced diffusion effects, the Lorentz force and piezoelectric effects are neglected. A further discussion on these assumptions can be found in Pride (1994) and Pride and Haartsen (1996).

2-1-1 Coupling coefficient

The electrokinetic coupling coefficient, $\hat{\mathcal{L}}$, accounts for the coupling between the elastodynamic and electromagnetic wavefields and is described by,

$$\hat{\mathcal{L}} = \mathcal{L}_0 \left[1 + j\frac{\omega}{\omega_c}\frac{m}{4}\left(1 - 2\frac{d^l}{\Lambda}\right)^2 \left(1 + d^l\sqrt{\frac{j\omega\rho^f}{\eta}}\right)^2\right]^{-\frac{1}{2}}, \tag{2-1}$$

where $\mathcal{L}_0$ represents the static coupling coefficient,

$$\mathcal{L}_0 = -\frac{\phi}{\alpha_\infty}\frac{\epsilon_0\epsilon_r^f\zeta}{\eta}\left(1 - 2\frac{d^l}{\Lambda}\right); \tag{2-2}$$

ω_c, the critical frequency; m, the similarity parameter; d^l, the Debye screening length; Λ, the volume-to-surface ratio of the porous material; ρ^f, the density of the fluid phase; η, the viscosity of the pore fluid; ϕ, the porosity as a volume fraction; ϵ_0, the permittivity of free space; ϵ_r^f, the fluid's relative dielectric permittivity; ζ, the zeta potential of the double layer; and α_∞, the tortuosity. The frequency dependency of the coupling coefficient relates to relaxation associated with the development of viscous boundary layers in the pores (Pride, 1994). The amplitude and frequency behaviour of the coupling coefficient has been validated by recent laboratory measurements (Schoemaker, 2011).
The critical frequency is a transition frequency separating low-frequency viscous flow from high-frequency inertial flow and is defined as

$$\omega_c = \frac{\phi\eta}{\alpha_\infty k_0\rho^f}. \tag{2-3}$$

For realistic rock and fluid parameters, the transition frequency lies above the frequency band of interest, where we consider the bandwidth of interest to lie between 10^1 and 10^3 Hz. Thus although $\hat{\mathcal{L}}$ is complex and frequency-dependent, viscous boundary layers do not develop when $\omega \ll \omega_c$, hence we can assume that $\hat{\mathcal{L}} = \mathcal{L}_0$. Considering the small $\frac{d^l}{\Lambda}$ limit, the static coupling coefficient reduces to (Garambois and Dietrich, 2001; Pride and Garambois, 2005),

$$\mathcal{L}_0 = -\frac{\phi}{\alpha_\infty}\frac{\epsilon_0\epsilon_r^f\zeta}{\eta}. \tag{2-4}$$

The Debye screening length is a characteristic thickness of the electrical double layer, typically on the order of nanometres. It is essentially the distance over which mobile charge carriers in the electrolyte screen out the surface charge present on the grains of the saturated porous medium,

$$d^l = \sum_{l=1}^{L}\sqrt{\frac{\epsilon_0\epsilon_r^f k_B T}{e^2 z_l^2 N_l}}, \tag{2-5}$$

where $k_B T$ is the thermal energy of the system, e is the elementary charge, z_l is the valence of the lth ion, N_l is the bulk-ionic concentration of species l out of a total L species in the system. N_l is calculated from

$$N_l = 10^3 C N_A \left|z_l'\right| \tag{2-6}$$

where C is the electrolyte concentration of the pore fluid in moles per litre, N_A is Avogadro's constant, with a value of 6.022×10^{23} mol^{-1}, and z_l' is the valency of the conjugate ion. The zeta potential is also known as the electrokinetic potential and defines the electrical potential at the electrical double layer's slipping plane, a plane within the diffuse layer that separates the surface-bound ions from the mobile ions. A literature review by Pride and Morgan (1991) on experimental studies of the zeta potential of quartz found

$$\zeta = 8 + 26\log_{10} C \tag{2-7}$$

to be a reasonable approximation, with ζ in millivolts.
The similarity parameter is a dimensionless number that consists only of terms that characterize the pore geometry. It is mathematically expressed as

$$m = \frac{\phi \Lambda^2}{\alpha_\infty k_0}, \tag{2-8}$$

and will be fixed to a value of 8 (Johnson, 1989) throughout our modelling.

2-1-2 Mechanical equations

Pride's transport equations are derived from the principle of conservation of linear momentum and are expressed for an arbitrary inhomogeneous anisotropic medium by

$$j\omega \hat{\rho}^b \hat{v}_i^s + j\omega \hat{\rho}^f \hat{w}_i - \frac{\partial \hat{\tau}_{ij}^b}{\partial x_j} = \hat{f}_i^b, \tag{2-9}$$

$$j\omega \hat{\rho}^f \hat{v}_i^s + \frac{\eta}{\hat{k}}(\hat{w}_i - \hat{\mathcal{L}} \hat{E}_i) + \frac{\partial \hat{p}}{\partial x_i} = \hat{f}_i^f, \tag{2-10}$$

with

$$\hat{w}_i = \phi(\hat{v}_i^f - \hat{v}_i^s), \tag{2-11}$$

$$\hat{\rho}^b = (1-\phi)\hat{\rho}^s + \phi \hat{\rho}^f, \tag{2-12}$$

where $\hat{\rho}^b$, $\hat{\rho}^s$ and $\hat{\rho}^f$ are the anisotropic frequency-dependent density functions for the bulk, solid and fluid, respectively, $\hat{v}_i^s$ and $\hat{v}_i^f$ are the averaged solid and fluid particle velocities, $\hat{w}_i$ is the Darcy filtration velocity, $\hat{\tau}_{ij}^b$ is the averaged bulk stress, $\hat{f}_i^b$ and $\hat{f}_i^f$ are the volume densities of the external (source) force applied to the bulk and fluid phases, respectively, and $\hat{p}$ is the averaged fluid pressure. The normal components of the bulk stress tensor, corresponding to $i = j$, can be considered to be tensile stresses, while the tangential components, corresponding to $i \neq j$, are the shear stresses. In an ideal fluid, where shearing stresses are not sustained, the pressure is given by the negative tensile stress (Wapenaar and Berkhout, 1989). Note that setting the coupling coefficient to zero reduces Equations (2-9) and (2-10) to Biot's equations of motion (Biot, 1956) and decouples the elastodynamic and electromagnetic waves.
The second set of mechanical equations, the stress-strain relations, are given by

$$-j\omega \hat{\tau}_{ij}^b + \hat{d}_{ijkl} \frac{\partial \hat{v}_k^s}{\partial x_l} + \hat{C}_{ij} \frac{\partial \hat{w}_k}{\partial x_k} = \hat{d}_{ijkl} \hat{h}_{kl}^b + \hat{C}_{ij} \hat{q}^i, \tag{2-13}$$

$$j\omega \hat{p} + \hat{C}_{kl} \frac{\partial \hat{v}_k^s}{\partial x_k} + \hat{M} \frac{\partial \hat{w}_k}{\partial x_k} = \hat{C}_{kl} \hat{h}_{kl}^b + \hat{M} \hat{q}^i \tag{2-14}$$

where $\hat{d}_{ijkl}$, $\hat{C}$ and $\hat{M}$ are stiffness parameters of the porous solid, $\hat{h}^b_{kl}$ is the bulk external deformation rate density and $\hat{q}^i$ is the fluid phase volume injection rate density. Note that $\hat{\tau}^b_{ij} = \hat{\tau}^b_{ji}$, $\hat{h}^b_{ij} = \hat{h}^b_{ji}$, $\hat{C}_{ij} = \hat{C}_{ji}$ and $d_{ijkl} = d_{jikl} = d_{ijlk} = d_{klij}$.

Throughout the rest of this thesis, we consider all elastic media parameters to be isotropic and specified media parameters to be frequency-independent. The frequency-independent stiffness tensor for isotropic media is

$$d_{ijkl} = (\mathrm{K}_G - \frac{2}{3}G^{\mathrm{fr}})\delta_{ij}\delta_{kl} + G^{\mathrm{fr}}(\delta_{ik}\delta_{jl} + \delta_{il}\delta_{jk}), \tag{2-15}$$

where G^{fr} is the frequency-indepedent shear modulus of the solid framework and K_G is Gassmann's bulk modulus,

$$\mathrm{K}_G = \frac{\mathrm{K}^{\mathrm{fr}} + \phi\mathrm{K}^f + (1+\phi)\mathrm{K}^s\Delta}{1+\Delta}, \tag{2-16}$$

where K^{fr}, K^f and K^s are the frequency-independent compression moduli of the grain framework, the fluid phase and the solid phase, respectively. Δ is defined as

$$\Delta = \frac{\mathrm{K}^f}{\phi(\mathrm{K}^s)^2}[(1-\phi)\mathrm{K}^s - \mathrm{K}^{\mathrm{fr}}]. \tag{2-17}$$

The elastic parameters C and M can be defined in terms of the fluid and solid moduli,

$$C = \frac{\mathrm{K}^f + \mathrm{K}^s\Delta}{1+\Delta}, \tag{2-18}$$

$$M = \frac{\mathrm{K}^f}{\phi(1+\Delta)}. \tag{2-19}$$

The dynamic permeability is taken to be frequency-dependent with $\hat{k}_{ij} = \delta_{ij}\hat{k}$ and $\hat{k}$ defined by,

$$\hat{k} = k_0 \left[(1 + j\tfrac{\omega}{\omega_c}\tfrac{4}{m})^{\frac{1}{2}} + j\tfrac{\omega}{\omega_c}\right]^{-1}. \tag{2-20}$$

If we again consider frequencies significantly below the transition frequency, the frequency-dependent dynamic permeability reduces to the value of the static permeability, $\hat{k} = k_0$.

2-1-3 Electromagnetic equations

The Maxwell-Faraday equation and Ampere's circuital law are given in the frequency domain by (Griffiths, 1999)

$$\epsilon_{ijk}\frac{\partial \hat{E}_k}{\partial x_j} = -j\omega\hat{B}_i, \tag{2-21}$$

$$\epsilon_{ijk}\frac{\partial \hat{H}_k}{\partial x_j} = j\omega\hat{D}_i + \hat{J}^f_i, \tag{2-22}$$

where $\hat{D}_i$ and $\hat{B}_i$ are the averaged electric and magnetic flux densities, $\hat{H}_i$ and $\hat{E}_i$ are the averaged electric and magnetic fields and $\hat{J}^f_i$ is the ionic-current density. With the inclusion of electric and magnetic current densities, they lead to the following equations (Pride, 1994; De Ridder, 2007)

$$j\omega \hat{D}_i + \hat{J}_i^{\mathbf{i},e} - \epsilon_{ijk}\frac{\partial \hat{H}_k}{\partial x_j} = -\hat{J}_i^{\mathbf{s},e}, \tag{2-23}$$

$$j\omega \hat{B}_i + \hat{J}_i^{\mathbf{i},m} + \epsilon_{ijk}\frac{\partial \hat{E}_k}{\partial x_j} = -\hat{J}_i^{\mathbf{s},m}, \tag{2-24}$$

where $\hat{J}_i^{\mathbf{i},e}$ and $\hat{J}_i^{\mathbf{i},m}$ are the induced electric and magnetic current densities and $\hat{J}_i^{\mathbf{s},e}$ and $\hat{J}_i^{\mathbf{s},m}$ are the external electric and magnetic current source densities. The above equations are closed by

$$\hat{J}_i^{\mathbf{i},e} = (\hat{\sigma}^e - \frac{\eta}{\hat{k}}\hat{\mathcal{L}}^2)\hat{E}_i + \frac{\eta}{\hat{k}}\hat{\mathcal{L}}\hat{w}_i, \tag{2-25}$$

$$\hat{J}_i^{\mathbf{i},m} = \hat{\sigma}^m \hat{H}_i, \tag{2-26}$$

and the constitutive relations

$$\hat{D}_i = \epsilon_0\epsilon_r\hat{E}_i = \epsilon\hat{E}_i, \tag{2-27}$$

$$\hat{B}_i = \mu_0\mu_r\hat{H}_i = \mu\hat{H}_i, \tag{2-28}$$

where $\hat{\sigma}^e$ and $\hat{\sigma}^m$ are the frequency-dependent electric and magnetic conductivities, while ϵ and μ are the frequency-independent dielectric permittivity and magnetic permeability, respectively. With the substitution of Equations (2-25), (2-26), (2-27) and (2-28) into Maxwell's equations (2-23) and (2-24), the coupled electromagnetic field equations are obtained

$$j\omega\epsilon\hat{E}_i + (\hat{\sigma}^e - \frac{\eta}{\hat{k}}\hat{\mathcal{L}}^2)\hat{E}_i + \frac{\eta}{\hat{k}}\hat{\mathcal{L}}\hat{w}_i - \epsilon_{ijk}\frac{\partial \hat{H}_k}{\partial x_j} = -\hat{J}_i^{\mathbf{s},e}, \tag{2-29}$$

$$j\omega\mu\hat{H}_i + \hat{\sigma}^m\hat{H}_i + \epsilon_{ijk}\frac{\partial \hat{E}_k}{\partial x_j} = -\hat{J}_i^{\mathbf{s},m}. \tag{2-30}$$

For notational clarity, $\hat{J}_i^{\mathbf{s},e}$ and $\hat{J}_i^{\mathbf{s},m}$ will be replaced by $\hat{J}_i^e$ and $\hat{J}_i^m$, where $\hat{J}_i^e$ and $\hat{J}_i^m$ now take on the definitions of external electric and magnetic current source densities. All relaxation mechanisms are captured within the electric and magnetic conductivity functions.
The electrical conductivity is a function of the frequency-independent bulk-fluid conductivity, σ^f, the frequency-independent double layer ion electromigration conductance, C_{em}, and the frequency-dependent conductance due to electrically induced streaming of the excess double layer, $\hat{C}_{os}$. It is defined as (Pride, 1994)

$$\hat{\sigma}^e = \frac{\phi\sigma^f}{\alpha_\infty}\left(1 + \frac{2(C_{em} + \hat{C}_{os})}{\sigma^f\Lambda}\right), \tag{2-31}$$

with

$$\sigma^f = \sum_{l=1}^{L} (ez_l)^2 b_l N_l, \tag{2-32}$$

$$C_{em} \simeq 2 - D^l \sum_{l=1}^{L} (ez_l)^2 b_l N_l \left[\exp\left(-\frac{ez_l \zeta}{2k_B T} \right) - 1 \right], \tag{2-33}$$

$$\hat{C}_{os} = \frac{(\epsilon_0 \epsilon_r^f)^2 \zeta^2}{2d^l \eta} P \left(1 - \frac{2d^l \exp[\frac{j\pi}{4}]}{P\delta} \right)^{-1} (1), \tag{2-34}$$

$$\tag{2-35}$$

where b_l represents the ion-mobilities, δ the viscous skin depth,

$$\delta = \sqrt{\frac{\eta}{\rho^f \omega}}, \tag{2-36}$$

and P is a dimensionless parameter. P is always greater than one and is defined as

$$P = \frac{8k_B T (d^l)^2}{\epsilon_0 \epsilon_r^f \zeta^2} \sum_{l=1}^{L} N_l \left[\exp\left(-\frac{ez_l \zeta}{2k_B T} \right) - 1 \right]. \tag{2-37}$$

The weak dependency on frequency within the electro-osmotic conductance term does not cause relaxation in the electrical conductivity in the frequency band of interest, thus the frequency-dependent electrical conductivity reduces to

$$\hat{\sigma}^e = \frac{\phi \sigma^f}{\alpha_\infty}, \tag{2-38}$$

to leading order in $\frac{d}{\Lambda}$ (Pride and Garambois, 2005). We simplify the conductivity of the pure electrolyte to

$$\sigma^f = (ez)^2 N (b_+ + b_-), \tag{2-39}$$

where b_+ and b_- are the ionic mobilities of the cations and anions, respectively, with typical values of approximately 3.0×10^{11} m s^{-1} N^{-1} for inorganic ions (Haartsen and Pride, 1997). In this thesis magnetic relaxation losses will be neglected, i.e. $\hat{\sigma}^m = 0$. The relative magnetic permeability will be set to one, such that $\mu = \mu_0 \mu_r = \mu_0$, while the relative dielectric permittivity will be calculated using (Pride, 1994)

$$\epsilon_r = \frac{\phi}{\alpha_\infty} (\epsilon_r^f - \epsilon_r^s) + \epsilon_r^s, \tag{2-40}$$

where ϵ_r^f and ϵ_r^s are the relative dielectric constants of the fluid and solid, respectively.

2-2 Boundary Conditions

The wavefields on either side of an interface between two dissimilar materials must satisfy specific continuity requirements. At a lossless open-pore interface (i.e. where the pores of the two media are completely connected), Deresiewicz and Skalak (1963) found that the only

permissible set of boundary conditions requires the continuity of the following quantities: the normal and tangential components of the bulk stress, $\boldsymbol{\tau}^b_n$; the normal and tangential components of the skeletal velocity, $\mathbf{v}^s$; the pore pressure, p; and the normal component of the Darcy filtration velocity, $\mathbf{w}_n$. The interface conditions governing the electric and magnetic fields can be derived from the integral form of Maxwell's equations. It is found that the tangential components of these fields are continuous.
Based on the normal being oriented in the x_3 direction, the above quantities can all be combined into a wave vector $\mathbf{q}$:

$$\mathbf{q} = \left(-\boldsymbol{\tau}^b_3, p, \mathbf{v}^s, w_3, \mathbf{E}_0, \mathbf{H}_0\right)^t, \tag{2-41}$$

where

$$\boldsymbol{\tau}^b_3 = \begin{pmatrix} \tau^b_{13} \\ \tau^b_{23} \\ \tau^b_{33} \end{pmatrix}, \mathbf{v}^s = \begin{pmatrix} v^s_1 \\ v^s_2 \\ v^s_3 \end{pmatrix}, \mathbf{E}_0 = \begin{pmatrix} E_1 \\ E_2 \end{pmatrix}, \mathbf{H}_0 = \begin{pmatrix} H_2 \\ -H_1 \end{pmatrix}. \tag{2-42}$$

The continuity of this wave vector at a source-free interface can be explicitly written as

$$\lim_{x_3 \downarrow x_{3,n}} \mathbf{q}_{n+1}(x_3) - \lim_{x_3 \uparrow x_{3,n}} \mathbf{q}_n(x_3) = \mathbf{0}, \tag{2-43}$$

where x_3 is positive downwards, and layers n and $n+1$ are the upper and lower mediums, respectively, as depicted in Figure 2-1.
If there is a source located inside a homogeneous medium, the wave vectors on either side

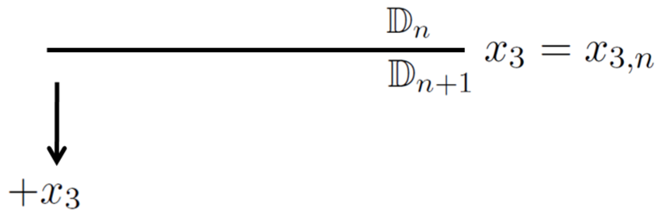

Figure 2-1: Interface between two media with different medium parameters.

of the source level will not be continuous: they will be subject to a jump discontinuity due to the source injection. The jump is represented by the source vector, $\mathbf{d}$, which has the same number of components as the wave vector and is specified at the source level, $x_{3,s}$,

$$\lim_{x_3 \downarrow x_{3,s}} \mathbf{q}^b(x_3) - \lim_{x_3 \uparrow x_{3,s}} \mathbf{q}^a(x_3) = \mathbf{d}(x_{3,s}), \tag{2-44}$$

where $\mathbf{q}^b$ is evaluated immediately below the source level and $\mathbf{q}^a$ immediately above.

2-3 Rewriting governing equations

In explorational geophysics one can define the vertical axis as a "preferred direction of propagation". The wavefields in the preferred direction of propagation, in this case depth, can

be split into oppositely propagating waves. To take this preferential direction into account and assuming that the medium is laterally homogeneous, the wavefield quantities that are not differentiable with depth are eliminated from the system. The wavefield quantities that are differentiable with depth are subject to boundary conditions at interfaces in the laterally homogeneous medium. These remaining wavefield quantities can be expressed in terms of their horizontal derivatives (Wapenaar, 1996).
In this section the governing equations will be organized into a form that can be compactly expressed through a matrix-vector representation of the two-way wave equation,

$$\frac{\partial \hat{\mathbf{q}}}{\partial x_3} = \hat{\mathbf{A}}\hat{\mathbf{q}} + \hat{\mathbf{d}}, \tag{2-45}$$

where $\hat{\mathbf{q}}$ contains the chosen field quantities, $\hat{\mathbf{A}}$ contains the medium parameters of the system and the horizontal derivatives of the field quantities and $\hat{\mathbf{d}}$ represents the source vector. It is thus necessary to reorganize the governing equations such that the vertical derivatives of the continuous wavefields are expressed as a function of the horizontal derivatives, plus a source term, as previously performed by Shaw (2005) and De Ridder (2007).
First we rewrite the transport equations (Equations (2-9) and (2-10)) as

$$j\omega\rho^b \hat{v}_i^s + j\omega\rho^f \delta_{ij}\hat{w}_j - \frac{\partial \hat{\tau}_{ij}^b}{\partial x_j} = \hat{f}_i^b, \tag{2-46}$$

$$j\omega\rho^f \delta_{ij}^t \hat{v}_i^s + \frac{\eta}{\hat{k}}\left[\hat{w}_i - \hat{\mathcal{L}}(\gamma_{i\alpha}^t \hat{E}_\alpha + \delta_{i3}\hat{E}_3)\right] + \frac{\partial \hat{p}}{\partial x_i} = \hat{f}_i^f, \tag{2-47}$$

where the subscript α denotes the horizontal components. To express the stress-strain relations in a similar form, the $\partial_k \hat{w}_k$ term is eliminated from Eq. (2-13) by isolating it from Eq. (2-14),

$$\frac{\partial \hat{w}_k}{\partial x_k} = \frac{1}{M}\left(C\hat{h}_{kl}^b + M\hat{q}^i - j\omega\hat{p} - C\frac{\partial \hat{v}_k^s}{\partial x_k}\right). \tag{2-48}$$

This is substituted into Eq. (2-13) to yield

$$-j\omega\hat{\tau}_{ij}^b + e_{ijkl}\frac{\partial \hat{v}_k^s}{\partial x_l} - j\omega\frac{C}{M}\delta_{ij}\hat{p} = e_{ijkl}\hat{h}_{kl}^b, \tag{2-49}$$

where

$$e_{ijkl} = d_{ijkl} - \frac{C^2}{M}\delta_{ij}\delta_{kl}. \tag{2-50}$$

The stress-strain relations can now be reformulated as

$$-j\omega\hat{\tau}_{ij}^b + \mathrm{e}_{ijkl}\frac{\partial \hat{v}_i^s}{\partial x_l} - j\omega\frac{C}{M}\delta_{ij}\hat{p} = \mathrm{e}_{ijkl}\hat{h}_{kl}^b, \tag{2-51}$$

$$j\omega\hat{p} + C\delta_{kl}^t\frac{\partial \hat{v}_k^s}{\partial x_k} + M\frac{\partial \hat{w}_k}{\partial x_k} = \hat{C}_{kl}^t\hat{h}_{kl}^b + \hat{M}\hat{q}^i, \tag{2-52}$$

where e_{ijkl} is a symmetric matrix that is defined as

$$\mathrm{e}_{ijkl} = \mathbf{e}_{jl} = \begin{pmatrix} \mathrm{e}_{1j1l} & \mathrm{e}_{1j2l} & \mathrm{e}_{1j3l} \\ \mathrm{e}_{2j1l} & \mathrm{e}_{2j2l} & \mathrm{e}_{2j3l} \\ \mathrm{e}_{3j1l} & \mathrm{e}_{3j2l} & \mathrm{e}_{3j3l} \end{pmatrix}, \tag{2-53}$$

and can also be expressed through

$$(\mathbf{e}_{jl})_{ik} = e_{ijkl} = S\delta_{ij}\delta_{kl} + G^{\mathrm{fr}}(\delta_{ik}\delta_{jl} + \delta_{il}\delta_{jk}). \tag{2-54}$$

The elastic media parameter S is defined as

$$S = \mathrm{K}_G - \frac{2}{3}\mathrm{G}_{\mathrm{fr}} - \frac{C^2}{M}. \tag{2-55}$$

The electromagnetic field equations are similarily written in a manner that facilitates separation of the vertical and horizontal derivatives. Rewriting Equation (2-29) leads to the following three equations:

$$j\omega\hat{\varepsilon}_{\mathcal{L}}\hat{E}_1 + \frac{\eta}{\hat{k}}\hat{\mathcal{L}}\hat{w}_1 + \frac{\partial \hat{H}_2}{\partial x_3} - \frac{\partial \hat{H}_3}{\partial x_2} = -\hat{J}^e_1, \tag{2-56}$$

$$j\omega\hat{\varepsilon}_{\mathcal{L}}\hat{E}_2 + \frac{\eta}{\hat{k}}\hat{\mathcal{L}}\hat{w}_2 - \frac{\partial \hat{H}_1}{\partial x_3} + \frac{\partial \hat{H}_3}{\partial x_1} = -\hat{J}^e_2, \tag{2-57}$$

$$j\omega\hat{\varepsilon}_{\mathcal{L}}\hat{E}_3 + \frac{\eta}{\hat{k}}\hat{\mathcal{L}}\hat{w}_3 - \frac{\partial \hat{H}_2}{\partial x_1} + \frac{\partial \hat{H}_1}{\partial x_2} = -\hat{J}^e_3. \tag{2-58}$$

with the definitions

$$\hat{\rho}^E = \frac{\eta}{j\omega\hat{k}},\ \hat{\varepsilon} = \epsilon_0\epsilon_r + \frac{\hat{\sigma}^e}{j\omega}, \hat{\varepsilon}_{\mathcal{L}} = \hat{\varepsilon} - \hat{\rho}^E\hat{\mathcal{L}}^2. \tag{2-59}$$

The term $\hat{\rho}^E$ denotes the effective density of the fluid in relative motion; $\hat{\varepsilon}$, the effective dielectric permittivity of the porous medium; and $\hat{\varepsilon}_{\mathcal{L}}$, a modified effective dielectric permittivity that includes the coupling coefficient. Equation (2-30) can be analogously rewritten to yield

$$j\omega\mu_0\hat{H}_2 + \frac{\partial \hat{E}_1}{\partial x_3} - \frac{\partial \hat{E}_3}{\partial x_1} = -\hat{J}^m_2, \tag{2-60}$$

$$j\omega\mu_0\hat{H}_1 - \frac{\partial \hat{E}_2}{\partial x_3} + \frac{\partial \hat{E}_3}{\partial x_2} = -\hat{J}^m_1, \tag{2-61}$$

$$j\omega\mu_0\hat{H}_3 - \left(\tfrac{\partial}{\partial x_2} \quad -\tfrac{\partial}{\partial x_1}\right)\hat{E}_\alpha = -\hat{J}^m_3. \tag{2-62}$$

Now the vertical derivatives can be compiled from the rewritten governing equations,

$$-\frac{\partial \hat{\tau}^b_{i3}}{\partial x_3} = -j\omega\rho^b \hat{v}^s_i - j\omega\rho^f(\delta_{i\alpha}\hat{w}_\alpha + \delta_{i3}\hat{w}_3) + \frac{\partial \hat{\tau}^b_{i\alpha}}{\partial x_\alpha} + \hat{f}^b_i, \tag{2-63}$$

$$\frac{\partial \hat{p}}{\partial x_3} = -j\omega\rho^f \delta^t_{i3}\hat{v}^s_i - \frac{\eta}{\hat{k}}\left(\hat{w}_3 - \hat{\mathcal{L}}\hat{E}_3\right) + \hat{f}^f_3, \tag{2-64}$$

$$\frac{\partial \hat{v}^s_i}{\partial x_3} = \mathrm{e}^{-1}_{i3k3}\left(j\omega\hat{\tau}^b_{i3} + j\omega\frac{C}{M}\delta_{i3}\hat{p} - \mathrm{e}_{i3k\beta}\frac{\partial \hat{v}^s_i}{\partial x_\beta}\right) + \mathrm{e}^{-1}_{i3k3}\mathrm{e}_{i3kl}\hat{h}^b_{kl}, \tag{2-65}$$

$$\frac{\partial \hat{w}_3}{\partial x_3} = -\frac{j\omega}{M}\hat{p} - \frac{C}{M}\left(\delta^t_{i\beta}\frac{\partial \hat{v}^s_i}{\partial x_\beta} + \delta^t_{i3}\frac{\partial \hat{v}^s_i}{\partial x_3}\right) - \frac{\partial \hat{w}_\beta}{\partial x_\beta} + \frac{\hat{C}^t_{kl}\hat{h}^b_{kl}}{M} + \hat{q}_i, \tag{2-66}$$

$$\frac{\partial \hat{E}_1}{\partial x_3} = -j\omega\mu_0\hat{H}_2 + \frac{\partial \hat{E}_3}{\partial x_1} - \hat{J}^m_2, \tag{2-67}$$

$$\frac{\partial \hat{E}_2}{\partial x_3} = j\omega\mu_0\hat{H}_1 + \frac{\partial \hat{E}_3}{\partial x_2} + \hat{J}^m_1, \tag{2-68}$$

$$\frac{\partial \hat{H}_2}{\partial x_3} = -j\omega\hat{\varepsilon}_{\mathcal{L}} - \frac{\eta}{\hat{k}}\hat{\mathcal{L}}\hat{w}_1 + \frac{\partial \hat{H}_3}{\partial x_2} - \hat{J}^e_1, \tag{2-69}$$

$$\frac{\partial \hat{H}_1}{\partial x_3} = j\omega\hat{\varepsilon}_{\mathcal{L}} + \frac{\eta}{\hat{k}}\hat{\mathcal{L}}\hat{w}_2 + \frac{\partial \hat{H}_3}{\partial x_1} + \hat{J}^e_2. \tag{2-70}$$

(2-71)

The next step is to express these vertical derivatives as functions of the elements of the wave vector and the horizontal derivatives of that vector. Starting with the equation for the vertical derivative of the bulk-averaged stress tensor, Equation (2-63), the $\hat{w}_\alpha$ and $\hat{\tau}^b_{i\alpha}$ terms are eliminated, after being isolated from Equations (2-47) and (2-51),

$$\begin{aligned}-\frac{\partial \hat{\tau}^b_{i3}}{\partial x_3} = &-j\omega\rho^b\hat{v}^s_i - j\omega\rho^f\delta_{i3}\hat{w}_3 - j\omega\rho^f\delta_{i\alpha}\left[\frac{\hat{k}}{\eta}\left(\hat{f}^f_\alpha - j\omega\rho^f\delta^t_{i\alpha}\hat{v}^s_i - \frac{\partial \hat{p}}{\partial x_\alpha}\right) + \hat{\mathcal{L}}\gamma^t_{i\alpha}\hat{E}_\alpha\right]\\ &+ \frac{1}{j\omega}\frac{\partial}{\partial x_\alpha}\left(\mathrm{e}_{i\alpha k\beta}\frac{\partial \hat{v}^s_i}{\partial x_\beta} + \mathrm{e}_{i\alpha k3}\frac{\partial \hat{v}^s_i}{\partial x_3} - j\omega\frac{C}{M}\delta_{i\alpha}\hat{p} - \mathrm{e}_{i\alpha kl}\hat{h}^b_{kl}\right) + \hat{f}^b_i.\end{aligned} \tag{2-72}$$

We then eliminate the $\partial_3\hat{v}^s_i$ term through substitution of Equation (2-65),

$$\begin{aligned}-\frac{\partial \hat{\tau}^b_{i3}}{\partial x_3} = &\frac{\partial}{\partial x_\alpha}(\mathrm{e}_{i\alpha k3}\mathrm{e}^{-1}_{i3k3}\hat{\tau}^b_{i3}) + j\omega\rho^f\frac{\hat{k}}{\eta}\delta_{i\alpha}\frac{\partial \hat{p}}{\partial x_\alpha} - \frac{1}{j\omega}\frac{\partial}{\partial x_\alpha}\left(j\omega\frac{C}{M}\mathrm{u}_{i\alpha}\hat{p} - \mathrm{U}_{i\alpha k\beta}\frac{\partial \hat{v}^s_i}{\partial x_\beta}\right)\\ &- j\omega\left(\rho_b\delta_{ij} - j\omega(\rho^f)^2\frac{\hat{k}}{\eta}\delta_{i\alpha}\delta^t_{i\alpha}\right)\hat{v}^s_i - j\omega\rho^f\delta_{i3}\hat{w}_3 - j\omega\rho^f\hat{\mathcal{L}}\gamma^t_{i\alpha}\delta_{i\alpha}\hat{E}_\alpha\\ &- j\omega\rho^f\frac{\hat{k}}{\eta}\delta_{i\alpha}\hat{f}^f_\alpha + \hat{f}^b_i - \frac{1}{j\omega}\frac{\partial}{\partial x_\alpha}\mathrm{U}_{i\alpha k\beta}h^b_{k\beta},\end{aligned} \tag{2-73}$$

where

$$\mathrm{U}_{i\alpha k\beta} = \mathrm{e}_{i\alpha k\beta} - \mathrm{e}_{i\alpha k3}\mathrm{e}^{-1}_{i3k3}\mathrm{e}_{i3k\beta}, \tag{2-74}$$

$$\mathrm{u}_{i\alpha} = \delta_{i\alpha} - \mathrm{e}_{i\alpha k3}\mathrm{e}^{-1}_{i3k3}\delta_{i3}. \tag{2-75}$$

The vertical derivative of $\hat{p}$ can be expressed by isolating $\hat{E}_3$ from Equation (2-58) and substituting it into Equation (2-64),

$$\begin{aligned}\frac{\partial \hat{p}}{\partial x_3} &= -j\omega\rho^f \delta^t_{i3}\hat{v}^s_i - \frac{\eta}{\hat{k}}\left(1+\frac{\hat{\rho}^E\hat{\mathcal{L}}^2}{\hat{\varepsilon}_{\mathcal{L}}}\right)\hat{w}_3 + \frac{\hat{\rho}^E\hat{\mathcal{L}}}{\hat{\varepsilon}_{\mathcal{L}}}\left(\frac{\partial \hat{H}_2}{\partial x_1} - \frac{\partial \hat{H}_1}{\partial x_2}\right) \\ &\quad - \frac{\hat{\rho}^E\hat{\mathcal{L}}}{\hat{\varepsilon}_{\mathcal{L}}}\hat{J}^e_3 + \hat{f}^f_3 .\end{aligned} \tag{2-76}$$

To rewrite $\partial_3\hat{w}_3$ we eliminate the $\partial_3\hat{v}^s_i$ and $\partial_\beta\hat{w}_\beta$ terms from Equation (2-66) using Equations (2-65) and (2-47),

$$\begin{aligned}\frac{\partial \hat{w}_3}{\partial x_3} &= -\frac{C}{M}\delta^t_{i3}e^{-1}_{i3k3}\left(j\omega\hat{\tau}^b_{i3} + j\omega\frac{C}{M}\delta_{i3}\hat{p}\right) - \frac{j\omega}{M}\hat{p} + \frac{\partial}{\partial x_\beta}\left(\frac{\hat{k}}{\eta}\frac{\partial \hat{p}}{\partial x_\beta} + j\omega\rho^f\frac{\hat{k}}{\eta}\delta^t_{i\beta}\hat{v}^s_i - \hat{\mathcal{L}}\gamma^t_{i\beta}\hat{E}_\beta\right) \\ &\quad - \frac{C}{M}\mathrm{u}^t_{i\beta}\frac{\partial \hat{v}^s_i}{\partial x_\beta} + \frac{C}{M}\mathrm{u}^t_{i\beta}\hat{h}^t_\beta - \frac{\partial}{\partial x_\beta}\frac{\hat{k}}{\eta}\hat{f}^f_\beta + \hat{q}^i.\end{aligned} \tag{2-77}$$

$\hat{E}_3$ is eliminated from Equation (2-67) and Equation (2-68) using Equation (2-58) to yield the following differential equations:

$$\frac{\partial \hat{E}_1}{\partial x_3} = -j\omega\mu_0\hat{H}_2 + \frac{\partial}{\partial x_1}\frac{1}{j\omega\hat{\varepsilon}_{\mathcal{L}}}\left(\frac{\partial \hat{H}_2}{\partial x_1} - \frac{\partial \hat{H}_1}{\partial x_2}\right) - \frac{\partial}{\partial x_1}\frac{\hat{\rho}^E\hat{\mathcal{L}}}{\hat{\varepsilon}_{\mathcal{L}}}\hat{w}_3 - \hat{J}^m_2 - \frac{\partial}{\partial x_1}\frac{1}{j\omega\hat{\varepsilon}_{\mathcal{L}}}\hat{J}^e_3 \tag{2-78}$$

and

$$\frac{\partial \hat{E}_2}{\partial x_3} = j\omega\mu_0\hat{H}_1 + \frac{\partial}{\partial x_2}\frac{1}{j\omega\hat{\varepsilon}_{\mathcal{L}}}\left(\frac{\partial \hat{H}_2}{\partial x_1} - \frac{\partial \hat{H}_1}{\partial x_2}\right) - \frac{\partial}{\partial x_2}\frac{\hat{\rho}^E\hat{\mathcal{L}}}{\hat{\varepsilon}_{\mathcal{L}}}\hat{w}_3 + \hat{J}^m_1 - \frac{\partial}{\partial x_2}\frac{1}{j\omega\hat{\varepsilon}_{\mathcal{L}}}\hat{J}^e_3. \tag{2-79}$$

Finally, $\hat{H}_3$ and $\hat{w}_\alpha$ are removed from Equations (2-69) and (2-70) using Equations (2-62) and (2-47). This results in

$$\begin{aligned}\frac{\partial \hat{H}_2}{\partial x_3} &= -j\omega\hat{\varepsilon}_{\mathcal{L}}\hat{E}_1 + \frac{\eta}{\hat{k}}\hat{\mathcal{L}}\left[j\omega\rho^f\frac{\hat{k}}{\eta}\hat{v}^s_1 + \frac{\hat{k}}{\eta}\left(\frac{\partial \hat{p}}{\partial x_1} - \hat{f}^f_1\right) - \hat{\mathcal{L}}\hat{E}_1\right] \\ &\quad - \hat{J}^e_1 + \frac{1}{j\omega\mu_0}\frac{\partial}{\partial x_2}\left(\frac{\partial \hat{E}_1}{\partial x_2} - \frac{\partial \hat{E}_2}{\partial x_1}\right) - \frac{1}{j\omega\mu_0}\frac{\partial \hat{J}^m_3}{\partial x_2}\end{aligned} \tag{2-80}$$

and

$$\begin{aligned}\frac{\partial \hat{H}_1}{\partial x_3} &= j\omega\hat{\varepsilon}_{\mathcal{L}}\hat{E}_2 - \frac{\eta}{\hat{k}}\hat{\mathcal{L}}\left[j\omega\rho^f\frac{\hat{k}}{\eta}\hat{v}^s_2 + \frac{\hat{k}}{\eta}\left(\frac{\partial \hat{p}}{\partial x_2} - \hat{f}^f_2\right) - \hat{\mathcal{L}}\hat{E}_2\right] \\ &\quad - \hat{J}^e_2 - \frac{1}{j\omega\mu_0}\frac{\partial}{\partial x_1}\left(\frac{\partial \hat{E}_1}{\partial x_2} - \frac{\partial \hat{E}_2}{\partial x_1}\right) + \frac{1}{j\omega\mu_0}\frac{\partial \hat{J}^m_3}{\partial x_1}.\end{aligned} \tag{2-81}$$

Equations (2-65), (2-73), (2-76), (2-77), (2-78), (2-79), (2-80) and (2-81) are combined in the form of the seismoelectric two-way wave equation,

$$\frac{\partial \hat{\mathbf{q}}}{\partial x_3} = \hat{\mathbf{A}}\hat{\mathbf{q}} + \hat{\mathbf{d}}. \tag{2-82}$$

The equations listed above express the vertical derivatives of the continous field quantities as a function of these quantities multiplied by a system matrix, $\hat{\mathbf{A}}$, and supplemented by a source vector. The order of the wave vector $\hat{\mathbf{q}}$ is specifically chosen such that the system matrix in 2-D will have a block diagonal matrix structure,

$$\hat{\mathbf{A}}^{\text{2-D}} = \begin{pmatrix} \hat{\mathbf{A}}^{11} & \mathbf{0} \\ \mathbf{0} & \hat{\mathbf{A}}^{22} \end{pmatrix}, \tag{2-83}$$

and such that the main diagonal block square matrices have the following off-diagonal block matrix structures,

$$\hat{\mathbf{A}}^{11} = \begin{pmatrix} \mathbf{0} & \hat{\mathbf{A}}^{11}_{12} \\ \hat{\mathbf{A}}^{11}_{21} & \mathbf{0} \end{pmatrix}, \ \hat{\mathbf{A}}^{22} = \begin{pmatrix} \mathbf{0} & \hat{\mathbf{A}}^{22}_{12} \\ \hat{\mathbf{A}}^{22}_{21} & \mathbf{0} \end{pmatrix}. \tag{2-84}$$

The motivation behind this choice of structure for the system matrix is to take advantage of the resulting symmetry properties and thereby simplify the linear algebra involved when decomposing the system into its upgoing and downgoing components, as elaborated on in Chapter 3 (Ursin, 1983). To create the desired structure, the wave vector $\hat{\mathbf{q}}$ is defined as

$$\hat{\mathbf{q}} = \left(-\hat{\tau}^b_{23}, -\hat{H}_1, \hat{v}^s_2, -\hat{E}_2, \hat{v}^s_3, \hat{w}_3, \hat{\tau}^b_{13}, \hat{H}_2, -\hat{\tau}^b_{33}, \hat{p}, \hat{v}^s_1, \hat{E}_1\right)^t , \tag{2-85}$$

leading to a source vector of

$$\hat{\mathbf{d}} = \begin{pmatrix} \hat{f}^b_2 - \frac{\rho^f}{\hat{\rho}^E}\hat{f}^f_2 - \frac{1}{j\omega}\left(\frac{\partial}{\partial x_1}G^{\text{fr}}(\hat{\text{h}}_{12} + \hat{\text{h}}_{21}) - \frac{\partial}{\partial x_2}\left(2G^{\text{fr}}\hat{\text{h}}_{22} + (S - \frac{S^2}{\text{K}_C})(\hat{\text{h}}_{11} + \hat{\text{h}}_{22})\right)\right) \\ -\hat{J}^e_2 - \hat{\mathcal{L}}\hat{f}^f_2 + \frac{\partial}{\partial x_1}\frac{1}{j\omega\mu_0}\hat{J}^m_3 \\ \hat{\text{h}}_{23} + \hat{\text{h}}_{32} \\ -\hat{J}^m_1 + \frac{\partial}{\partial x_2}\frac{1}{j\omega\hat{\epsilon}_{\mathcal{L}}}\hat{J}^e_3 \\ \hat{\text{h}}_{33} + (\frac{S}{\text{K}_C})(\hat{\text{h}}_{11} + \hat{\text{h}}_{22}) \\ -\frac{\partial}{\partial x_\beta}\frac{\hat{k}}{\eta}\hat{f}^f_\beta + \frac{C}{M}\text{u}^t_{i\beta}\hat{h}_{k\beta} + \hat{\text{q}}^i \\ -\hat{f}^b_1 + \frac{\rho^f}{\hat{\rho}^E}\hat{f}^f_1 + \frac{1}{j\omega}\left(\frac{\partial}{\partial x_2}G^{\text{fr}}(\hat{\text{h}}_{12} + \hat{\text{h}}_{21}) - \frac{\partial}{\partial x_1}\left(2G^{\text{fr}}\hat{\text{h}}_{11} + (S - \frac{S^2}{\text{K}_C})(\hat{\text{h}}_{11} + \hat{\text{h}}_{22})\right)\right) \\ -\hat{J}^e_1 - \hat{\mathcal{L}}\hat{f}^f_1 - \frac{\partial}{\partial x_2}\frac{1}{j\omega\mu_0}\hat{J}^m_3 \\ \hat{f}^b_3 - \frac{\rho^f}{\hat{\rho}^E}\hat{f}^f_3 \\ \hat{f}^f_3 - \frac{1}{j\omega\hat{\epsilon}_{\mathcal{L}}}\hat{\mathcal{L}}\frac{\eta}{\hat{k}}\hat{J}^e_3 \\ \hat{\text{h}}_{31} + \hat{\text{h}}_{13} \\ -\hat{J}^m_2 - \frac{\partial}{\partial x_1}\frac{1}{j\omega\hat{\varepsilon}_{\mathcal{L}}}\hat{J}^e_3 \end{pmatrix}. \tag{2-86}$$

The system matrix in 3D, $\hat{\mathbf{A}}$, can be subdivided into a number of submatrices,

$$\hat{\mathbf{A}} = \begin{pmatrix} \hat{\mathbf{A}}_{11} & \hat{\mathbf{A}}_{12} & \hat{\mathbf{A}}_{13} \\ \hat{\mathbf{A}}_{21} & \hat{\mathbf{A}}_{22} & \hat{\mathbf{A}}_{23} \\ \hat{\mathbf{A}}_{31} & \hat{\mathbf{A}}_{32} & \hat{\mathbf{A}}_{33} \end{pmatrix}. \tag{2-87}$$

The above ordering of the wave vector will facililate the decoupling of the system into the SH-TE and P-SV-TM modes, as presented in Section 2-4. The submatrices of $\hat{\mathbf{A}}$ are given by

$\hat{\mathbf{A}}_{11} =$

$$\begin{pmatrix} 0 & 0 & -j\omega\hat{\rho}^c + \frac{1}{jw}(\frac{\partial}{\partial x_1}(G_{\text{fr}}\frac{\partial}{\partial x_1}\cdot) + \frac{\partial}{\partial x_2}(\nu_1\frac{\partial}{\partial x_2}\cdot)) & j\omega\rho^f\hat{\mathcal{L}} \\ 0 & 0 & j\omega\rho^f\hat{\mathcal{L}} & j\omega\hat{\epsilon} - \frac{1}{j\omega}\frac{\partial}{\partial x_1}(\frac{1}{\mu_0}\frac{\partial}{\partial x_1}\cdot) \\ -\frac{j\omega}{G_{\text{fr}}} & 0 & 0 & 0 \\ 0 & j\omega\mu_0 - \frac{1}{j\omega}\frac{\partial}{\partial x_2}(\frac{1}{\hat{\epsilon}_{\mathcal{L}}}\frac{\partial}{\partial x_2}\cdot) & 0 & 0 \end{pmatrix}, \tag{2-88}$$

$$\hat{\mathbf{A}}_{12} = \begin{pmatrix} 0 & 0 & 0 & 0 \\ 0 & 0 & 0 & 0 \\ -\frac{\partial}{\partial x_2} & 0 & 0 & 0 \\ 0 & \frac{\partial}{\partial x_2}(\frac{\hat{\rho}^E}{\hat{\epsilon}_{\mathcal{L}}}\hat{\mathcal{L}}\cdot) & 0 & -\frac{1}{j\omega}\frac{\partial}{\partial x_2}(\frac{1}{\hat{\epsilon}_{\mathcal{L}}}\frac{\partial}{\partial x_1}\cdot) \end{pmatrix},$$

$$\hat{\mathbf{A}}_{13} =$$

$$\begin{pmatrix} -\frac{\partial}{\partial x_2}(\frac{S}{K_c}\cdot) & \frac{\rho^f}{\hat{\rho}^E}\frac{\partial}{\partial x_2} - \frac{\partial}{\partial x_2}(\frac{2CG_{\text{fr}}}{MK_c}\cdot) & \frac{1}{jw}(\frac{\partial}{\partial x_2}(\nu_2\frac{\partial}{\partial x_1}\cdot) + \frac{\partial}{\partial x_1}(G_{\text{fr}}\frac{\partial}{\partial x_2}\cdot)) & 0 \\ 0 & \hat{\mathcal{L}}\frac{\partial}{\partial x_2} & 0 & -\frac{1}{j\omega}\frac{\partial}{\partial x_1}(\frac{1}{\mu_0}\frac{\partial}{\partial x_2}\cdot) \\ 0 & 0 & 0 & 0 \\ 0 & 0 & 0 & 0 \end{pmatrix}, \tag{2-89}$$

$$\hat{\mathbf{A}}_{21} = \begin{pmatrix} 0 & 0 & -(\frac{S}{K_c})\frac{\partial}{\partial x_2} & 0 \\ 0 & 0 & \frac{\partial}{\partial x_2}(\frac{\rho^f}{\hat{\rho}^E}\cdot) - \frac{2CG^{\text{fr}}}{MK_c}\frac{\partial}{\partial x_2} & \frac{\partial}{\partial x_2}(\hat{\mathcal{L}}\cdot) \\ 0 & 0 & -\frac{1}{jw}(\frac{\partial}{\partial x_2}(G_{\text{fr}}\frac{\partial}{\partial x_1}\cdot) - \frac{\partial}{\partial x_1}(\nu_2\frac{\partial}{\partial x_2}\cdot) & 0 \\ 0 & 0 & 0 & \frac{1}{j\omega}\frac{\partial}{\partial x_2}(\frac{1}{\mu_0}\frac{\partial}{\partial x_1}\cdot) \end{pmatrix}, \tag{2-90}$$

$$\hat{\mathbf{A}}_{23} = \begin{pmatrix} -\frac{j\omega}{K_c} & \frac{j\omega C}{MK_c} & -(\frac{S}{K_c})\frac{\partial}{\partial x_1} & 0 \\ \frac{j\omega C}{MK_c} & -j\omega(\frac{C^2}{M^2K_c} + \frac{1}{M}) + \frac{\partial}{\partial x_\beta}(\frac{1}{j\omega\hat{\rho}^E}\frac{\partial}{\partial x_\beta}\cdot) & \frac{\partial}{\partial x_1}(\frac{\rho^f}{\hat{\rho}^E}\cdot) - \frac{2CG^{\text{fr}}}{MK_c}\frac{\partial}{\partial x_1} & -\frac{\partial}{\partial x_1}(\hat{\mathcal{L}}\cdot) \\ (\frac{S}{K_c})\frac{\partial}{\partial x_1} & -\frac{\partial}{\partial x_1}(\frac{\rho^f}{\hat{\rho}^E}\cdot) + \frac{2CG^{\text{fr}}}{MK_c}\frac{\partial}{\partial x_1} & j\omega\hat{\rho}^c - \frac{1}{jw}(\frac{\partial}{\partial x_1}(\nu_1\frac{\partial}{\partial x_1}\cdot) - \frac{\partial}{\partial x_2}(G^{\text{fr}}\frac{\partial}{\partial x_2}\cdot)) & j\omega\rho^f\hat{\mathcal{L}} \\ 0 & \frac{\partial}{\partial x_1}(\hat{\mathcal{L}}\cdot) & j\omega\rho^f\hat{\mathcal{L}} & -j\omega\hat{\epsilon} + \frac{1}{j\omega}\frac{\partial}{\partial x_2}(\frac{1}{\mu_0}\frac{\partial}{\partial x_2}\cdot) \end{pmatrix}, \tag{2-91}$$

$$\hat{\mathbf{A}}_{31} = \begin{pmatrix} -\frac{\partial}{\partial x_2} & 0 & 0 & 0 \\ 0 & \frac{\hat{\rho}^E}{\hat{\epsilon}_{\mathcal{L}}}\hat{\mathcal{L}}\frac{\partial}{\partial x_2} & 0 & 0 \\ 0 & 0 & 0 & 0 \\ 0 & \frac{1}{j\omega}\frac{\partial}{\partial x_1}(\frac{1}{\hat{\epsilon}_{\mathcal{L}}}\frac{\partial}{\partial x_2}\cdot) & 0 & 0 \end{pmatrix}, \tag{2-92}$$

$$\hat{\mathbf{A}}_{32} = \begin{pmatrix} -j\omega\rho^b & -j\omega\rho^f & \frac{\partial}{\partial x_1} & 0 \\ -j\omega\rho^f & -j\omega\hat{\rho}^E(1+\frac{\hat{\rho}^E}{\hat{\epsilon}_\mathcal{L}}\hat{\mathcal{L}}^2) & 0 & \frac{\hat{\rho}^E}{\hat{\epsilon}_\mathcal{L}}\hat{\mathcal{L}}\frac{\partial}{\partial x_1} \\ -\frac{\partial}{\partial x_1} & 0 & \frac{j\omega}{G^{\mathrm{fr}}} & 0 \\ 0 & -\frac{\partial}{\partial x_1}(\frac{\hat{\rho}^E}{\hat{\epsilon}_\mathcal{L}}\hat{\mathcal{L}}\cdot) & 0 & -j\omega\mu_0 + \frac{1}{j\omega}\frac{\partial}{\partial x_1}(\frac{1}{\hat{\epsilon}_\mathcal{L}}\frac{\partial}{\partial x_1}\cdot) \end{pmatrix}, \tag{2-93}$$

where $\hat{\rho}^c$ is a complex density,

$$\hat{\rho}^c = \rho^b - \frac{(\rho^f)^2}{\hat{\rho}^E}, \tag{2-94}$$

and where the following representations are also introduced,

$$\nu_1 = 4G^{\mathrm{fr}}\left(\frac{S+G^{\mathrm{fr}}}{K_c}\right), \tag{2-95}$$

$$\nu_2 = 2G^{\mathrm{fr}}\left(\frac{S}{K_c}\right), \tag{2-96}$$

$$K_c = S + 2G^{\mathrm{fr}}. \tag{2-97}$$

Note that $\hat{\mathbf{A}}_{22}$ and $\hat{\mathbf{A}}_{33}$ are 4×4 null matrices. It can be seen that the entries of $\hat{\mathbf{A}}_{12}$, $\hat{\mathbf{A}}_{13}$, $\hat{\mathbf{A}}_{21}$ and $\hat{\mathbf{A}}_{31}$ are all zero when the derivatives in the x_2 direction are set to zero.
The wave vector contains the field quantities that are continuous over a source-free interface: the $-\tau^b_{i1}, -\tau^b_{i2}, E_3, H_3, w_1$ and w_2 fields were eliminated. From the governing equations, it is clear that these eliminated quantities can be expressed in terms of the considered field quantities according to the following relations,

$$-\hat{\tau}^b_{i1} = \frac{1}{j\omega}\left(\mathrm{e}_{i1kl}h^b_{kl} - \mathrm{e}_{i1kl}\frac{\partial\hat{v}^s_i}{\partial x_l} + j\omega\frac{C}{M}\delta_{i1}\hat{p}\right), \tag{2-98}$$

$$-\hat{\tau}^b_{i2} = \frac{1}{j\omega}\left(\mathrm{e}_{i2kl}h^b_{kl} - \mathrm{e}_{i2kl}\frac{\partial\hat{v}^s_i}{\partial x_l} + j\omega\frac{C}{M}\delta_{i2}\hat{p}\right), \tag{2-99}$$

$$\hat{E}_3 = \frac{1}{j\omega\hat{\varepsilon}_\mathcal{L}}\left(\frac{\partial\hat{H}_1}{\partial x_2} - \frac{\partial\hat{H}_2}{\partial x_1} - \frac{\eta}{\hat{k}}\hat{\mathcal{L}}\hat{w}_3 - \hat{J}^e_3\right), \tag{2-100}$$

$$\hat{H}_3 = \frac{1}{j\omega\mu_0}\left(\frac{\partial\hat{E}_1}{\partial x_2} - \frac{\partial\hat{E}_2}{\partial x_1} - \hat{J}^m_3\right), \tag{2-101}$$

$$\hat{w_1} = \frac{\hat{k}}{\eta}\left(\hat{f}^f_1 - j\omega\rho^f\hat{v}^s_1 - \frac{\partial\hat{p}}{\partial x_1}\right) + \hat{\mathcal{L}}\hat{E}_1, \tag{2-102}$$

$$\hat{w_2} = \frac{\hat{k}}{\eta}\left(\hat{f}^f_2 - j\omega\rho^f\hat{v}^s_2 - \frac{\partial\hat{p}}{\partial x_2}\right) + \hat{\mathcal{L}}\hat{E}_2. \tag{2-103}$$

2-4 Decoupled SH-TE and P-SV-TM systems

Up to this point we have considered a three-dimensional wave propagation problem in a horizontally layered, isotropic medium with homogeneous subdomains. Setting the vertical axis as the "preferred direction of progation", allowed us to express changes in the vertical components of the wave vector quantities in terms of lateral changes in those field quanitites and contributions from source terms. The mechanical waves, both longitudinal and transverse, and the electromagnetic waves are fully coupled. The electromagnetic field can be expressed as the sum of transverse electric and transverse magnetic modes. TE-modes do not have an electric field in the direction of propagation, whereas-TM modes do not have a magnetic field in the direction of propagation.

In horizontally layered media the seismoelectric system can be separated into two independent systems: SH-TE and P-SV-TM. Horizontally polarized shear waves generate electrical currents that are coupled to transverse electric polarized electromagnetic waves while both compressional waves and vertically polarized shear waves generate currents that are coupled to transverse magnetic polarized electromagnetic waves (Haartsen and Pride, 1997).

We now consider waves propagating in the x_1x_3 plane, where x_3 is defined positive downwards, with line sources in the x_2 direction (De Ridder, 2007): all x_2 derivatives are set to zero. The TE-mode is represented by its $\hat{H}_1$, $\hat{E}_2$ and $\hat{H}_3$ components, while the TM-mode is represented by the complementary $\hat{E}_1$, $\hat{H}_2$ and $\hat{E}_3$ components.

The previous organization of the wave vector now facilitates decoupling the SH-TE system from the P-SV-TM system. We can express the decoupled components of the seismoelectric wave equation as follows:

$$\hat{\mathbf{q}} = \begin{pmatrix} \hat{\mathbf{q}}_{\mathrm{H}} \\ \hat{\mathbf{q}}_{\mathrm{V}} \end{pmatrix}, \tag{2-104}$$

where

$$\hat{\mathbf{q}}_{\mathrm{H}} = (-\hat{\tau}^b_{23}, -\hat{H}_1, \hat{v}^s_2, -\hat{E}_2)^t, \tag{2-105}$$

$$\hat{\mathbf{q}}_{\mathrm{V}} = (\hat{v}^s_3, \hat{w}_3, \hat{\tau}^b_{13}, \hat{H}_2, -\hat{\tau}^b_{33}, \hat{p}, \hat{v}^s_1, \hat{E}_1)^t; \tag{2-106}$$

and

$$\hat{\mathbf{A}} = \begin{pmatrix} \hat{\mathbf{A}}_{\mathrm{H}} & \mathbf{0} \\ \mathbf{0} & \hat{\mathbf{A}}_{\mathrm{V}} \end{pmatrix} = \begin{pmatrix} \mathbf{0}_{2\times 2} & \hat{\mathbf{A}}_{12,\mathrm{H}} & & \\ \hat{\mathbf{A}}_{21,\mathrm{H}} & \mathbf{0}_{2\times 2} & \multicolumn{2}{c}{0^{4\times 8}} \\ \multicolumn{2}{c}{0^{4\times 8}} & \mathbf{0}_{4\times 4} & \hat{\mathbf{A}}_{12,\mathrm{V}} \\ & & \hat{\mathbf{A}}_{21,\mathrm{V}} & \mathbf{0}_{4\times 4} \end{pmatrix}, \tag{2-107}$$

where $\hat{\mathbf{A}}_{\mathrm{H}}$ is determined from $\hat{\mathbf{A}}_{11}$ of Equation (2-88), while $\hat{\mathbf{A}}_{12,\mathrm{V}}$ and $\hat{\mathbf{A}}_{21,\mathrm{V}}$ follow from $\hat{\mathbf{A}}_{23}$ and $\hat{\mathbf{A}}_{32}$ of Equations (2-91) and (2-93), respectively. Setting the x_2 derivatives to zero results in the following submatrices,

$$\hat{\mathbf{A}}_{12,\mathrm{H}} = \begin{pmatrix} -j\omega\hat{\rho}^c + \frac{1}{j\omega}(\frac{\partial}{\partial x_1}(G^{\mathrm{fr}}(\frac{\partial}{\partial x_1}\cdot))) & j\omega\rho^f\hat{\mathcal{L}} \\ j\omega\rho^f\hat{\mathcal{L}} & j\omega\hat{\epsilon} - \frac{1}{j\omega}(\frac{\partial}{\partial x_1}(\frac{1}{\mu_0}(\frac{\partial}{\partial x_1}\cdot))) \end{pmatrix}, \tag{2-108}$$

$$\hat{\mathbf{A}}_{21,\mathrm{H}} = \begin{pmatrix} -\frac{j\omega}{G^{\mathrm{fr}}} & 0 \\ 0 & j\omega\mu_0 \end{pmatrix}, \tag{2-109}$$

$$\hat{\mathbf{A}}_{12,\mathrm{V}} = \begin{pmatrix} -\frac{j\omega}{\mathrm{K}_C} & \frac{j\omega C}{M\mathrm{K}_C} & -(\frac{S}{K_c})\frac{\partial}{\partial x_1} & 0 \\ \frac{j\omega C}{M\mathrm{K}_C} & -j\omega(\frac{C^2}{M^2K_C} + \frac{1}{M}) + \frac{\partial}{\partial x_1}(\frac{1}{j\omega\hat{\rho}^E}\frac{\partial}{\partial x_1}\cdot) & \frac{\partial}{\partial x_1}(\frac{\rho^f}{\hat{\rho}^E}\cdot) - \frac{2CG^{\mathrm{fr}}}{MK_C}\frac{\partial}{\partial x_1} & -\frac{\partial}{\partial x_1}(\hat{\mathcal{L}}\cdot) \\ (\frac{S}{K_c})\frac{\partial}{\partial x_1} & -\frac{\partial}{\partial x_1}(\frac{\rho^f}{\hat{\rho}^E}\cdot) + \frac{2CG^{\mathrm{fr}}}{MK_C}\frac{\partial}{\partial x_1} & j\omega\hat{\rho}^c + \frac{1}{jw}(\frac{\partial}{\partial x_1}(\nu_1\frac{\partial}{\partial x_1}\cdot) & j\omega\rho^f\hat{\mathcal{L}} \\ 0 & \frac{\partial}{\partial x_1}(\hat{\mathcal{L}}\cdot) & j\omega\rho^f\hat{\mathcal{L}} & -j\omega\hat{\varepsilon} \end{pmatrix}, \tag{2-110}$$

$$
\hat{\mathbf{A}}_{21,\mathrm{V}} = \begin{pmatrix} -j\omega\rho^b & -j\omega\rho^f & \frac{\partial}{\partial x_1} & 0 \\ -j\omega\rho^f & -j\omega\hat{\rho}^E\left(1+\frac{\hat{\rho}^E\hat{\mathcal{L}}^2}{\hat{\varepsilon}_{\mathcal{L}}}\right) & 0 & \frac{\hat{\rho}^E}{\hat{\epsilon}_{\mathcal{L}}}\hat{\mathcal{L}}\frac{\partial}{\partial x_1} \\ -\frac{\partial}{\partial x_1} & 0 & \frac{j\omega}{G^{\mathrm{fr}}} & 0 \\ 0 & -\frac{\hat{\rho}^E}{\hat{\epsilon}_{\mathcal{L}}}\hat{\mathcal{L}}\frac{\partial}{\partial x_1} & 0 & -j\omega\mu_0+\frac{1}{j\omega}\frac{\partial}{\partial x_1}(\frac{1}{\hat{\epsilon}_{\mathcal{L}}}\frac{\partial}{\partial x_1}\cdot) \end{pmatrix}. \tag{2-111}
$$

The source vector is similarly rearranged,

$$
\hat{\mathbf{d}} = \begin{pmatrix} \hat{\mathbf{d}}_{\mathrm{H}} \\ \hat{\mathbf{d}}_{\mathrm{V}} \end{pmatrix}, \tag{2-112}
$$

where

$$
\hat{\mathbf{d}}_{\mathrm{H}} = \begin{pmatrix} \hat{f}_2^b - \frac{\rho^f}{\hat{\rho}^E}\hat{f}_2^f - \frac{1}{j\omega}\frac{\partial}{\partial x_1}G^{\mathrm{fr}}(\hat{\mathrm{h}}_{12}+\hat{\mathrm{h}}_{21}) \\ -\hat{J}_2^e - \hat{\mathcal{L}}\hat{f}_2^f + \frac{\partial}{\partial x_1}\frac{1}{j\omega\mu_0}\hat{J}_3^m \\ \hat{\mathrm{h}}_{23}+\hat{\mathrm{h}}_{32} \\ -\hat{J}_1^m \end{pmatrix}, \tag{2-113}
$$

$$
\hat{\mathbf{d}}_{\mathrm{V}} = \begin{pmatrix} \hat{\mathrm{h}}_{33} + (\frac{S}{\mathrm{K}_C})(\hat{\mathrm{h}}_{11}+\hat{\mathrm{h}}_{22}) \\ \hat{\mathrm{q}}^i - \frac{\partial}{\partial x_1}\frac{1}{j\omega\hat{\rho}^E}\hat{f}_1^f \\ -\hat{f}_1^b + \frac{\rho^f}{\hat{\rho}^E}\hat{f}_1^f + \frac{1}{j\omega}\frac{\partial}{\partial x_1}\left(2G^{\mathrm{fr}}\hat{\mathrm{h}}_{11} + (S-\frac{S^2}{\mathrm{K}_C})(\hat{\mathrm{h}}_{11}+\hat{\mathrm{h}}_{22})\right) \\ -\hat{J}_1^e - \hat{\mathcal{L}}\hat{f}_1^f \\ -\hat{f}_3^b + \frac{\rho^f}{\hat{\rho}^E}\hat{f}_3^f \\ -\hat{f}_3^f + \frac{\hat{\rho}^E}{\hat{\varepsilon}_{\mathcal{L}}}\hat{\mathcal{L}}\hat{J}_3^e \\ \hat{\mathrm{h}}_{31}+\hat{\mathrm{h}}_{13} \\ -\hat{J}_2^m - \frac{\partial}{\partial x_1}\frac{1}{j\omega\hat{\varepsilon}_{\mathcal{L}}}\hat{J}_3^e \end{pmatrix}. \tag{2-114}
$$

2-5 Symmetry Properties

It can be seen that the two-way system matrix $\hat{\mathbf{A}}$ and the decoupled SH-TE and P-SV-TM submatrices obey the following symmetry relation,

$$
\hat{\mathbf{A}}^{\mathbf{t}}\mathbf{N} = -\mathbf{N}\hat{\mathbf{A}}, \tag{2-115}
$$

where

$$
\mathbf{N} = \begin{pmatrix} \mathbf{0} & \mathbf{I} \\ -\mathbf{I} & \mathbf{0} \end{pmatrix}. \tag{2-116}
$$

The identity and null matrices are appropriately scaled for the system being considered. Note that we use the following mathematical property relating a spatial derivative to its transpose:

$$
\left(\frac{\partial}{\partial x_1}\right)^t = -\left(\frac{\partial}{\partial x_1}\right). \tag{2-117}
$$

Chapter 3

Seismoelectric decomposition for the P-SV-TM system

In this chapter we continue from our derivation of the decoupled 2-D P-SV-TM system. The wave velocities of the four wavetypes (Pf, Ps, SV, TM) can be derived from the system matrix and are presented. We then perform an eigendecomposition on the system matrix, further decomposing the system into a product of matrices consisting of its eigenvectors and eigenvalues. The eight eigenvectors of the P-SV-TM system, corresponding to downgoing and upgoing waves of each of the four wavetypes, are composed into a composition matrix. To take advantage of one-way reciprocity theorems, the composition matrix is flux-normalized. After presenting the flux-normalized composition matrix, we show the relation between the composition matrix and its inverse, the decomposition matrix.
An introduction to one-way wave theory is presented. It is shown that the one-way wave and source vectors can be obtained through the action of the flux-normalized decomposition matrix on the two-way wave vector. In an analogous fashion, the composition matrix composes the two-way field quantities from their downgoing and upgoing one-way wave vector constituents. We then determine the eigenvalues and eigenvectors for the special situation of the P-SV-TM system in a vacuum, again deriving the corresponding flux-normalized composition matrices. The composition and decomposition matrices for both the porous medium and the vacuum domain are used in Chapter 4 to determine the reflection coefficients for incident wavefields at both porous-porous and porous-vacuum interfaces.

3-1 Decoupled system matrix

The 2-D P-SV-TM system from the previous chapter is transformed from the (x_1, x_3, w) domain to the (k_1, x_3, w) domain through the application of a 1-D horizontal spatial Fourier transformation. In the wavenumber-frequency domain, the wave vector and system matrix are written as follows,

$$\tilde{\mathbf{q}}_{\mathrm{V}} = (\tilde{v}_3^s, \tilde{w}_3, \tilde{\tau}_{13}^b, \tilde{H}_2, -\tilde{\tau}_{33}^b, \tilde{p}, \tilde{v}_1^s, \tilde{E}_1)^t, \tag{3-1}$$

and

$$\tilde{\mathbf{A}}_{\mathrm{V}} = \begin{pmatrix} \mathbf{0} & \tilde{\mathbf{A}}_{12,\mathrm{V}} \\ \tilde{\mathbf{A}}_{21,\mathrm{V}} & \mathbf{0} \end{pmatrix}, \tag{3-2}$$

where

$$\tilde{\mathbf{A}}_{12,\mathrm{V}} = \begin{pmatrix} -\frac{j\omega}{\mathrm{K}_C} & \frac{j\omega C}{M\mathrm{K}_C} & \frac{jk_1 S}{\mathrm{K}_C} & 0 \\ \frac{j\omega C}{M\mathrm{K}_C} & \frac{jk_1^2}{\omega\hat{\rho}^E} - j\omega\left(\frac{C^2}{M^2\mathrm{K}_C} + \frac{1}{M}\right) & \frac{2jk_1 C G^{\mathrm{fr}}}{M\mathrm{K}_C} - \frac{jk_1\rho^f}{\hat{\rho}^E} & jk_1\hat{\mathcal{L}} \\ -\frac{jk_1 S}{\mathrm{K}_C} & \frac{jk_1\rho^f}{\hat{\rho}^E} - \frac{2jk_1 C G^{\mathrm{fr}}}{M\mathrm{K}_C} & j\omega\hat{\rho}^c - \frac{jk_1^2\nu_1}{\omega} & j\omega\rho^f\hat{\mathcal{L}} \\ 0 & -jk_1\hat{\mathcal{L}} & j\omega\rho^f\hat{\mathcal{L}} & -j\omega\hat{\varepsilon} \end{pmatrix}, \tag{3-3}$$

$$\tilde{\mathbf{A}}_{21,\mathrm{V}} = \begin{pmatrix} -j\omega\rho^b & -j\omega\rho^f & -jk_1 & 0 \\ -j\omega\rho^f & -j\omega\hat{\rho}^E\left(1 + \frac{\hat{\rho}^E\hat{\mathcal{L}}^2}{\hat{\varepsilon}_{\mathcal{L}}}\right) & 0 & -\frac{jk_1\hat{\rho}^E\hat{\mathcal{L}}}{\hat{\varepsilon}_{\mathcal{L}}} \\ jk_1 & 0 & \frac{j\omega}{G^{\mathrm{fr}}} & 0 \\ 0 & \frac{jk_1\hat{\rho}^E\hat{\mathcal{L}}}{\hat{\varepsilon}_{\mathcal{L}}} & 0 & -j\omega\mu_0 + \frac{jk_1^2}{\omega\hat{\varepsilon}_{\mathcal{L}}} \end{pmatrix}. \tag{3-4}$$

The system matrix is further rewritten such that it only contains elastic parameters that were used by Haartsen and Pride (1997) in their derivation of the eigenvectors of the P-SV-TM system. We adopt Biot's stiffness parameters, where $H = \mathrm{K}_G + \frac{4G^{\mathrm{fr}}}{3}$ and $HM - C^2 = M(S + 2G^{\mathrm{fr}}) = M\mathrm{K}_C$. Using these relations and recalling that $\nu_1 = 4G^{\mathrm{fr}}\left(\frac{S+G^{\mathrm{fr}}}{\mathrm{K}_C}\right)$ allows us to recast $\tilde{\mathbf{A}}_{12,\mathrm{V}}$ as

$$\tilde{\mathbf{A}}_{12,\mathrm{V}} =$$

$$\begin{pmatrix} -\frac{j\omega M}{HM-C^2} & \frac{j\omega C}{HM-C^2} & jk_1\left(1 - \frac{2G^{\mathrm{fr}}M}{HM-C^2}\right) & 0 \\ \frac{j\omega C}{HM-C^2} & \frac{jk_1^2}{\omega\hat{\rho}^E} - \frac{j\omega H}{HM-C^2} & \frac{2jk_1 C G^{\mathrm{fr}}}{HM-C^2} - \frac{jk_1\rho^f}{\hat{\rho}^E} & jk_1\hat{\mathcal{L}} \\ -jk_1\left(1 - \frac{2G^{\mathrm{fr}}M}{HM-C^2}\right) & \frac{jk_1\rho^f}{\hat{\rho}^E} - \frac{2jk_1 C G^{\mathrm{fr}}}{HM-C^2} & j\omega\hat{\rho}^c - \frac{4jk_1^2 G^{\mathrm{fr}}}{\omega}\left(1 - \frac{G^{\mathrm{fr}}M}{HM-C^2}\right) & j\omega\rho^f\hat{\mathcal{L}} \\ 0 & -jk_1\hat{\mathcal{L}} & j\omega\rho^f\hat{\mathcal{L}} & -j\omega\hat{\varepsilon}_{\mathcal{L}}\left(1 + \frac{\hat{\rho}^E\hat{\mathcal{L}}^2}{\hat{\varepsilon}_{\mathcal{L}}}\right) \end{pmatrix}. \tag{3-5}$$

The application of the horizontal spatial Fourier transform allows us to rewrite the previous symmetry relation for the system matrix, Equation (2-115), as (Wapenaar, 1996; Slob, 2009)

$$\tilde{\mathbf{A}}^t(-k_1, x_3, \omega)\mathbf{N} = -\mathbf{N}\tilde{\mathbf{A}}(k_1, x_3, \omega). \tag{3-6}$$

The decoupled P-SV-TM source vector, Equation (2-114), is similarly reformulated to give

$$\tilde{\mathbf{d}}_{\mathrm{V}} = \begin{pmatrix} \tilde{\mathrm{h}}_{33} + \left(1 - \frac{2G^{\mathrm{fr}}M}{HM-C^2}\right)(\tilde{\mathrm{h}}_{11} + \tilde{\mathrm{h}}_{22}) \\ \tilde{\mathrm{q}}^i + \frac{k_1}{\omega\hat{\rho}^E}\tilde{f}_1^f \\ -\tilde{f}_1^b + \frac{\rho^f}{\hat{\rho}^E}\tilde{f}_1^f - \frac{2k_1 G^{\mathrm{fr}}}{\omega}\left(\tilde{\mathrm{h}}_{11} + \left(1 - \frac{2G^{\mathrm{fr}}M}{HM-C^2}\right)(\tilde{\mathrm{h}}_{11} + \tilde{\mathrm{h}}_{22})\right) \\ -\tilde{J}_1^e - \hat{\mathcal{L}}\tilde{f}_1^f \\ \tilde{f}_3^b - \frac{\rho^f}{\hat{\rho}^E}\tilde{f}_3^f \\ \tilde{f}_3^f - \frac{\hat{\rho}^E}{\hat{\varepsilon}_{\mathcal{L}}}\hat{\mathcal{L}}\tilde{J}_3^e \\ \tilde{\mathrm{h}}_{31} + \tilde{\mathrm{h}}_{13} \\ -\tilde{J}_2^m + \frac{k_1}{\omega\hat{\varepsilon}_{\mathcal{L}}}\tilde{J}_3^e \end{pmatrix}. \tag{3-7}$$

3-2 Wave velocities

Pride and Haartsen (1996) determined the complex velocities of the compressional waves, the vertically polarized shear wave and the electromagnetic wave for the P-SV-TM propagation mode to be:

$$\frac{2}{\hat{c}_{pf}^2} = \hat{\xi} - \sqrt{\hat{\xi}^2 - \frac{4\rho^b \hat{\rho}^E}{HM - C^2}\left(\frac{\hat{\rho}^c}{\rho^b} + \frac{\hat{\rho}^E \hat{\mathcal{L}}^2}{\hat{\varepsilon}_{\mathcal{L}}}\right)}, \tag{3-8}$$

$$\frac{2}{\hat{c}_{ps}^2} = \hat{\xi} + \sqrt{\hat{\xi}^2 - \frac{4\rho^b \hat{\rho}^E}{HM - C^2}\left(\frac{\hat{\rho}^c}{\rho^b} + \frac{\hat{\rho}^E \hat{\mathcal{L}}^2}{\hat{\varepsilon}_{\mathcal{L}}}\right)}, \tag{3-9}$$

$$\frac{2}{\hat{c}_{sv}^2} = \frac{\hat{\rho}^c}{G^{\text{fr}}} + \mu\hat{\varepsilon}_{\mathcal{L}}\left(1 + \frac{\hat{\rho}^E \hat{\mathcal{L}}^2}{\hat{\varepsilon}_{\mathcal{L}}}\right) + \sqrt{\left[\frac{\hat{\rho}^c}{G^{\text{fr}}} - \mu\hat{\varepsilon}_{\mathcal{L}}\left(1 + \frac{\hat{\rho}^E \hat{\mathcal{L}}^2}{\hat{\varepsilon}_{\mathcal{L}}}\right)\right]^2 - 4\mu\frac{(\rho^f)^2\hat{\mathcal{L}}^2}{G^{\text{fr}}}}, \tag{3-10}$$

$$\frac{2}{\hat{c}_{tm}^2} = \frac{\hat{\rho}^c}{G^{\text{fr}}} + \mu\hat{\varepsilon}_{\mathcal{L}}\left(1 + \frac{\hat{\rho}^E \hat{\mathcal{L}}^2}{\hat{\varepsilon}_{\mathcal{L}}}\right) - \sqrt{\left[\frac{\hat{\rho}^c}{G^{\text{fr}}} - \mu\hat{\varepsilon}_{\mathcal{L}}\left(1 + \frac{\hat{\rho}^E \hat{\mathcal{L}}^2}{\hat{\varepsilon}_{\mathcal{L}}}\right)\right]^2 - 4\mu\frac{(\rho^f)^2\hat{\mathcal{L}}^2}{G^{\text{fr}}}}, \tag{3-11}$$

where the parameter $\hat{\xi}$ is

$$\hat{\xi} = \frac{\rho^b M + \hat{\rho}^E H(1 + \hat{\rho}^E \hat{\mathcal{L}}^2/\hat{\varepsilon}_{\mathcal{L}}) - 2\rho^f C}{HM - C^2}. \tag{3-12}$$

Note that a negative sign is associated with the fast P-wave and a positive sign with the slow P-wave. If the coupling coefficient in the above equations is set to zero, the P-wave velocities would lead to those as defined by Biot (1956) and the transverse wave velocities would reduce to their usual definitions.
The real phase velocity of the waves is represented by the real part of their complex velocities,

$$V_w = \text{Re}(\hat{c}_w), \tag{3-13}$$

where the subscript w refer to either the fast P-wave (w = pf), the slow P-wave (w = ps), the vertically polarized shear wave (w = sv), or the transverse magnetic wave (w = tm). The imaginary part of the complex velocities describes the attenuation. The real attenuation coefficient, in units of inverse length, is given by (Haartsen and Pride, 1997)

$$\alpha_w = \frac{\omega}{\text{Im}(\hat{c}_w)}, \tag{3-14}$$

3-3 Eigendecomposition

The system matrix $\tilde{\mathbf{A}}$ of the two-way wave equation, Equation (2-45), can be decomposed into matrices consisting of its eigenvectors and eigenvalues,

$$\tilde{\mathbf{A}} = \tilde{\mathbf{L}}\tilde{\mathbf{H}}\tilde{\mathbf{L}}^{-1}, \tag{3-15}$$

where $\tilde{\mathbf{H}}$ is a diagonal matrix containing the eigenvalues of the system and where the columns of $\tilde{\mathbf{L}}$ contain the corresponding eigenvectors. The diagonal eigenvalue matrix can be written in block-matrix form as

$$\tilde{\mathbf{H}} = \begin{pmatrix} \tilde{\mathbf{H}}^+ & 0 \\ 0 & \tilde{\mathbf{H}}^- \end{pmatrix} = \begin{pmatrix} -\tilde{\mathbf{H}} & 0 \\ 0 & \tilde{\mathbf{H}} \end{pmatrix}, \tag{3-16}$$

where we considered $\tilde{\mathbf{H}}^{\pm} = \mp\tilde{\mathbf{H}}$. The diagonal elements of $\tilde{\mathbf{H}}$ represent the eigenvalues of the system, as given by the square root operator $\tilde{\mathcal{H}}$,

$$\tilde{\mathbf{H}}^{\pm} = \mp j\tilde{\mathcal{H}}_w = \mp j\sqrt{\frac{\omega^2}{c_w^2} - k_1^2}. \tag{3-17}$$

From the above expression, it can be seen that the square root operator represents the vertical wavenumber k_3. Since $\tilde{\mathcal{H}}_w$ represents a square root, it has two valid solutions and we must define the desired sign of the root. For reasons that will be discussed in Section 3-6, we desire that the real part of $\tilde{\mathbf{H}}$ be positive, corresponding to the imaginary part of $\tilde{\mathcal{H}}_w$ being negative. Therefore, we choose the negative-valued root of $\sqrt{\frac{\omega^2}{c_w^2} - k_1^2}$. Specifying a one-way wavefield ordering of $(pf+, ps+, sv+, tm+, pf-, ps-, sv-, tm-)$ allows the diagonal operator matrix to be explicitly given by

$$\tilde{\mathbf{H}} = \mathrm{diag}(j\tilde{\mathcal{H}}^+_{pf}, j\tilde{\mathcal{H}}^+_{ps}, j\tilde{\mathcal{H}}^+_{sv}, j\tilde{\mathcal{H}}^+_{tm}, j\tilde{\mathcal{H}}^-_{pf}, j\tilde{\mathcal{H}}^-_{ps}, j\tilde{\mathcal{H}}^-_{sv}, j\tilde{\mathcal{H}}^-_{tm}). \tag{3-18}$$

3-4 Eigenvectors

The eigenvectors of the P-SV-TM system were derived by Pride (1994) and, for our ordering of the wave vector, are given by

$$\tilde{\mathbf{a}}^{\pm}_m = \begin{bmatrix} \pm\tilde{q}_m c_m \\ \pm\tilde{q}_m \gamma_{Lm} c_m \\ \mp 2G^{\mathrm{fr}} p\tilde{q}_m c_m \\ 0 \\ (H - 2G^{\mathrm{fr}} p^2 c_m^2 + \gamma_{Lm} C)/c_m \\ (C + \gamma_{Lm} M)/c_m \\ pc_m \\ -\hat{\rho}^E \hat{\mathcal{L}} \hat{\gamma}_{Lm} p c_m / \hat{\varepsilon}_{\mathcal{L}} \end{bmatrix} \text{ and } \tilde{\mathbf{a}}^{\pm}_n = \begin{bmatrix} -pc_n \\ -p(G^{\mathrm{fr}} - c_n^2 \rho^b)/(\rho^f c_n) \\ -G^{\mathrm{fr}}(\tilde{q}_n^2 - p^2)c_n \\ -\hat{\rho}^E \hat{\mathcal{L}} \gamma_{Tn} G^{\mathrm{fr}}/(\rho^f c_n) \\ \mp 2G^{\mathrm{fr}} p\tilde{q}_n c_n \\ 0 \\ \pm\tilde{q}_n c_n \\ \mp\mu\hat{\rho}^E \hat{\mathcal{L}} G^{\mathrm{fr}} \hat{\gamma}_{Tn} \tilde{q}_n c_n/\rho^f \end{bmatrix} \tag{3-19}$$

where $m = (pf, ps)$ and $n = (sv, tm)$.

3-5 Composition matrix

We seek to arrange the eigenvectors of the P-SV-TM system into a composition matrix $\tilde{\mathbf{K}}$ that has the following structure,

$$\tilde{\mathbf{K}} = \begin{pmatrix} \tilde{\mathbf{K}}_1 & \tilde{\mathbf{K}}_1 \\ \tilde{\mathbf{K}}_2 & -\tilde{\mathbf{K}}_2 \end{pmatrix}, \tag{3-20}$$

where $\tilde{\mathbf{K}}_1$ and $\tilde{\mathbf{K}}_2$ are equally-sized submatrices of $\tilde{\mathbf{K}}$. To obtain this structure we redefine the upgoing fast and slow compressional wave eigenvectors with a sign switch from the original definitions. This results in the first four elements of the upgoing fast and slow compressional wave eigenvectors having the same sign as their downgoing counterparts, whereas the second half of the elements have a sign switch from their downgoing counterparts. Having created the desired structure of the composition matrix, we notationally drop the negative sign that was introduced into the columns corresponding to the upgoing compressional wave eigenvectors and present the ordering of $\tilde{\mathbf{K}}$ as

$$\tilde{\mathbf{K}} = (\tilde{\mathbf{a}}^+_{pf}, \tilde{\mathbf{a}}^+_{ps}, \tilde{\mathbf{a}}^+_{sv}, \tilde{\mathbf{a}}^+_{tm}, \tilde{\mathbf{a}}^-_{pf}, \tilde{\mathbf{a}}^-_{ps}, \tilde{\mathbf{a}}^-_{sv}, \tilde{\mathbf{a}}^-_{tm}). \tag{3-21}$$

The submatrices of $\tilde{\mathbf{K}}$ are defined by

$$\tilde{\mathbf{K}}_1 = \begin{pmatrix} \tilde{q}_{pf}c_{pf} & \tilde{q}_{ps}c_{ps} & -p_1c_{sv} & -p_1c_{tm} \\ \tilde{q}_{pf}c_{pf}\hat{\gamma}_{Lpf} & \tilde{q}_{ps}c_{ps}\hat{\gamma}_{Lps} & -p_1(G^{\text{fr}}-c_{sv}^2\rho^b)/(\rho^f c_{sv}) & -p_1(G^{\text{fr}}-c_{tm}^2\rho^b)/(\rho^f c_{tm}) \\ -2G^{\text{fr}}p_1q_{pf}c_{pf} & -2G^{\text{fr}}p_1q_{ps}c_{ps} & -G^{\text{fr}}(q_{sv}^2-p_1^2)c_{sv} & -G^{\text{fr}}(q_{tm}^2-p_1^2)c_{tm} \\ 0 & 0 & -\hat{\rho}^E\hat{\mathcal{L}}\hat{\gamma}_{Tsv}G^{\text{fr}}/(\rho^f c_{sv}) & -\hat{\rho}^E\hat{\mathcal{L}}\hat{\gamma}_{Ttm}G^{\text{fr}}/(\rho^f c_{tm}) \end{pmatrix} \tag{3-22}$$

and

$$\tilde{\mathbf{K}}_2 = \begin{pmatrix} (H-2G^{\text{fr}}p_1^2c_{pf}^2+\hat{\gamma}_{Lpf}C)/c_{pf} & (H-2G^{\text{fr}}p_1^2c_{ps}^2+\hat{\gamma}_{Lps}C)/c_{ps} & -2G^{\text{fr}}p_1\tilde{q}_{sv}c_{sv} & -2G^{\text{fr}}p_1\tilde{q}_{tm}c_{tm} \\ (C+\hat{\gamma}_{Lpf}M)/c_{pf} & (C+\hat{\gamma}_{Lps}M)/c_{ps} & 0 & 0 \\ p_1c_{pf} & p_1c_{ps} & \tilde{q}_{sv}c_{sv} & \tilde{q}_{tm}c_{tm} \\ -\hat{\rho}^E\hat{\mathcal{L}}\hat{\gamma}_{Lpf}p_1c_{pf}/\hat{\varepsilon}_{\mathcal{L}} & -\hat{\rho}^E\hat{\mathcal{L}}\hat{\gamma}_{Lps}p_1c_{ps}/\hat{\varepsilon}_{\mathcal{L}} & -\mu\hat{\rho}^E\hat{\mathcal{L}}G^{\text{fr}}\hat{\gamma}_{Tsv}\tilde{q}_{sv}c_{sv}/\rho^f & -\mu\hat{\rho}^E\hat{\mathcal{L}}G^{\text{fr}}\hat{\gamma}_{Ttm}\tilde{q}_{tm}c_{tm}/\rho^f \end{pmatrix}, \tag{3-23}$$

where

$$\hat{\gamma}_{Lm} = -\frac{(\frac{H}{c_m^2}-\rho^b)}{(\frac{C}{c_m^2}-\rho^f)} \text{ and } \hat{\gamma}_{Tn} = -\frac{(\frac{1}{c_n^2}-\frac{\rho^b}{G^{\text{fr}}})}{(\frac{1}{c_n^2}-\mu_0\hat{\varepsilon}_{\mathcal{L}})}. \tag{3-24}$$

We add an additional subscript of L and T to distinguish between longitudinal and transverse waves.
The following relation holds between the horizontal and vertical slownesses and the complex wavespeed:

$$p^2 + \tilde{q}_w^2 = \frac{1}{\hat{c}_w^2}, \tag{3-25}$$

where the horizontal slowness, p, can be seen as the horizontal counterpart to the vertical slowness represented by $\tilde{q}_w$. The vertical slowness can be related to the previously defined square-root operator by $\tilde{q}_w = \frac{\tilde{\mathcal{H}}_w}{\omega}$. In the 2-D case, as discussed in this thesis, the partial derivatives with respect to the x_2 direction have been set to zero, such that the radial ray parameter, p, can be replaced by the signed ray parameter, p_1, as used in Eq. (3-22) and Eq. (3-23).

3-5-1 Flux-normalized composition matrix

The above eigenvectors of Haartsen and Pride (1997) were normalized with respect to their solid displacements; however, alternative normalizations are possible. We choose a normalization based on conserving energy flux across interfaces (Frasier, 1970).
The flux-normalized composition matrix $\tilde{\mathbf{L}}$ can be found by multiplying the composition operator by a diagonal matrix, $\tilde{\mathbf{D}}$, according to $\tilde{\mathbf{L}} = \tilde{\mathbf{K}}\tilde{\mathbf{D}}$, where

$$\tilde{\mathbf{D}} = \begin{pmatrix} \tilde{\mathbf{D}}_1 & \mathbf{0} \\ \mathbf{0} & \tilde{\mathbf{D}}_2 \end{pmatrix}. \tag{3-26}$$

The elements of the diagonal matrix can be found by substituting the above relation for $\tilde{\mathbf{L}}$ into the following symmetry condition relating the inverse of the composition matrix to its transpose (Ursin, 1983):

$$\tilde{\mathbf{L}}^{-1}(p_1, x_3, w) = -\mathbf{N}^{-1}\tilde{\mathbf{L}}^t(-p_1, x_3, w)\mathbf{N}. \tag{3-27}$$

Carrying out the substitution results in

$$(\tilde{\mathbf{K}}(p_1, x_3, w)\tilde{\mathbf{D}})^{-1} = -\mathbf{N}^{-1}(\tilde{\mathbf{K}}(-p_1, x_3, w)\tilde{\mathbf{D}})^t\mathbf{N}, \tag{3-28}$$

and bringing the elements of $\tilde{\mathbf{L}}^{-1}$ to the right-hand side yields

$$\begin{aligned} \mathbf{I} &= -\,\mathbf{N}^{-1}\tilde{\mathbf{D}}^t\tilde{\mathbf{K}}^t(-p_1, x_3, w)\mathbf{N}\tilde{\mathbf{K}}(p_1, x_3, w)\tilde{\mathbf{D}}, \\ &= -\,\tilde{\mathbf{K}}(p_1, x_3, w)\tilde{\mathbf{D}}\mathbf{N}^{-1}\tilde{\mathbf{D}}^t\tilde{\mathbf{K}}^t(-p_1, x_3, w)\mathbf{N}. \end{aligned} \tag{3-29}$$

We find from the second equation that

$$2\tilde{\mathbf{K}}_1(p_1, x_3, w)\tilde{\mathbf{D}}_1\tilde{\mathbf{D}}_2\tilde{\mathbf{K}}_2^t(-p_1, x_3, w) = \mathbf{I}, \tag{3-30}$$

where $\tilde{\mathbf{D}}_1 = \mathrm{diag}(\tilde{d}_1, \tilde{d}_2, \tilde{d}_3, \tilde{d}_4)$ and $\tilde{\mathbf{D}}_2 = \mathrm{diag}(\tilde{d}_5, \tilde{d}_6, \tilde{d}_7, \tilde{d}_8)$. It can be seen that only products of the diagonal matrices occur (i.e. $\tilde{d}_1\tilde{d}_5$), indicating that the relatives values of the elements can be chosen. We choose to set $\tilde{\mathbf{D}}_1 = \tilde{\mathbf{D}}_2$, thereby improving the amplitude balance of the flux-normalized composition matrix. The second constraint on the diagonal elements is creating a final flux-normalized composition matrix that has the following symmetry:

$$\tilde{\mathbf{L}} = \begin{pmatrix} \tilde{\mathbf{L}}_1 & \tilde{\mathbf{L}}_1 \\ \tilde{\mathbf{L}}_2 & -\tilde{\mathbf{L}}_2 \end{pmatrix}. \tag{3-31}$$

With these contraints in mind, the diagonal elements are chosen to be

$$\tilde{d}_1 = \tilde{d}_5 = \left[2\tilde{q}_{pf}\left(H + 2\hat{\gamma}_{Lpf}C + \hat{\gamma}_{Lpf}^2 M\right)\right]^{-\frac{1}{2}}, \tag{3-32}$$

$$\tilde{d}_2 = \tilde{d}_6 = \left[2\tilde{q}_{ps}\left(H + 2\hat{\gamma}_{Lps}C + \hat{\gamma}_{Lps}^2 M\right)\right]^{-\frac{1}{2}}, \tag{3-33}$$

$$\tilde{d}_3 = \tilde{d}_7 = \left[2\tilde{q}_{sv}\left(-G^{\mathrm{fr}} + \mu(\hat{\rho}^E\hat{\mathcal{L}}\hat{\gamma}_{Tsv}G^{\mathrm{fr}}/\rho^f)^2\right)\right]^{-\frac{1}{2}}, \tag{3-34}$$

$$\tilde{d}_4 = \tilde{d}_8 = \left[2\tilde{q}_{tm}\left(-G^{\mathrm{fr}} + \mu(\hat{\rho}^E\hat{\mathcal{L}}\hat{\gamma}_{Ttm}G^{\mathrm{fr}}/\rho^f)^2\right)\right]^{-\frac{1}{2}}. \tag{3-35}$$

The submatrices of the flux-normalized composition matrix are

$$
\tilde{\mathbf{L}}_1 = \begin{pmatrix}
\tilde{d}_1\tilde{q}_{pf}c_{pf} & \tilde{d}_2\tilde{q}_{ps}c_{ps} & -\tilde{d}_3 p_1 c_{sv} & -\tilde{d}_4 p_1 c_{tm} \\
\tilde{d}_1\tilde{q}_{pf}c_{pf}\hat{\gamma}_{Lpf} & \tilde{d}_2\tilde{q}_{ps}c_{ps}\hat{\gamma}_{Lps} & -\tilde{d}_3 p_1 (G^{\mathrm{fr}} - c_{sv}^2\rho^b)/(\rho^f c_{sv}) & -\tilde{d}_4 p_1 (G^{\mathrm{fr}} - c_{tm}^2\rho^b)/(\rho^f c_{tm}) \\
-2\tilde{d}_1 G^{\mathrm{fr}} p_1 q_{pf} c_{pf} & -2\tilde{d}_2 G^{\mathrm{fr}} p_1 q_{ps} c_{ps} & -\tilde{d}_3 G^{\mathrm{fr}}(q_{sv}^2 - p_1^2)c_{sv} & -\tilde{d}_4 G^{\mathrm{fr}}(q_{tm}^2 - p_1^2)c_{tm} \\
0 & 0 & -\tilde{d}_3\hat{\rho}^E\hat{\mathcal{L}}\hat{\gamma}_{Tsv}G^{\mathrm{fr}}/(\rho^f c_{sv}) & -\tilde{d}_4\hat{\rho}^E\hat{\mathcal{L}}\hat{\gamma}_{Ttm}G^{\mathrm{fr}}/(\rho^f c_{tm})
\end{pmatrix}, \tag{3-36}
$$

$$
\tilde{\mathbf{L}}_2 = \begin{pmatrix}
\tilde{d}_1(H - 2G^{\mathrm{fr}}p_1^2c_{pf}^2 + \hat{\gamma}_{Lpf}C)/c_{pf} & \tilde{d}_2(H - 2G^{\mathrm{fr}}p_1^2c_{ps}^2 + \hat{\gamma}_{Lps}C)/c_{ps} & -2\tilde{d}_3 G^{\mathrm{fr}} p_1 \tilde{q_{sv}} c_{sv} & -2\tilde{d}_4 G^{\mathrm{fr}} p_1 \tilde{q_{tm}} c_{tm} \\
\tilde{d}_1(C + \hat{\gamma}_{Lpf}M)/c_{pf} & \tilde{d}_2(C + \hat{\gamma}_{Lps}M)/c_{ps} & 0 & 0 \\
\tilde{d}_1 p_1 c_{pf} & \tilde{d}_2 p_1 c_{ps} & \tilde{d}_3\tilde{q}_{sv}c_{sv} & \tilde{d}_4\tilde{q}_{tm}c_{tm} \\
-\tilde{d}_1\hat{\rho}^E\hat{\mathcal{L}}\hat{\gamma}_{Lpf}p_1c_{pf}/\hat{\varepsilon}_{\mathcal{L}} & -\tilde{d}_2\hat{\rho}^E\hat{\mathcal{L}}\hat{\gamma}_{Lps}p_1c_{ps}/\hat{\varepsilon}_{\mathcal{L}} & -\tilde{d}_3\mu\hat{\rho}^E\hat{\mathcal{L}}G^{\mathrm{fr}}\hat{\gamma}_{Tsv}\tilde{q}_{sv}c_{sv}/\rho^f & -\tilde{d}_4\mu\hat{\rho}^E\hat{\mathcal{L}}G^{\mathrm{fr}}\hat{\gamma}_{Ttm}\tilde{q}_{tm}c_{tm}/\rho^f
\end{pmatrix}. \tag{3-37}
$$

The flux-normalized decomposition operator, $\tilde{\mathbf{L}}^{-1}$, is found by inverting Equation (3-31) to obtain

$$
\tilde{\mathbf{L}}^{-1}(p_1) = \frac{1}{2}\begin{pmatrix} \tilde{\mathbf{L}}_1^{-1}(p_1) & \tilde{\mathbf{L}}_2^{-1}(p_1) \\ \tilde{\mathbf{L}}_1^{-1}(p_1) & -\tilde{\mathbf{L}}_2^{-1}(p_1) \end{pmatrix}. \tag{3-38}
$$

However, to avoid explicitly numerically calculating the inverses of the submatrices, one can see from Eq. (3-27) that if the composition matrix is a general function of the horizontal wavenumber, the flux-normalized decomposition matrix can be expressed as

$$
\tilde{\mathbf{L}}^{-1}(p_1) = \begin{pmatrix} \tilde{\mathbf{L}}_2^t(-p_1) & \tilde{\mathbf{L}}_1^t(-p_1) \\ \tilde{\mathbf{L}}_2^t(-p_1) & -\tilde{\mathbf{L}}_1^t(-p_1) \end{pmatrix}. \tag{3-39}
$$

By comparing the above equations for the decomposition matrix, we note that the desired inverse of one submatrix can be expressed in terms of the transpose of the other submatrix,

$$
\tilde{\mathbf{L}}_1^{-1}(p_1) = 2\tilde{\mathbf{L}}_2^t(-p_1) \text{ and } \tilde{\mathbf{L}}_2^{-1}(p_1) = 2\tilde{\mathbf{L}}_1^t(-p_1). \tag{3-40}
$$

3-6 One-way wave equation

Wapenaar and Berkhout (1989) extensively treated wavefield extrapolation and the relation between two-way and one-way wave equations. As seen in Section 3-3, the system matrix $\tilde{\mathbf{A}}$ of the two-way wave equation, Eq. (2-45), can be decomposed into matrices composed of its eigenvectors and eigenvalues,

$$
\tilde{\mathbf{A}} = \tilde{\mathbf{L}}\tilde{\mathbf{H}}\tilde{\mathbf{L}}^{-1}. \tag{3-41}
$$

Substituting Eq. (3-41) into the two-way wave equation and multiplying from the left by $\tilde{\mathbf{L}}^{-1}$ gives (Wapenaar et al., 2001)

$$\tilde{\mathbf{L}}^{-1}\frac{\partial\tilde{\mathbf{q}}}{\partial x_3} = \tilde{\mathbf{H}}\tilde{\mathbf{L}}^{-1}\tilde{\mathbf{q}} + \tilde{\mathbf{L}}^{-1}\tilde{\mathbf{d}}. \tag{3-42}$$

From this, it can be inferred that the one-way wave and source vectors can be obtained through the action of the decomposition operator on the respective two-way quantities,

$$\tilde{\mathbf{p}} = \tilde{\mathbf{L}}^{-1}\tilde{\mathbf{q}}, \tag{3-43}$$

$$\tilde{\mathbf{b}} = \tilde{\mathbf{L}}^{-1}\tilde{\mathbf{d}}. \tag{3-44}$$

Further defining the one-way operator matrix $\tilde{\mathbf{B}}$ as

$$\tilde{\mathbf{B}} = \tilde{\mathbf{H}} - \tilde{\mathbf{L}}^{-1}\frac{\partial}{\partial x_3}\tilde{\mathbf{L}}, \tag{3-45}$$

allows the one-way wave equation to be cast as

$$\frac{\partial\tilde{\mathbf{p}}}{\partial x_3} = \tilde{\mathbf{B}}\tilde{\mathbf{p}} + \tilde{\mathbf{b}}. \tag{3-46}$$

The solution of Eq. (3-46) was found by Wapenaar and Berkhout (1989), using the method of variation of parameters (Boyce and Di Prima, 1969), to be

$$\tilde{\mathbf{p}}(x_3) = \tilde{\mathbf{W}}(x_3, x_{3,0})\tilde{\mathbf{p}}(x_{3,0}) + \int_{x_{3,0}}^{x_3}\tilde{\mathbf{W}}(x_3, x_3')\tilde{\mathbf{b}}(x_3')dx_3', \tag{3-47}$$

where $\tilde{\mathbf{W}}$ is the one-way extrapolation operator. This general solution of the one-way wave equation presents the one-way wavefield at a given depth, x_3, as a function of the wavefield extrapolated from a reference depth, $x_{3,0}$, and of the contribution from all sources located between $x_{3,0}$ and x_3. The wavefield extrapolator is defined as follows:

$$\tilde{\mathbf{W}}(x_3, x_{3,0}) = \sum_{\mathrm{m}=0}^{\infty}\frac{(x_3 - x_{3,0})^{\mathrm{m}}}{\mathrm{m}!}\tilde{\mathbf{B}}_{\mathrm{m}}(x_{3,0}), \tag{3-48}$$

where $\tilde{\mathbf{B}}_{\mathrm{m}}(x_{3,0})$ is defined recursively as

$$\tilde{\mathbf{B}}_{\mathrm{m}+1}(x_{3,0}) = \left.\frac{\partial\tilde{\mathbf{B}}_{\mathrm{m}}(x_3)}{\partial x_3}\right|_{(x_{3,0})} + \tilde{\mathbf{B}}_{\mathrm{m}}(x_{3,0})\tilde{\mathbf{B}}_1(x_{3,0}) \tag{3-49}$$

and

$$\tilde{\mathbf{B}}_0(x_{3,0}) = \mathbf{I}. \tag{3-50}$$

Referring back to Equations (3-43) and (3-44) and multiplying both equations from the left by $\tilde{\mathbf{L}}$, it can be seen that the two-way wave and source vectors are created from the one-way wave and source vectors through the action of a composition operator,

$$\tilde{\mathbf{q}} = \tilde{\mathbf{L}}\tilde{\mathbf{p}} \text{ and } \tilde{\mathbf{d}} = \tilde{\mathbf{L}}\tilde{\mathbf{b}}. \tag{3-51}$$

The flux-normalized one-way wave and source vectors can be expressed as

$$\tilde{\mathbf{p}} = \begin{pmatrix} \tilde{\mathbf{p}}^+ \\ \tilde{\mathbf{p}}^- \end{pmatrix} \text{ and } \tilde{\mathbf{b}} = \begin{pmatrix} \tilde{\mathbf{b}}^+ \\ \tilde{\mathbf{b}}^- \end{pmatrix}, \tag{3-52}$$

where a positive superscript indicates a downgoing wavefield and a negative superscript an upgoing wavefield. Based on the arrangement of the flux-normalized composition order for the P-SV-TM system,

$$\tilde{\mathbf{L}} = (\tilde{\mathbf{a}}^+_{pf}, \tilde{\mathbf{a}}^+_{ps}, \tilde{\mathbf{a}}^+_{sv}, \tilde{\mathbf{a}}^+_{tm}, \tilde{\mathbf{a}}^-_{pf}, \tilde{\mathbf{a}}^-_{ps}, \tilde{\mathbf{a}}^-_{sv}, \tilde{\mathbf{a}}^-_{tm}), \tag{3-53}$$

the one-way vector quantities are organized as

$$\tilde{\mathbf{p}} = \begin{pmatrix} \tilde{p}^+_{pf} \\ \tilde{p}^+_{ps} \\ \tilde{p}^+_{sv} \\ \tilde{p}^+_{tm} \\ \tilde{p}^-_{pf} \\ \tilde{p}^-_{ps} \\ \tilde{p}^-_{sv} \\ \tilde{p}^-_{tm} \end{pmatrix} \text{ and } \tilde{\mathbf{b}} = \begin{pmatrix} \tilde{b}^+_{pf} \\ \tilde{b}^+_{ps} \\ \tilde{b}^+_{sv} \\ \tilde{b}^+_{tm} \\ \tilde{b}^-_{pf} \\ \tilde{b}^-_{ps} \\ \tilde{b}^-_{sv} \\ \tilde{b}^-_{tm} \end{pmatrix}. \tag{3-54}$$

Since the composition matrix specifies how the two-way field quantities are constructed from the above one-way wavefields, we can examine the structure of the composition matrix to ascertain which one-way wavefields contribute to a given two-way wavefield. To make this analysis more clear, the composition matrix is expressed symbolically as follows:

$$\tilde{\mathbf{L}} = \begin{pmatrix} \cdot & \cdot & \cdot & \cdot & \cdot & \cdot & \cdot & \cdot \\ \cdot & \cdot & \cdot & \cdot & \cdot & \cdot & \cdot & \cdot \\ \cdot & \cdot & \cdot & \cdot & \cdot & \cdot & \cdot & \cdot \\ 0 & 0 & \cdot & \cdot & 0 & 0 & \cdot & \cdot \\ \cdot & \cdot & \cdot & \cdot & \cdot & \cdot & \cdot & \cdot \\ \cdot & \cdot & 0 & 0 & \cdot & \cdot & 0 & 0 \\ \cdot & \cdot & \cdot & \cdot & \cdot & \cdot & \cdot & \cdot \\ \cdot & \cdot & \cdot & \cdot & \cdot & \cdot & \cdot & \cdot \end{pmatrix}, \tag{3-55}$$

with a $\cdot$ representing a non-zero entry. In composing two-way wavefields from a system containing all eight one-way wavefields, we see that measurements of any of $\tilde{v}^s_3$, $\tilde{w}_3$, $\tilde{\tau}^b_{13}$, $-\tilde{\tau}^b_{33}$, $\tilde{v}^s_1$ and $\tilde{E}_1$ contain information on all eight one-way wavefields. However, a measurement of the x_2 component of the magnetic field is not sensitive to either of the compressional wavefields, as a magnetic field is not carried along as part of the material response. In addition, a measurement of a change in the phase-averaged fluid pressure is clearly independent of the upgoing or downgoing SV- and TM-waves. This can be intuitively explained since these waves are polarized in the transverse direction, yet an ideal fluid cannot sustain shear stresses and thus will not undergo a change in pressure (Shaw, 2005).

3-6-1 Homogeneous source-free domain

In the case of a homogeneous source-free domain, Eq. (3-46) can be reduced to (Wapenaar and Berkhout, 1989)

$$\frac{\partial \tilde{\mathbf{p}}}{\partial x_3} = \tilde{\mathbf{H}}\tilde{\mathbf{p}}, \tag{3-56}$$

of which the general solution reads

$$\tilde{\mathbf{p}}(x_3) = \tilde{\mathbf{W}}(x_3, x_{3,0})\tilde{\mathbf{p}}(x_{3,0}). \tag{3-57}$$

The general expression for the extrapolation operator can be simplified by noting that in a homogeneous domain the derivative seen in Eq. (3-49) drops out, such that

$$\tilde{\mathbf{B}}_{\mathrm{m+1}} = \tilde{\mathbf{B}}_{\mathrm{m}}\tilde{\mathbf{B}}_1 \tag{3-58}$$

and where

$$\tilde{\mathbf{B}}_{\mathrm{m}} = \tilde{\mathbf{B}}_1^{\mathrm{m}} = \tilde{\mathbf{H}}^{\mathrm{m}}. \tag{3-59}$$

This allows $\tilde{\mathbf{W}}$ to be symbolically written as

$$\tilde{\mathbf{W}}(x_3, x_{3,0}) = \exp[\tilde{\mathbf{H}}(\Delta x_3)], \tag{3-60}$$

where

$$\Delta x_3 = x_3 - x_{3,0}. \tag{3-61}$$

To ensure that the wavefields physically decay during propagation with the extrapolation operator, we must appropriately choose $\tilde{\mathbf{H}}$ such that the real part of the exponential is negative. This is done by choosing the negative-valued root of $\frac{\omega^2}{\tilde{c}_w^2} - k_1^2$, as previously discussed.
The extrapolation operator $\tilde{\mathbf{W}}$ satisfies the property that

$$\tilde{\mathbf{W}}(x_{3,2}, x_{3,0}) = \tilde{\mathbf{W}}(x_{3,2}, x_{3,1})\tilde{\mathbf{W}}(x_{3,1}, x_{3,0}). \tag{3-62}$$

If we set $x_{3,2} = x_{3,0}$, the following relation is obtained,

$$[\tilde{\mathbf{W}}(x_{3,1}, x_{3,0})]^{-1} = \tilde{\mathbf{W}}(x_{3,0}, x_{3,1}). \tag{3-63}$$

Substituting the expression for the eigenvalue matrix $\tilde{\mathbf{H}}$ from Equation (3-16) into Equation (3-60) leads to

$$\tilde{\mathbf{W}}(x_3, x_{3,0}) = \begin{pmatrix} \tilde{\mathbf{W}}^+(x_3, x_{3,0}) & 0 \\ 0 & \tilde{\mathbf{W}}^-(x_3, x_{3,0}) \end{pmatrix}, \tag{3-64}$$

where both $\tilde{\mathrm{W}}^+(x_3, x_{3,0})$ and $\tilde{\mathrm{W}}^-(x_3, x_{3,0})$ are diagonal matrices. The downgoing and upgoing wavefield extrapolators can be explicitly written as

$$\tilde{\mathbf{W}}^+(\Delta x_3) = \begin{pmatrix} \exp[j\tilde{\mathcal{H}}_{pf}^+(\Delta x_3)] & 0 & 0 & 0 \\ 0 & \exp[j\tilde{\mathcal{H}}_{ps}^+(\Delta x_3)] & 0 & 0 \\ 0 & 0 & \exp[j\tilde{\mathcal{H}}_{sv}^+(\Delta x_3)] & 0 \\ 0 & 0 & 0 & \exp[j\tilde{\mathcal{H}}_{tm}^+(\Delta x_3)] \end{pmatrix} \tag{3-65}$$

and

$$\tilde{\mathbf{W}}^-(\Delta x_3) = \begin{pmatrix} \exp[j\tilde{\mathcal{H}}_{pf}^-(\Delta x_3)] & 0 & 0 & 0 \\ 0 & \exp[j\tilde{\mathcal{H}}_{ps}^-(\Delta x_3)] & 0 & 0 \\ 0 & 0 & \exp[j\tilde{\mathcal{H}}_{sv}^-(\Delta x_3)] & 0 \\ 0 & 0 & 0 & \exp[j\tilde{\mathcal{H}}_{tm}^-(\Delta x_3)] \end{pmatrix}, \tag{3-66}$$

from which it can be seen that the flux-normalized one-way propagators obey the following reciprocity relation (Wapenaar, 1998),

$$\tilde{\mathbf{W}}^+(x_{3,1}, x_{3,0}) = \tilde{\mathbf{W}}^-(x_{3,0}, x_{3,1}) \tag{3-67}$$

3-7 The P-SV-TM system in a vacuum

To simulate the effect of the Earth's surface on the propagating wavefields, the upper half-space of the modelled system is approximated by a vacuum. In a vacuum there are no pressure or shear waves, solely electromagnetic waves. Due to the resulting absence of seismoelectric coupling, the TM system can be decoupled from the P-SV system. We perform an eigendecomposition on the reduced TM system to determine its eigenvalues and eigenvectors. We first write out the reduced two-way wave equation,

$$\frac{\partial \tilde{\mathbf{q}}_{\mathrm{TM}}}{\partial x_3} = \tilde{\mathbf{A}}_{\mathrm{TM}} \tilde{\mathbf{q}}_{\mathrm{TM}} + \tilde{\mathbf{d}}_{\mathrm{TM}}, \tag{3-68}$$

where the two-way wave and source vectors are (note that the TM subscript will be left out in the remainder of this section for convenience),

$$\tilde{\mathbf{q}} = \begin{pmatrix} \tilde{H}_2 \\ \tilde{E}_1 \end{pmatrix} \text{ and } \tilde{\mathbf{d}} = \begin{pmatrix} -\tilde{J}_1^e \\ -\tilde{J}_2^m \end{pmatrix}. \tag{3-69}$$

The system matrix is now 2×2:

$$\tilde{\mathbf{A}} = \begin{pmatrix} 0 & -j\omega\epsilon_0 \\ -j\omega\mu_0 + \frac{jk_1^2}{\omega\epsilon_0} & 0 \end{pmatrix}, \tag{3-70}$$

where we have taken the dielectric permittivity in vacuum to be ϵ_0.
The expected velocity of the electromagnetic wave in a vacuum can be confirmed by finding the trivial solution of the zero eigenvalue problem, i.e. by solving $\left|\tilde{\mathbf{A}}\right| = 0$. We find

$$\omega^2 \epsilon_0 \mu_0 - k_1^2 = 0, \tag{3-71}$$

$$\epsilon_0 \mu_0 = \frac{k_1^2}{\omega^2} = \frac{1}{\hat{c}_0^2}, \tag{3-72}$$

which leads to the expected result of

$$\hat{c}_0^2 = \frac{1}{\epsilon_0 \mu_0}. \tag{3-73}$$

The non-zero eigenvalues of the TM system are found by solving the eigenvalue problem $\tilde{\mathbf{A}}\tilde{\mathbf{L}} = \tilde{\mathbf{L}}\tilde{\mathbf{H}}$. An equation for the eigenvalues is given by the characteristic equation, $\left|\tilde{\mathbf{A}} - \tilde{\mathbf{H}}\mathbf{I}\right| = \mathbf{0}$, and we seek the two distinct solutions:

$$\tilde{\mathbf{H}}^2 + \omega^2 \epsilon_0 \mu_0 - k_1^2 = 0 \tag{3-74}$$

$$-\tilde{\mathbf{H}}^2 = \frac{\omega^2}{c_0^2} - k_1^2 \tag{3-75}$$

It can be seen that there are two eigenvalues, $j\tilde{\mathcal{H}}$ and $-j\tilde{\mathcal{H}}$. We again make use of the relation $j\tilde{\mathcal{H}}^{\pm} = \mp j\tilde{\mathcal{H}}$, where

$$j\tilde{\mathcal{H}}^{\pm} = \mp j\sqrt{\frac{\omega^2}{\hat{c}_0^2} - k_1^2}. \tag{3-76}$$

To determine the eigenvectors we substitute the general eigenvalues ($j\tilde{\mathcal{H}}^{\pm}$) into the general eigenvector ($\tilde{\mathbf{a}}_n^{\pm}$) problem, $(\tilde{\mathbf{A}} - j\tilde{\mathcal{H}}^{\pm})\tilde{\mathbf{a}}_n^{\pm} = \mathbf{0}$, leading to

$$-j\tilde{\mathcal{H}}^{\pm}\tilde{\mathbf{a}}_1^{\pm} - j\omega\epsilon_0\tilde{\mathbf{a}}_2^{\pm} = 0, \tag{3-77}$$

$$\tilde{\mathbf{a}}_1^{\pm}\left(-j\omega\mu_0 + \frac{jk_1^2}{\omega\epsilon_0}\right) - j\tilde{\mathcal{H}}^{\pm}\tilde{\mathbf{a}}_2^{\pm} = 0. \tag{3-78}$$

We normalize to the magnetic field component by setting $\tilde{\mathbf{a}}_1^{\pm}$ to one and solving for $\tilde{\mathbf{a}}_2^{\pm}$,

$$-j\tilde{\mathcal{H}}^{\pm} - j\omega\epsilon_0\tilde{\mathbf{a}}_2^{\pm} = 0, \tag{3-79}$$

$$\tilde{\mathbf{a}}_2^{\pm} = -\frac{\tilde{\mathcal{H}}^{\pm}}{\omega\epsilon_0} = \pm\frac{\tilde{\mathcal{H}}}{\omega\epsilon_0}. \tag{3-80}$$

$$\tag{3-81}$$

Therefore the general eigenvector can be expressed as

$$\tilde{\mathbf{a}}^{\pm} = \begin{pmatrix} 1 \\ \pm\frac{\tilde{\mathcal{H}}}{\omega\epsilon_0} \end{pmatrix}. \tag{3-82}$$

Arranging these eigenvectors into the columns of the composition matrix with an order of $\begin{pmatrix}\tilde{\mathbf{a}}^{+} & \tilde{\mathbf{a}}^{-}\end{pmatrix}$ gives

$$\tilde{\mathbf{K}} = \begin{pmatrix} 1 & 1 \\ \frac{\tilde{\mathcal{H}}}{\omega\epsilon_0} & -\frac{\tilde{\mathcal{H}}}{\omega\epsilon_0} \end{pmatrix}. \tag{3-83}$$

This composition matrix can be flux-normalized, following the same scheme as previously outined. We find the value of the diagonal element to be

$$\tilde{d}_1 = \tilde{d}_2 = \left[2\frac{\tilde{\mathcal{H}}}{\omega\epsilon_0}\right]^{-\frac{1}{2}} = \left[2\frac{\tilde{q}}{\epsilon_0}\right]^{-\frac{1}{2}}. \tag{3-84}$$

Placing $\tilde{d}_1$ on the diagonal of $\tilde{\mathbf{D}}$ and multiplying it from the left with $\tilde{\mathbf{K}}$ allows us to construct the flux-normalized composition operator for the vacuum:

$$\tilde{\mathbf{L}} = \tilde{\mathbf{K}}\tilde{\mathbf{D}} = \begin{pmatrix} \tilde{d}_1 & \tilde{d}_1 \\ \tilde{d}_1\frac{\tilde{q}}{\epsilon_0} & -\tilde{d}_1\frac{\tilde{q}}{\epsilon_0} \end{pmatrix}. \tag{3-85}$$

The flux-normalized composition operator for the reduced system again has the specific structure defined by Equation (3-31), with $\tilde{\mathbf{L}}_1$ and $\tilde{\mathbf{L}}_2$ representing the appropriate elements.

Chapter 4

Reflection Formalism

This chapter provides the framework for carrying out seismoelectric simulations in a layered earth model. It follows the approach outlined by De Ridder (2007), which is based on a global reflection matrix formalism, originally derived for a three layer medium by Airy (1833). The scheme determines the total recorded wavefield at any depth from an arbitrarily located source, taking into account reflections from the bounding free surface and layers, including internal multiples. The waves that are not accounted for in applying this scheme are discussed in Section 4-2.

The model, seen in Figure 4-1, is oriented with the z axis positive downwards, bounded on the top by the pressure-free surface and on the bottom by a lower half-space. The domain of the vacuum above the pressure-free surface is denoted by $\mathbb{D}_0$, where the subscript denotes the layer number, which increases as one progresses downward through the layered model. Layer $\mathbb{D}_{n+1}$ is bounded above at depth z_n and below at depth z_{n+1}. The lower half-space is denoted $\mathbb{D}_{\mathrm{N}}$ and has an upper boundary of $z_{\text{N-1}}$.

4-1 Local Reflection Operators

A local reflection operator describes the generation of an outgoing plane wave from an incoming plane wave due to the reflection at an interface between contrasting media. The local downgoing reflection operator of a plane wave impinging on interface n, located at depth z_n, is defined according to

$$\tilde{\mathbf{p}}_n^-(z_n) = \tilde{\mathbf{r}}_n^+(z_n)\tilde{\mathbf{p}}_n^+(z_n), \tag{4-1}$$

where the interface is below $\mathbb{D}_n$ and above $\mathbb{D}_{n+1}$, as depicted in Figure 4-2.

Similarily, the local upgoing reflection operator of a plane wave impinging on interface $n-1$ located at depth z_{n-1} is

$$\tilde{\mathbf{p}}_n^+(z_{n-1}) = \tilde{\mathbf{r}}_n^-(z_{n-1})\tilde{\mathbf{p}}_n^-(z_{n-1}), \tag{4-2}$$

where the interface is below $\mathbb{D}_{n-1}$ and above $\mathbb{D}_n$, as depicted in Figure 4-3.

The local reflection operators simply define the reflections from a single layer. With multiple

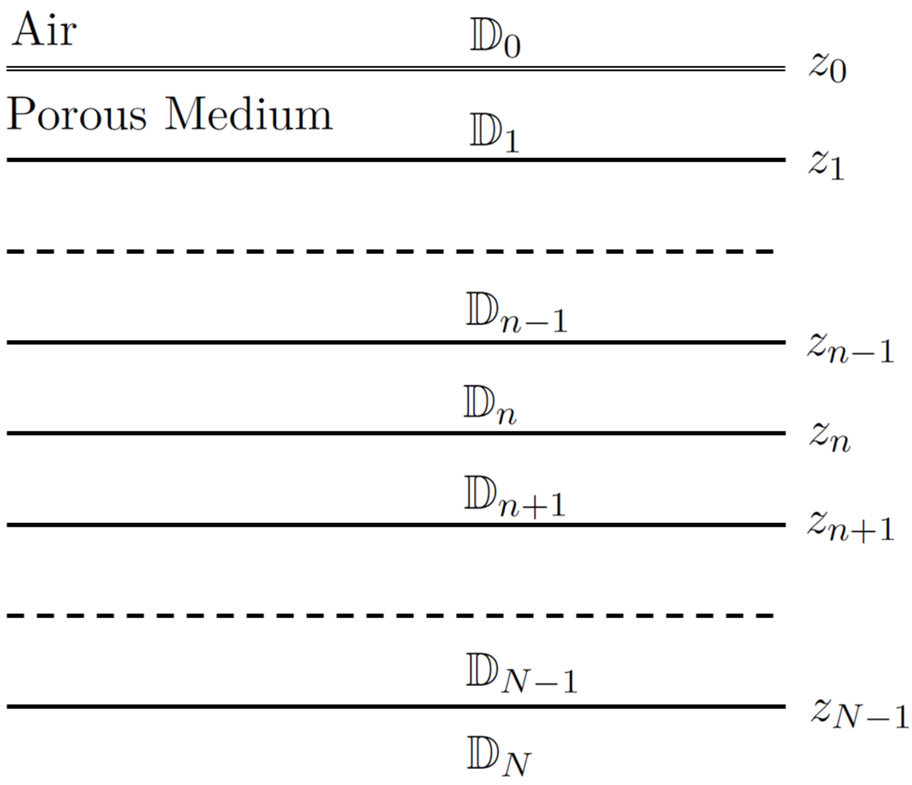

Figure 4-1: Illustration of layered model used. Subdomain n is denoted by n and has a lower boundary at depth z_n, where the z axis is positive downwards. Figure adapted from De Ridder (2007).

layers present we seek to define a reflection operator that accounts for both the immediate reflection from a single layer plus all reflections and multiples due to layers on the other side of it. To account for all reflections returning from either above or below a given interface, it is necessary to respectively define either an upgoing or downgoing global reflection operator.

4-2 Global Reflection Operators

The downgoing and upgoing global reflection operators are respectively defined as

$$\tilde{\mathbf{p}}_n^-(z_n) = \tilde{\mathbf{R}}_n^+(z_n)\tilde{\mathbf{p}}_n^+(z_n), \tag{4-3}$$

$$\tilde{\mathbf{p}}_n^+(z_{n-1}) = \tilde{\mathbf{R}}_n^-(z_{n-1})\tilde{\mathbf{p}}_n^-(z_{n-1}). \tag{4-4}$$

The downgoing and upgoing global reflection operators account for all internal multiples of the waves occurring in regions below or above, respectively, the reference depth level where they are defined. They do not account for the presence of a source in either the regions below or above the reference depth level. Secondary incoming waves are also excluded. This refers to waves that have been reflected back up or down through the reference depth level, where

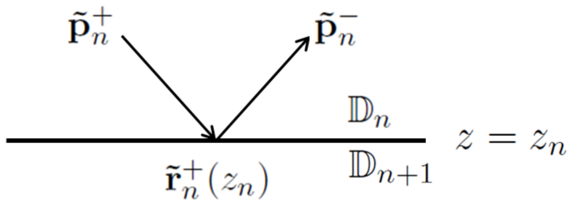

Figure 4-2: Illustration of upgoing wavefield generated by a local downgoing reflection operator.

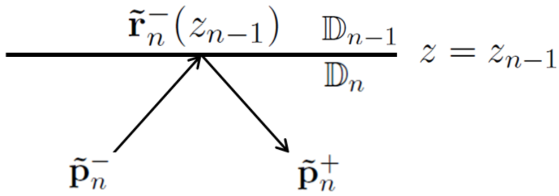

Figure 4-3: Illustration of downgoing wavefield generated by a local upgoing reflection operator.

the downgoing or upgoing global reflection operators, respectively, were defined, and that undergo another reflection on the other side of the reference depth level, such that they pass through the reference depth level for a third time.
The previously defined wavefield extrapolator operator propagates downgoing or upgoing wavefields, respectively, from depth z_n to z:

$$\tilde{\mathbf{p}}_n^+(z) = \tilde{\mathbf{W}}^+(z, z_n)\tilde{\mathbf{p}}_n^+(z_n), \tag{4-5}$$
$$\tilde{\mathbf{p}}_n^-(z) = \tilde{\mathbf{W}}^-(z, z_n)\tilde{\mathbf{p}}_n^-(z_n). \tag{4-6}$$

Substituting Equations (4-5) and (4-6) into Equation (4-3) leads to

$$\tilde{\mathbf{W}}^-(z_n, z)\tilde{\mathbf{p}}_n^-(z) = \tilde{\mathbf{R}}_n^+(z_n)\tilde{\mathbf{W}}^+(z_n, z)\tilde{\mathbf{p}}_n^+(z). \tag{4-7}$$

Rearranging and using the symmetry property of the flux-normalized one-way wavefield extrapolators, $\tilde{\mathbf{W}}^-(z, z_n) = \tilde{\mathbf{W}}^+(z_n, z)$ (Wapenaar, 1998), gives

$$\tilde{\mathbf{p}}_n^-(z) = \tilde{\mathbf{W}}^+(z_n, z)\tilde{\mathbf{R}}_n^+(z_n)\tilde{\mathbf{W}}^+(z_n, z)\tilde{\mathbf{p}}_n^+(z). \tag{4-8}$$

Upon rewriting the above equation and making use of Equation (4-3), a method of extrapolating the downgoing global reflection operator is found:

$$\tilde{\mathbf{R}}_n^+(z) = \tilde{\mathbf{W}}^+(z_n, z)\tilde{\mathbf{R}}_n^+(z_n)\tilde{\mathbf{W}}^+(z_n, z). \tag{4-9}$$

The same approach can be followed for the upgoing global reflection operator to obtain

$$\tilde{\mathbf{R}}_n^-(z) = \tilde{\mathbf{W}}^-(z_{n-1}, z)\tilde{\mathbf{R}}_n^-(z_{n-1})\tilde{\mathbf{W}}^-(z_{n-1}, z). \tag{4-10}$$

4-2-1 Explicit Representation

To have an expression for the global reflection operators in any layer, it is necessary to derive a recursive formula to propagate these operators from a known interface to the desired location. Domains outside the source layer will be considered first. The starting point for this derivation is treating the boundary conditions on the two-way wave vector $\tilde{\mathbf{q}}$ for a lossless source-free interface (Section 2-2),

$$\lim_{z \downarrow z_n} \tilde{\mathbf{q}}_{n+1}(z) - \lim_{z \uparrow z_n} \tilde{\mathbf{q}}_n(z) = \mathbf{0}, \tag{4-11}$$

by evaluating the limits as the interface is approached from below (layer $n+1$) and above (layer n):

$$\tilde{\mathbf{q}}_n(z_n) = \tilde{\mathbf{q}}_{n+1}(z_n). \tag{4-12}$$

Substituting in the relation $\tilde{\mathbf{q}}_n(z_n) = \tilde{\mathbf{L}}_n \tilde{\mathbf{p}}_n(z_n)$ leads to

$$\tilde{\mathbf{L}}_n \tilde{\mathbf{p}}_n(z_n) = \tilde{\mathbf{L}}_{n+1} \tilde{\mathbf{p}}_{n+1}(z_n). \tag{4-13}$$

It has previously been seen that the one-way wave vector, $\tilde{\mathbf{p}}$, and composition operator, $\tilde{\mathbf{L}}$, can be written as

$$\tilde{\mathbf{p}} = \begin{pmatrix} \tilde{\mathbf{p}}^+ \\ \tilde{\mathbf{p}}^- \end{pmatrix} \tag{4-14}$$

and

$$\tilde{\mathbf{L}} = \begin{pmatrix} \tilde{\mathbf{L}}_1 & \tilde{\mathbf{L}}_1 \\ \tilde{\mathbf{L}}_2 & -\tilde{\mathbf{L}}_2 \end{pmatrix}. \tag{4-15}$$

With this matrix representation, Equation (4-13) can be decomposed into

$$\tilde{\mathbf{L}}_{n,1} \tilde{\mathbf{p}}_n^+(z_n) + \tilde{\mathbf{L}}_{n,1} \tilde{\mathbf{p}}_n^-(z_n) = \tilde{\mathbf{L}}_{n+1,1} \tilde{\mathbf{p}}_{n+1}^+(z_n) + \tilde{\mathbf{L}}_{n+1,1} \tilde{\mathbf{p}}_{n+1}^-(z_n), \tag{4-16}$$

$$\tilde{\mathbf{L}}_{n,2} \tilde{\mathbf{p}}_n^+(z_n) - \tilde{\mathbf{L}}_{n,2} \tilde{\mathbf{p}}_n^-(z_n) = \tilde{\mathbf{L}}_{n+1,2} \tilde{\mathbf{p}}_{n+1}^+(z_n) - \tilde{\mathbf{L}}_{n+1,2} \tilde{\mathbf{p}}_{n+1}^-(z_n). \tag{4-17}$$

Substituting Equation (4-3) and

$$\tilde{\mathbf{p}}_{n+1}^-(z_n) = \tilde{\mathbf{R}}_{n+1}^+(z_n) \tilde{\mathbf{p}}_{n+1}^+(z_n) \tag{4-18}$$

into Equations (4-16) and (4-17) yields

$$\tilde{\mathbf{L}}_{n,1}[\mathbf{I} + \tilde{\mathbf{R}}_n^+(z_n)] \tilde{\mathbf{p}}_n^+(z_n) = \tilde{\mathbf{L}}_{n+1,1}[\mathbf{I} + \tilde{\mathbf{R}}_{n+1}^+(z_n)] \tilde{\mathbf{p}}_{n+1}^+(z_n), \tag{4-19}$$

$$\tilde{\mathbf{L}}_{n,2}[\mathbf{I} - \tilde{\mathbf{R}}_n^+(z_n)] \tilde{\mathbf{p}}_n^+(z_n) = \tilde{\mathbf{L}}_{n+1,2}[\mathbf{I} - \tilde{\mathbf{R}}_{n+1}^+(z_n)] \tilde{\mathbf{p}}_{n+1}^+(z_n). \tag{4-20}$$

It is now possible to derive an expression for $\tilde{\mathbf{R}}_n^+(z_n)$ in terms of $\tilde{\mathbf{R}}_{n+1}^+(z_n)$,

$$\tilde{\mathbf{R}}_n^+(z_n) = [(\underline{\tilde{\mathbf{L}}}_{n,1} - \underline{\tilde{\mathbf{L}}}_{n,2}) + (\underline{\tilde{\mathbf{L}}}_{n,1} + \underline{\tilde{\mathbf{L}}}_{n,2}) \tilde{\mathbf{R}}_{n+1}^+(z_n)][(\underline{\tilde{\mathbf{L}}}_{n,1} + \underline{\tilde{\mathbf{L}}}_{n,2}) + (\underline{\tilde{\mathbf{L}}}_{n,1} - \underline{\tilde{\mathbf{L}}}_{n,2}) \tilde{\mathbf{R}}_{n+1}^+(z_n)]^{-1}. \tag{4-21}$$

where $\underline{\tilde{\mathbf{L}}}_{n,1}$ and $\underline{\tilde{\mathbf{L}}}_{n,2}$ are defined by

$$\underline{\tilde{\mathbf{L}}}_{n,1} = [\tilde{\mathbf{L}}_{n,1}]^{-1} \tilde{\mathbf{L}}_{n+1,1} \text{ and } \underline{\tilde{\mathbf{L}}}_{n,2} = [\tilde{\mathbf{L}}_{n,2}]^{-1} \tilde{\mathbf{L}}_{n+1,2}\ . \tag{4-22}$$

Based on the properties of the flux-normalized system, we can rewrite the inverse of the composition operator $\tilde{\mathbf{L}}_{n,1}$ as a function of the transpose of the composition operator $\tilde{\mathbf{L}}_{n,2}$. This also applies to $\tilde{\mathbf{L}}_{n,2}$ and $\tilde{\mathbf{L}}_{n,1}$. By avoiding the use of an inverse, the numerical speed and accuracy of calculating $\underline{\tilde{\mathbf{L}}}_{n,1}$ and $\underline{\tilde{\mathbf{L}}}_{n,2}$ will be increased. These terms are thus rewritten as

$$\underline{\tilde{\mathbf{L}}}_{n,1} = [2\tilde{\mathbf{L}}^t_{n,2}]\tilde{\mathbf{L}}_{n+1,1} \text{ and } \underline{\tilde{\mathbf{L}}}_{n,2} = [2\tilde{\mathbf{L}}^t_{n,1}]\tilde{\mathbf{L}}_{n+1,2}. \tag{4-23}$$

The constant scaling factor in these expressions is present to equate them to their inverse equivalents. However, since the reflection matrices are based on fractions of these expressions (as seen in Eq. (4-21) and Eq. (4-24)), the scaling factors drop out.

Equation (4-21) makes it possible to determine the downgoing global reflection operator in any layer, by recursively propagating the operator up from the bottom interface. No reflections will be created from below the bottom interface, located at z_{N-1}, i.e. $\tilde{\mathbf{R}}^+_N(z > z_{N-1}) = \mathbf{0}$. Thus, at the bottom interface, Equation (4-21) can be expressed as a local reflection matrix

$$\tilde{\mathbf{R}}^+_{N-1}(z_n) = \tilde{\mathbf{r}}^+_n = (\underline{\tilde{\mathbf{L}}}_{n,1} - \underline{\tilde{\mathbf{L}}}_{n,2})(\underline{\tilde{\mathbf{L}}}_{n,1} + \underline{\tilde{\mathbf{L}}}_{n,2})^{-1}. \tag{4-24}$$

Substituting Equation (4-24) into Equation (4-21) allows the formula to be written with the local reflection matrix present,

$$\begin{aligned}\tilde{\mathbf{R}}^+_n(z_n) = [&\tilde{\mathbf{r}}^+_n(z_n) + (\underline{\tilde{\mathbf{L}}}_{n,1} + \underline{\tilde{\mathbf{L}}}_{n,2})\tilde{\mathbf{R}}^+_{n+1}(z_n)(\underline{\tilde{\mathbf{L}}}_{n,1} + \underline{\tilde{\mathbf{L}}}_{n,2})^{-1}]\\ &[\mathbf{I} + (\underline{\tilde{\mathbf{L}}}_{n,1} - \underline{\tilde{\mathbf{L}}}_{n,2})\tilde{\mathbf{R}}^+_{n+1}(z_n)(\underline{\tilde{\mathbf{L}}}_{n,1} + \underline{\tilde{\mathbf{L}}}_{n,2})^{-1}]^{-1}.\end{aligned} \tag{4-25}$$

This can be expressed in the same form as the scalar formula for the global reflection coefficient, as derived by Fokkema and Ziolkowski (1987),

$$\tilde{\mathbf{R}}^+_n(z_n) = (\underline{\tilde{\mathbf{L}}}_{n,1} + \underline{\tilde{\mathbf{L}}}_{n,2})[\tilde{\mathbf{r}}^+_n(z_n) + \tilde{\mathbf{R}}^+_{n+1}(z_n)][\mathbf{I} + \tilde{\mathbf{r}}^+_n(z_n)\tilde{\mathbf{R}}^+_{n+1}(z_n)]^{-1}(\underline{\tilde{\mathbf{L}}}_{n,1} + \underline{\tilde{\mathbf{L}}}_{n,2})^{-1}. \tag{4-26}$$

By switching the geometry and first calculating the local upgoing reflection matrix at the porous-vacuum interface, the upgoing global reflection matrix at any depth can be calculated in an analogous manner.

4-3 Source subdomain

The source is taken to be within a homogeneous layer n, which has an upper boundary at z_{n-1} and a lower boundary at z_n. The level of the source, z_s, does not coincide with an interface. Wavefields above the source level are denoted with the superscript a; those below the source level, with superscript b. Figure 4-4 depicts the partitioning of the source-level domain into its subdomains, a and b, as well as the wavefields present in each domain. The boundary conditions at the source level are again the starting point for the analysis. In this situation, the presence of the source creates a discontinuity in the field vector. The discontinuity is defined by the source vector $\tilde{\mathbf{d}}$, leading to the following boundary condition,

$$\lim_{z\downarrow z_s} \tilde{\mathbf{q}}^b_n(z) - \lim_{z\uparrow z_s} \tilde{\mathbf{q}}^a_n(z) = \tilde{\mathbf{d}}(z_s). \tag{4-27}$$

Evaluating the limits gives

$$\tilde{\mathbf{q}}^b_n(z_s) - \tilde{\mathbf{q}}^a_n(z_s) = \tilde{\mathbf{d}}(z_s). \tag{4-28}$$

Substituting in $\tilde{\mathbf{q}}_n(z_s) = \tilde{\mathbf{L}}_n\tilde{\mathbf{p}}_n(z_s)$ and $\tilde{\mathbf{d}}(z_s) = \tilde{\mathbf{L}}_n\tilde{\mathbf{b}}(z_s)$ leads to

$$\tilde{\mathbf{L}}_n\tilde{\mathbf{p}}^b_n(z_s) - \tilde{\mathbf{L}}_n\tilde{\mathbf{p}}^a_n(z_s) = \tilde{\mathbf{L}}_n\tilde{\mathbf{b}}(z_s). \tag{4-29}$$

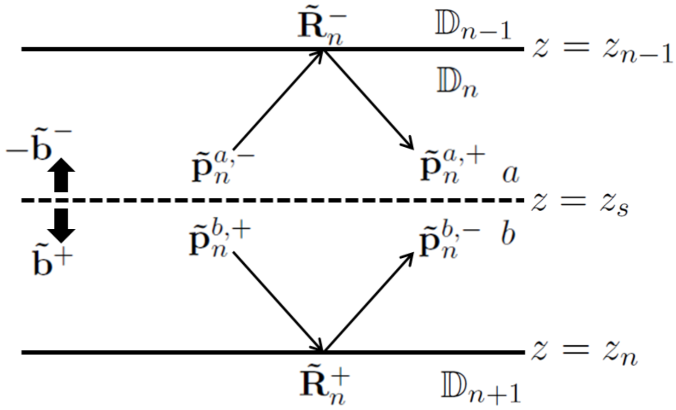

Figure 4-4: Source subdomain. z_s denotes the source level, a and b refer to the partitioning of domain n into the subdomains above the source level and below the source level, respectively.

Multiplying from the left by $[\tilde{\mathbf{L}}_n]^{-1}$ and decomposing $\tilde{\mathbf{p}}$ and $\tilde{\mathbf{b}}$ into their downgoing and upgoing components creates expressions for the one-way wavefield quantities in relation to the source terms,

$$\tilde{\mathbf{p}}_n^{b,+}(z_s) = \tilde{\mathbf{p}}_n^{a,+}(z_s) + \tilde{\mathbf{b}}^+(z_s), \tag{4-30}$$
$$\tilde{\mathbf{p}}_n^{b,-}(z_s) = \tilde{\mathbf{p}}_n^{a,-}(z_s) + \tilde{\mathbf{b}}^-(z_s). \tag{4-31}$$

Combining these equations with the definitions for the upgoing and downgoing global reflection operators at the level of the source,

$$\tilde{\mathbf{p}}_n^{b,-}(z_s) = \tilde{\mathbf{R}}_n^+(z_s)\tilde{\mathbf{p}}_n^{b,+}(z_s), \tag{4-32}$$
$$\tilde{\mathbf{p}}_n^{a,+}(z_s) = \tilde{\mathbf{R}}_n^-(z_s)\tilde{\mathbf{p}}_n^{a,-}(z_s), \tag{4-33}$$

makes it possible to obtain explicit symbolic representations for $\tilde{\mathbf{p}}_n^{a,-}, \tilde{\mathbf{p}}_n^{a,+}, \tilde{\mathbf{p}}_n^{b,-}$ and $\tilde{\mathbf{p}}_n^{b,+}$ as a function of the source-level global reflection operators,

$$\tilde{\mathbf{p}}_n^{a,-}(z_s) = [\mathbf{I} - \tilde{\mathbf{R}}_n^+(z_s)\tilde{\mathbf{R}}_n^-(z_s)]^{-1}[\tilde{\mathbf{R}}_n^+(z_s)\tilde{\mathbf{b}}_n^+(z_s) - \tilde{\mathbf{b}}_n^-(z_s)], \tag{4-34}$$
$$\tilde{\mathbf{p}}_n^{a,+}(z_s) = [\mathbf{I} - \tilde{\mathbf{R}}_n^-(z_s)\tilde{\mathbf{R}}_n^+(z_s)]^{-1}[\tilde{\mathbf{R}}_n^-(z_s)\tilde{\mathbf{R}}_n^+(z_s)\tilde{\mathbf{b}}_n^+(z_s) - \tilde{\mathbf{R}}_n^-(z_s)\tilde{\mathbf{b}}_n^-(z_s)], \tag{4-35}$$
$$\tilde{\mathbf{p}}_n^{b,-}(z_s) = [\mathbf{I} - \tilde{\mathbf{R}}_n^+(z_s)\tilde{\mathbf{R}}_n^-(z_s)]^{-1}[\tilde{\mathbf{R}}_n^+(z_s)\tilde{\mathbf{b}}_n^+(z_s) - \tilde{\mathbf{R}}_n^+(z_s)\tilde{\mathbf{R}}_n^-(z_s)\tilde{\mathbf{b}}_n^-(z_s)], \tag{4-36}$$
$$\tilde{\mathbf{p}}_n^{b,+}(z_s) = [\mathbf{I} - \tilde{\mathbf{R}}_n^-(z_s)\tilde{\mathbf{R}}_n^+(z_s)]^{-1}[\tilde{\mathbf{b}}_n^+(z_s) - \tilde{\mathbf{R}}_n^-(z_s)\tilde{\mathbf{b}}_n^-(z_s)]. \tag{4-37}$$

4-4 The wavefield in source-free layers

In Section 4-2-1, the reflection of wavefields from an interface was addressed; it is also necessary to consider the transmission of wavefields across interfaces. Here the propagation of a known wavefield from layer n through interface z_n to layer $n+1$ will be considered. $\tilde{\mathbf{p}}_{n+1}^+(z_n)$ is isolated from Equation (4-16) to find

$$\tilde{\mathbf{p}}_{n+1}^+(z_n) = [\mathbf{I} + \tilde{\mathbf{R}}_{n+1}^+(z_n)]^{-1}[\underline{\tilde{\mathbf{L}}}_{n,1}]^{-1}[\mathbf{I} + \tilde{\mathbf{R}}_n^+(z_n)]\tilde{\mathbf{p}}_n^+(z_n). \tag{4-38}$$

The upgoing wavefield in the next layer can subsequently be determined by reflecting the propagated downgoing wavefield through the use of Eq. (4-18).

4-5 Local reflection matrix at Earth's surface

We simulate the surface of the Earth as a vacuum-porous interface. The only wave types present in vacuum are the electromagnetic waves, $\tilde{p}^+_{0,tm}$ and $\tilde{p}^-_{0,tm}$; seismic waves are not present. The underlying porous medium can contain all eight one-way wavefields: $\tilde{p}^+_{1,pf}$, $\tilde{p}^+_{1,ps}$, $\tilde{p}^+_{1,sv}$, $\tilde{p}^+_{1,tm}$, $\tilde{p}^-_{1,pf}$, $\tilde{p}^-_{1,ps}$, $\tilde{p}^-_{1,sv}$ and $\tilde{p}^-_{1,tm}$.
A scattering matrix can be used to relate the outgoing wavefield to the ingoing wavefield in terms of the reflection and transmission coefficients of the interface,

$$\tilde{\mathbf{p}}^{\text{out}} = \tilde{\mathbf{S}}\tilde{\mathbf{p}}^{\text{in}}. \tag{4-39}$$

For the P-SV-TM system, the scattering matrix $\tilde{\mathbf{S}}$ is

$$\begin{pmatrix} \tilde{\mathbf{p}}_0^- \\ \tilde{\mathbf{p}}_1^+ \end{pmatrix} = \begin{pmatrix} \tilde{\mathbf{r}}^+ & \tilde{\mathbf{t}}^- \\ \tilde{\mathbf{t}}^+ & \tilde{\mathbf{r}}^- \end{pmatrix} \begin{pmatrix} \tilde{\mathbf{p}}_0^+ \\ \tilde{\mathbf{p}}_1^- \end{pmatrix}, \tag{4-40}$$

which can be written more explicitly as a 5×5 matrix:

$$\begin{pmatrix} \tilde{p}^-_{0,tm}(z_0) \\ \tilde{p}^+_{1,pf}(z_0) \\ \tilde{p}^+_{1,ps}(z_0) \\ \tilde{p}^+_{1,sv}(z_0) \\ \tilde{p}^+_{1,tm}(z_0) \end{pmatrix} =$$

$$\begin{pmatrix} \tilde{r}^+_{0,tm-tm}(z_0) & \tilde{t}^-_{tm-pf}(z_0) & \tilde{t}^-_{tm-ps}(z_0) & \tilde{t}^-_{tm-sv}(z_0) & \tilde{t}^-_{tm-tm}(z_0) \\ \tilde{t}^+_{pf-tm}(z_0) & \tilde{r}^-_{1,pf-pf}(z_0) & \tilde{r}^-_{1,pf-ps}(z_0) & \tilde{r}^-_{1,pf-sv}(z_0) & \tilde{r}^-_{1,pf-tm}(z_0) \\ \tilde{t}^+_{ps-tm}(z_0) & \tilde{r}^-_{1,ps-pf}(z_0) & \tilde{r}^-_{1,ps-ps}(z_0) & \tilde{r}^-_{1,ps-sv}(z_0) & \tilde{r}^-_{1,ps-tm}(z_0) \\ \tilde{t}^+_{sv-tm}(z_0) & \tilde{r}^-_{1,sv-pf}(z_0) & \tilde{r}^-_{1,sv-ps}(z_0) & \tilde{r}^-_{1,sv-sv}(z_0) & \tilde{r}^-_{1,sv-tm}(z_0) \\ \tilde{t}^+_{tm-tm}(z_0) & \tilde{r}^-_{1,tm-pf}(z_0) & \tilde{r}^-_{1,tm-ps}(z_0) & \tilde{r}^-_{1,tm-sv}(z_0) & \tilde{r}^-_{1,tm-tm}(z_0) \end{pmatrix} \begin{pmatrix} \tilde{p}^+_{0,tm}(z_0) \\ \tilde{p}^-_{1,pf}(z_0) \\ \tilde{p}^-_{1,ps}(z_0) \\ \tilde{p}^-_{1,sv}(z_0) \\ \tilde{p}^-_{1,tm}(z_0) \end{pmatrix}, \tag{4-41}$$

where the first subscript of the scattering matrix denotes the outgoing wavetype and the second subscript denotes the ingoing wavetype, e.g. $\tilde{r}^-_{1,pf-tm}(z_0)$ is the free surface reflection coefficient for an upgoing TM-wave converting to a downgoing fast P-wave.
The boundary conditions on the field vector, $\tilde{\mathbf{q}}_{\text{V}} = (\tilde{v}^s_3, \tilde{\omega}_3, \tilde{\tau}^b_{13}, \tilde{H}_2, -\tilde{\tau}^b_{33}, \tilde{p}, \tilde{v}^s_1, \tilde{E}_1)$, are used to determine the local reflection coefficients. At a vacuum-porous interface the continuity of the two-way wave vector components (Section 2-2) are

$$\begin{pmatrix} 0 \\ \tilde{H}_2 \\ 0 \\ 0 \\ \tilde{E}_1 \end{pmatrix}_0 = \begin{pmatrix} \tilde{\tau}^b_{13} \\ \tilde{H}_2 \\ -\tilde{\tau}^b_{33} \\ \tilde{p} \\ \tilde{E}_1 \end{pmatrix}_1, \tag{4-42}$$

which can be expressed in terms of the action of their respective eigenvectors on the one-way wave quantities,

$$\tilde{\mathbf{L}}_0\tilde{\mathbf{p}}_0(z_0) = \tilde{\mathbf{L}}_1\tilde{\mathbf{p}}_1(z_0). \tag{4-43}$$

The eigenvectors of the seismoelectric P-SV-TM system in both vacuum and porous media have previously been determined and the above equation can be explicitly expressed in terms of these eigenvectors and the one-way wave fields that can be present on each side of the interface,

$$\begin{pmatrix} 0 & 0 \\ \tilde{a}^+_{0,tm,1} & \tilde{a}^-_{0,tm,1} \\ 0 & 0 \\ 0 & 0 \\ \tilde{a}^+_{0,tm,2} & \tilde{a}^-_{0,tm,2} \end{pmatrix} \begin{pmatrix} \tilde{p}^+_{0,tm}(z_0) \\ \tilde{p}^-_{0,tm}(z_0) \end{pmatrix} =$$

$$\begin{pmatrix} \tilde{a}^+_{1,pf,3} & \tilde{a}^+_{1,ps,3} & \tilde{a}^+_{1,sv,3} & \tilde{a}^+_{1,tm,3} & \tilde{a}^-_{1,pf,3} & \tilde{a}^-_{1,ps,3} & \tilde{a}^-_{1,sv,3} & \tilde{a}^-_{1,tm,3} \\ \tilde{a}^+_{1,pf,4} & \tilde{a}^+_{1,ps,4} & \tilde{a}^+_{1,sv,4} & \tilde{a}^+_{1,tm,4} & \tilde{a}^-_{1,pf,4} & \tilde{a}^-_{1,ps,4} & \tilde{a}^-_{1,sv,4} & \tilde{a}^-_{1,tm,4} \\ \tilde{a}^+_{1,pf,5} & \tilde{a}^+_{1,ps,5} & \tilde{a}^+_{1,sv,5} & \tilde{a}^+_{1,tm,5} & \tilde{a}^-_{1,pf,5} & \tilde{a}^-_{1,ps,5} & \tilde{a}^-_{1,sv,5} & \tilde{a}^-_{1,tm,5} \\ \tilde{a}^+_{1,pf,6} & \tilde{a}^+_{1,ps,6} & \tilde{a}^+_{1,sv,6} & \tilde{a}^+_{1,tm,6} & \tilde{a}^-_{1,pf,6} & \tilde{a}^-_{1,ps,6} & \tilde{a}^-_{1,sv,6} & \tilde{a}^-_{1,tm,6} \\ \tilde{a}^+_{1,pf,8} & \tilde{a}^+_{1,ps,8} & \tilde{a}^+_{1,sv,8} & \tilde{a}^+_{1,tm,8} & \tilde{a}^-_{1,pf,8} & \tilde{a}^-_{1,ps,8} & \tilde{a}^-_{1,sv,8} & \tilde{a}^-_{1,tm,8} \end{pmatrix} \begin{pmatrix} \tilde{p}^+_{1,pf}(z_0) \\ \tilde{p}^+_{1,ps}(z_0) \\ \tilde{p}^+_{1,sv}(z_0) \\ \tilde{p}^+_{1,tm}(z_0) \\ \tilde{p}^-_{1,pf}(z_0) \\ \tilde{p}^-_{1,ps}(z_0) \\ \tilde{p}^-_{1,sv}(z_0) \\ \tilde{p}^-_{1,tm}(z_0) \end{pmatrix}, \tag{4-44}$$

where $\tilde{a}^\pm_{0,tm,i}$ refers to the eigenvectors of the seismoelectric system in vacuum and $\tilde{a}^\pm_{0,w,i}$ to the eigenvectors of the system in a homogeneous source-free subdomain, i.e. $\tilde{a}^+_{0,tm,2} = \tilde{d}_1\frac{\tilde{q}}{\epsilon_0}$. We can also express Equation (4-44) in the following form (Shaw, 2005),

$$\tilde{\mathbf{a}}^+_0\tilde{\mathbf{p}}^+_0 + \tilde{\mathbf{a}}^-_0\tilde{\mathbf{p}}^-_0 = \tilde{\mathbf{a}}^+_1\tilde{\mathbf{p}}^+_1 + \tilde{\mathbf{a}}^-_1\tilde{\mathbf{p}}^-_1. \tag{4-45}$$

To write the eigenvectors in terms of the reflection and transmission coefficients we seek to state Equation (4-44) in the form of Equation (4-41) by first reorganizing Equation (4-45) as

$$-\tilde{\mathbf{a}}^-_0\tilde{\mathbf{p}}^-_0 + \tilde{\mathbf{a}}^+_1\tilde{\mathbf{p}}^+_1 = \tilde{\mathbf{a}}^+_0\tilde{\mathbf{p}}^+_0 - \tilde{\mathbf{a}}^-_1\tilde{\mathbf{p}}^-_1. \tag{4-46}$$

It is then clear that Equation (4-44) takes on the following structure:

$$\begin{pmatrix} 0 & \tilde{a}^+_{1,pf,3} & \tilde{a}^+_{1,ps,3} & \tilde{a}^+_{1,sv,3} & \tilde{a}^+_{1,tm,3} \\ -\tilde{a}^-_{0,tm,1} & \tilde{a}^+_{1,pf,4} & \tilde{a}^+_{1,ps,4} & \tilde{a}^+_{1,sv,4} & \tilde{a}^+_{1,tm,4} \\ 0 & \tilde{a}^+_{1,pf,5} & \tilde{a}^+_{1,ps,5} & \tilde{a}^+_{1,sv,5} & \tilde{a}^+_{1,tm,5} \\ 0 & \tilde{a}^+_{1,pf,6} & \tilde{a}^+_{1,ps,6} & \tilde{a}^+_{1,sv,6} & \tilde{a}^+_{1,tm,6} \\ -\tilde{a}^-_{0,tm,2} & \tilde{a}^+_{1,pf,8} & \tilde{a}^+_{1,ps,8} & \tilde{a}^+_{1,sv,8} & \tilde{a}^+_{1,tm,8} \end{pmatrix} \begin{pmatrix} \tilde{p}^-_{0,tm}(z_0) \\ \tilde{p}^+_{1,pf}(z_0) \\ \tilde{p}^+_{1,ps}(z_0) \\ \tilde{p}^+_{1,sv}(z_0) \\ \tilde{p}^+_{1,tm}(z_0) \end{pmatrix} =$$

$$\begin{pmatrix} 0 & -\tilde{a}^-_{1,pf,3} & -\tilde{a}^-_{1,ps,3} & -\tilde{a}^-_{1,sv,3} & -\tilde{a}^-_{1,tm,3} \\ \tilde{a}^+_{0,tm,1} & -\tilde{a}^-_{1,pf,4} & -\tilde{a}^-_{1,ps,4} & -\tilde{a}^-_{1,sv,4} & -\tilde{a}^-_{1,tm,4} \\ 0 & -\tilde{a}^-_{1,pf,5} & -\tilde{a}^-_{1,ps,5} & -\tilde{a}^-_{1,sv,5} & -\tilde{a}^-_{1,tm,5} \\ 0 & -\tilde{a}^-_{1,pf,6} & -\tilde{a}^-_{1,ps,6} & -\tilde{a}^-_{1,sv,6} & -\tilde{a}^-_{1,tm,6} \\ \tilde{a}^+_{0,tm,2} & -\tilde{a}^-_{1,pf,8} & -\tilde{a}^-_{1,ps,8} & -\tilde{a}^-_{1,sv,8} & -\tilde{a}^-_{1,tm,8} \end{pmatrix} \begin{pmatrix} \tilde{p}^+_{0,tm}(z_0) \\ \tilde{p}^-_{1,pf}(z_0) \\ \tilde{p}^-_{1,ps}(z_0) \\ \tilde{p}^-_{1,sv}(z_0) \\ \tilde{p}^-_{1,tm}(z_0) \end{pmatrix}. \tag{4-47}$$

Left-multiplying this equation by the inverse of the left-most matrix and comparing to Equation (4-41), leads to the desired relation between the eigenvectors and the reflection coefficients,

$$\begin{pmatrix} \tilde{r}^{+}_{0,tm-tm}(z_0) & \tilde{t}^{-}_{tm-pf}(z_0) & \tilde{t}^{-}_{tm-ps}(z_0) & \tilde{t}^{-}_{tm-sv}(z_0) & \tilde{t}^{-}_{tm-tm}(z_0) \\ \tilde{t}^{+}_{pf-tm}(z_0) & \tilde{r}^{-}_{1,pf-pf}(z_0) & \tilde{r}^{-}_{1,pf-ps}(z_0) & \tilde{r}^{-}_{1,pf-sv}(z_0) & \tilde{r}^{-}_{1,pf-tm}(z_0) \\ \tilde{t}^{+}_{ps-tm}(z_0) & \tilde{r}^{-}_{1,ps-pf}(z_0) & \tilde{r}^{-}_{1,ps-ps}(z_0) & \tilde{r}^{-}_{1,ps-sv}(z_0) & \tilde{r}^{-}_{1,ps-tm}(z_0) \\ \tilde{t}^{+}_{sv-tm}(z_0) & \tilde{r}^{-}_{1,sv-pf}(z_0) & \tilde{r}^{-}_{1,sv-ps}(z_0) & \tilde{r}^{-}_{1,sv-sv}(z_0) & \tilde{r}^{-}_{1,sv-tm}(z_0) \\ \tilde{t}^{+}_{tm-tm}(z_0) & \tilde{r}^{-}_{1,tm-pf}(z_0) & \tilde{r}^{-}_{1,tm-ps}(z_0) & \tilde{r}^{-}_{1,tm-sv}(z_0) & \tilde{r}^{-}_{1,tm-tm}(z_0) \end{pmatrix} =$$

$$\begin{pmatrix} 0 & \tilde{a}^{+}_{1,pf,3} & \tilde{a}^{+}_{1,ps,3} & \tilde{a}^{+}_{1,sv,3} & \tilde{a}^{+}_{1,tm,3} \\ -\tilde{a}^{-}_{0,tm,1} & \tilde{a}^{+}_{1,pf,4} & \tilde{a}^{+}_{1,ps,4} & \tilde{a}^{+}_{1,sv,4} & \tilde{a}^{+}_{1,tm,4} \\ 0 & \tilde{a}^{+}_{1,pf,5} & \tilde{a}^{+}_{1,ps,5} & \tilde{a}^{+}_{1,sv,5} & \tilde{a}^{+}_{1,tm,5} \\ 0 & \tilde{a}^{+}_{1,pf,6} & \tilde{a}^{+}_{1,ps,6} & \tilde{a}^{+}_{1,sv,6} & \tilde{a}^{+}_{1,tm,6} \\ -\tilde{a}^{-}_{0,tm,2} & \tilde{a}^{+}_{1,pf,8} & \tilde{a}^{+}_{1,ps,8} & \tilde{a}^{+}_{1,sv,8} & \tilde{a}^{+}_{1,tm,8} \end{pmatrix}^{-1}$$

$$\begin{pmatrix} 0 & -\tilde{a}^{-}_{1,pf,3} & -\tilde{a}^{-}_{1,ps,3} & -\tilde{a}^{-}_{1,sv,3} & -\tilde{a}^{-}_{1,tm,3} \\ \tilde{a}^{+}_{0,tm,1} & -\tilde{a}^{-}_{1,pf,4} & -\tilde{a}^{-}_{1,ps,4} & -\tilde{a}^{-}_{1,sv,4} & -\tilde{a}^{-}_{1,tm,4} \\ 0 & -\tilde{a}^{-}_{1,pf,5} & -\tilde{a}^{-}_{1,ps,5} & -\tilde{a}^{-}_{1,sv,5} & -\tilde{a}^{-}_{1,tm,5} \\ 0 & -\tilde{a}^{-}_{1,pf,6} & -\tilde{a}^{-}_{1,ps,6} & -\tilde{a}^{-}_{1,sv,6} & -\tilde{a}^{-}_{1,tm,6} \\ \tilde{a}^{+}_{0,tm,2} & -\tilde{a}^{-}_{1,pf,8} & -\tilde{a}^{-}_{1,ps,8} & -\tilde{a}^{-}_{1,sv,8} & -\tilde{a}^{-}_{1,tm,8} \end{pmatrix}. \quad (4\text{-}48)$$

4-5-1 Reflection coefficients at normal incidence

We can now examine the general upgoing 2-D reflection matrix at the free surface, given above by the $\tilde{r}^-$ components of Equation (4-48), for the situation of normal incidence. At normal incidence, the horizontal slowness p_1 is equal to zero, reducing the problem to a 1-D case. Substituting the eigenvectors for $p_1 = 0$ into Equation (4-48) and solving for the upgoing reflection coefficients shows that, at normal incidence, the compressional waves decouple from the SV-TM waves. The free surface is perfectly reflecting for both the fast and slow P-waves, whereas the reflection coefficients for the vertically polarized shear wave, the transverse magnetic wave, and their conversions are dependent on the medium parameters of the underlying layer. At normal incidence, seismoelectric coupling is solely present within the SV-TM system. However, as the horizontal slowness increases from zero (corresponding to an increase in the angle of incidence) the P- and SV-TM systems recouple and conversions from longitudinal waves to transverse waves, and vice versa, take place. In other words, seismoelectric coupling is no longer limited to the SV-TM system.

4-6 Applying the scheme

The use of global reflection matrices, as outlined by De Ridder (2007), accounts for all internal multiple reflections of the source wave. A benefit of using this scheme when modelling is that it avoids the need to recursively propagate the wavefield through the layered medium based on local reflection coefficients. The method is applied as follows: first, the upgoing and downgoing local reflection matrices at the top and bottom boundaries, respectively, of the model are determined from the free surface reflection matrix, Eq. (4-48), and the general equation for a local reflection matrix, Eq. (4-24). The global reflection matrices of the neighbouring layers are then found by downward or upward extrapolating the local reflection matrices from the boundary to the adjacent layer and then calculating the global reflection matrices at that depth through the use of Eq. (4-25), or its equivalent for the upgoing global reflection matrix. This sequence of extrapolation and recursively updating the global reflection matrix, using Eq. (4-21), is repeated until the upgoing and downgoing global reflection matrices are resolved both at the source and the receiver level. The next step is to determine the wavefield in the source layer, both downgoing immediately below the source and upgoing immediately above the source, using Equations (4-35) and (4-36). The source-level wavefield that is in the direction of the receiver is propagated through the separating layers, based on Eq. (4-38), until it reaches the receiver level. The incoming wavefield at the receiver level is then reflected once by the receiver-level global reflection matrix, leading to receiver-level expressions for the full upgoing and downgoing wavefields.

Chapter 5

Modelling

In this chapter, the reflection formalism of Chapter 4 will be combined with the matrix-vector components of the one-way wave equation, as presented in Chapter 3, to carry out numerical modelling of the P-SV-TM propagation mode. We start with a transmission experiment in a homogeneous model to depict one-way wavefields and their composition into two-way wavefields. In the succeeding section a second homogeneous layer is introduced into the background model, allowing a reflection experiment to be conducted. Due to the difference in the medium parameters of the two half-spaces, seismoelectric conversions occur at the interface, effectively acting as a secondary source for one-way wavefields. We then introduce a free surface at the top of the model, which simulates a more realistic two-layered Earth setting with the presence of multiple reflections and multiple seismoelectric conversions. Finally, we proceed to a series of models to simulate potential applications of the seismoelectric method: depth estimation of a subsurface layer from the amplitude of the interface response, Vertical ElectroSeismic Profiling (VESP) and aquifer monitoring.

5-1 Numerical implementation

The simulations were conducted on a grid size of 4096×256 $(x_1 \times t)$. The source function for both the one- and two-way wavefields is a zero-phase Ricker wavelet, the second derivative of a Gaussian function, with a centre frequency of 600 radians per second (approximately 95 Hertz). The source is implemented in the frequency domain and is described by (Shaw, 2005),

$$\hat{S}(\omega) = \frac{2}{\sqrt{\pi}}\frac{\omega^2}{\omega_0^3}\exp\left[-\frac{\omega^2}{\omega_0^2}\right], \tag{5-1}$$

where ω_0 is the centre frequency. The Nyquist sampling theorem requires that the spatial sampling is set to sample the wavefields a minimum of two times per wavelength, based on the velocity of the slowest wave,

$$\Delta x = \frac{\lambda}{2} = \frac{c_{min}}{2f_N}, \tag{5-2}$$

where f_N is the Nyquist frequency. Since the slowest wave is the slow P-wave, which is essentially a pure fluid-pressure diffusion, we should rewrite the above constraint as the requirement to sample two times within the wave's diffusive skin depth (Haines and Pride, 2006). However, the temporal and spatial scales required for proper modelling of the Biot slow wave would render the modelling computationally expensive (Wenzlau and Mueller, 2009). We choose to adopt larger scales, which signifies that the Biot slow wave would not be properly modelled around material-property contrasts (Pride and Garambois, 2002). For our modelling purposes we will take the vertically polarized shear wave as the slowest wavefield, with a medium parameter dependent velocity that will not be significantly less than 2000 m/s. With this wavespeed in mind, we choose a spatial sampling of 2 metres. This spatial sampling also corresponds to the receiver spacing defined at the receiver depth level.

Since the calculations are carried out in the horizontal wavenumber-frequency domain, we must choose a grid size and discretization that limits spatial and temporal aliasing. The spatial sampling defined above is proportional to the shortest wavelength and thus defines the high wavenumber limit of the modelling. The length of the spatial axis, in combination with the step size, determines the low wavenumber limit, which is proportional to the large electromagnetic wavelength. The chosen time sampling step of 1 ms corresponds to a maximum frequency retrieval of 500 Hz. Although a finer spatial and temporal discretization would have been preferable, it was not possible due to computational limitations. Combining the grid size with the chosen discretization creates a grid extending in time to 0.25 seconds, with a maximum offset of ± 4000 metres. However, for convenience, only the near-offsets (± 1000 m) will be displayed.

It can be seen in Chapter 3 that some components of the P-SV-TM system's eigenvectors have a singularity at $\omega = 0$. To account for these singularities, a small positive imaginary frequency is added to the real frequency vector, such that $\omega = \omega_R - j\omega_I$, where $\omega_I > 0$. This additional term shifts the calculations just off the real frequency axis. It also damps the magnitude of the late arrivals, occuring due to the periodicity of the discrete Fourier transformation. The effective attenuation can be removed from the final result by including a growing exponential with time, $\exp(\omega_I t)$, in the kernel of the inverse-Fourier transform. We follow the approach of Haartsen and Pride (1997) and choose the value of the small added imaginary part to be

$$\omega_I = \frac{\pi}{t_{max}}. \tag{5-3}$$

5-2 Numerical analysis

A symbolic implementation of the seismoelectric system and reflection formalism of the previous chapters would yield the "true" symbolic representation of a wavefield, subject to the assumptions and constraints of Chapters 2 and 4. In order to carry out numerical modelling, the symbolic expressions must be replaced with numbers, resulting in numerical approximations being made to the true values. These approximations can introduce round-off errors, due to the inability to represent all real numbers on computers with finite memory. For a given computation, round-off errors are dependent on the numerical program and numerical representation being used, as well as the computational hardware on which the computation is run. Each numerical program (e.g. MATLAB, Maple, Fortran) carries out computations in a different way. This applies to, among other factors, the order of operations in which the computation is done, the internal representation of the elements of the computation and

the individual algorithms for the different operations. The accuracy of the final result that is stored by the program is restricted by both the software's numerical representation and the computer's hardware. The most common representation, the floating-point representation, can be considered a numerical implementation of scientific notation. The number of significant digits that are retained is restricted by the length of the binary format being used. For example, a computer that supports 64-bit units of data can store integers up to a binary format length of 64-bits, creating a precision of 16 decimal digits (referred to as double precision.) Floating-point arithmetic provides the floating-point approximation to operations carried out on floating-point numbers. Depending on the software, the numbers calculated using floating-point arithmetic are either rounded-off repeatedly during the operations or only once at the end. Naturally, larger errors are introduced when the first approach is implemented, as is the case with MATLAB. Two alternative approaches to numerically carrying-out calculations are rational arithmetic and arbitrary-precision arithmetic. Rational arithmetic represents all numbers as a combination of numerators and denominators, producing a rational number as the exact result. With arbitrary-precision arithmetic, values are stored in a variable-length array of digits, such that the number of significant digits is independent of the width of the binary format. Both these approaches lead to increased accuracy at the expense of time and storage (Press et al., 2007).
A final factor that dictates the severity of the round-off errors that are introduced is the relative magnitude of the variables in the computation. Two operations that can amplify round-off errors are additive dominance and subtractive cancellation. Additive dominance refers to the loss of precision due to the addition of a large number to a small number. In the worst case, this entails the magnitude of the large number remaining the same, such that the added value of the small number is lost. Subtractive cancellation occurs when two similiarly-valued numbers are subtracted. This results in a shift of the less-precise (due to previous round-off errors) decimal bits to locations of greater numerical significance. Since the errors propagate, a large volume of calculations could lead to a substantial error in the final result (Gentle, 2009).
Modelling the seismoelectric system necessitates implementing the medium parameters of two fundamentally different systems: elastodynamic and electromagnetic. The eigenvectors of the seismoelectric system are composed of a combination of small (e.g. slow P-wave velocity) and large (e.g. TM-wave velocity) numbers. Therefore, operations on the composition matrices, such as determining a local reflection matrix, are subject to both additive dominance and subtractive cancelation. Since the reflection matrices are the building-blocks of the reflection formalism, any error that is introduced in their computation will be propagated and amplified through the modelling procedure. To test the errors introduced at this stage, we checked if the local reflection matrix,

$$\tilde{\mathbf{r}}_n^+ = [\underline{\tilde{\mathbf{L}}}_{n,1} - \underline{\tilde{\mathbf{L}}}_{n,2}][\underline{\tilde{\mathbf{L}}}_{n,1} + \underline{\tilde{\mathbf{L}}}_{n,2}]^{-1}, \tag{5-4}$$

at an arbitrary location inside a homogeneous medium returned the expected null result. This was done by computing $\underline{\tilde{\mathbf{L}}}_1$ using both the inverse and transpose operators, i.e.

$$\underline{\tilde{\mathbf{L}}}_1 = [\tilde{\mathbf{L}}_1]^{-1}\tilde{\mathbf{L}}_1 = [2\tilde{\mathbf{L}}_2^t]\tilde{\mathbf{L}}_1 = \mathbf{I}. \tag{5-5}$$

Figures 5-1a and 5-1b display the maximum errors of the matrices $\left([\tilde{\mathbf{L}}_1]^{-1}\tilde{\mathbf{L}}_1 - \mathbf{I}\right)$ and $\left([2\tilde{\mathbf{L}}_2^t]\tilde{\mathbf{L}}_1 - \mathbf{I}\right)$, respectively, for all frequencies and wavenumbers, calculated using double precision floating-point arithmetic. We observe that both figures show an error that is significantly greater than machine precision, due to error propagation through the successive steps of the calculation. Contrary to our expectation, the expression with the inverse operator returns a more accurate result than the expression with the transpose operator. If this were true, it would imply that thereis an error in either the eigenvectors or the flux-normalization of the system. However, by comparing this result with one obtained using a combination of rational and arbitrary precision arithmetic, we can confirm that the use of the transpose operator is more accurate. For example, at the centre frequency of 600 rad s^{-1} and a horizontal wavenumber of 1.5 m^{-1}, floating-point arithmetic calculations of $\left([\tilde{\mathbf{L}}_1]^{-1}\tilde{\mathbf{L}}_1 - \mathbf{I}\right)$ and $\left([2\tilde{\mathbf{L}}_2^t]\tilde{\mathbf{L}}_1 - \mathbf{I}\right)$ returned errors of 4×10^{-15} and 1×10^{-8}, respectively, while requiring respective computational times of 10 and 3 ms. By carrying out the above calculations with rational arithmetic and converting the final exact rational number to a 128-bit quadrupule precision result, the errors are reduced to 1×10^{-23} and 1×10^{-27}, respectively, while the computational times increase to 1.74 s and 1.34 s, respectively. Based on these results, we can conclude that the use of the transpose operator results in lower error at reduced computational expense, subject to a sufficiently precise numerical algorithm. However, due to the considerable increase in computational time with the implementation of rational and arbitrary precision arithmetic, it was necessary to carry out the modelling using double precision floating-point arithmetic. With this representation, $[2\tilde{\mathbf{L}}_2^t]\tilde{\mathbf{L}}_1$ was subject to more round-off error than $[\tilde{\mathbf{L}}_1]^{-1}\tilde{\mathbf{L}}_1$, therefore the transpose operator equivalent of the inverse was not used.

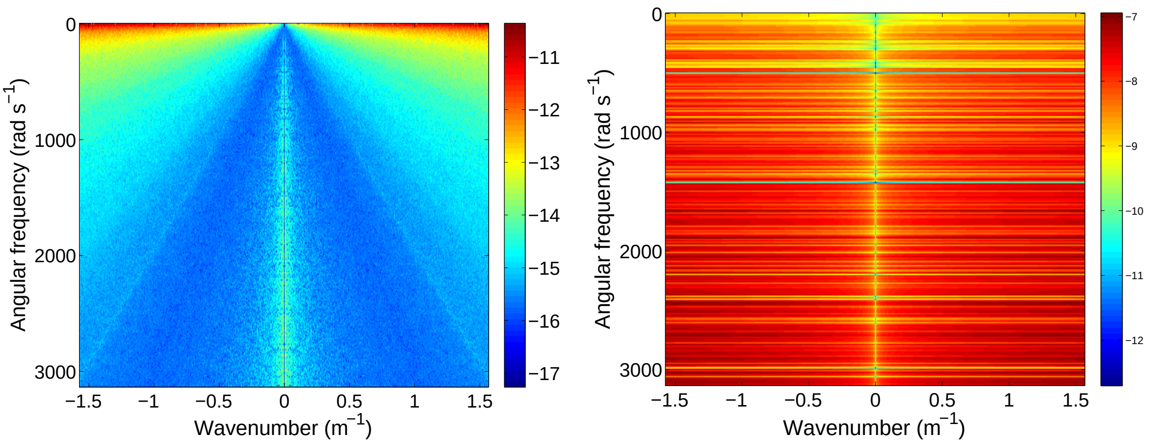

(a) $\tilde{\mathbf{L}}_1^{-1}\tilde{\mathbf{L}}_1 - \mathbf{I}$ **(b)** $2\tilde{\mathbf{L}}_2^t\tilde{\mathbf{L}}_1 - \mathbf{I}$

Figure 5-1: Comparison of the deviations of (a) $\left([\tilde{\mathbf{L}}_1]^{-1}\tilde{\mathbf{L}}_1 - \mathbf{I}\right)$ and (b)$\left([2\tilde{\mathbf{L}}_2^t]\tilde{\mathbf{L}}_1 - \mathbf{I}\right)$ from the expected null matrix using double precision floating-point arithmetic. Both figures are logarithmically scaled.

5-3 Source and receiver composition

The one-way wavefield source vector, as seen in Eq. (3-54), is comprised of upgoing and downgoing fast P-waves, slow P-waves, vertically polarized shear waves and transverse magnetic

polarized electromagnetic waves. Although all wavefields are accounted for in the one-way wave equation and reflection formalism, we will not consider slow P-wave sources or receivers due to their highly dispersive behaviour.
The two-way wavefield source vector of the P-SV-TM system was defined in Eq. (3-7). In carrying out numerical simulations using two-way wavefield sources, we will choose a subset of the listed source types. The types of sources that will be considered are two seismic and two electromagnetic sources. The seismic sources will be forces in the x_1 and x_3 directions and it will be assumed that the forces applied to the fluid and to the bulk are equal, such that $\tilde{f}_i^f = \tilde{f}_i^b$. The electromagnetic sources will be either an electrical source in the x_1 direction or a magnetic source in the x_2 direction. We can extract the desired sources from Eq. (3-7) and specify the following four two-way source vectors:

$$\tilde{\mathbf{d}}_{\mathrm{V}}^{\mathrm{f}_1} = \left(0, p_1 \tilde{f}_1^f, \tfrac{\rho^f}{\hat{\rho}^E} \tilde{f}_1^f - \tilde{f}_1^b, -\hat{\mathcal{L}} \tilde{f}_1^f, 0, 0, 0, 0\right), \tag{5-6}$$

$$\tilde{\mathbf{d}}_{\mathrm{V}}^{\mathrm{f}_3} = \left(0, 0, 0, 0, \tilde{f}_3^b - \tfrac{\rho^f}{\hat{\rho}^E} \tilde{f}_3^f, \tilde{f}_3^f, 0, 0\right), \tag{5-7}$$

$$\tilde{\mathbf{d}}_{\mathrm{V}}^{\mathrm{J}_1^{\mathrm{e}}} = \left(0, 0, 0, -\tilde{J}_1^e, 0, 0, 0, 0\right), \tag{5-8}$$

$$\tilde{\mathbf{d}}_{\mathrm{V}}^{\mathrm{J}_2^{\mathrm{m}}} = \left(0, 0, 0, 0, 0, 0, 0, -\tilde{J}_2^m\right). \tag{5-9}$$

These two-way wavefield sources are converted to one-way wavefields through the action of the decomposition operator. Whether or not the resulting one-way wavefields are angle dependent (i.e. have a polarity that switches at zero offset), is dependent on whether the decomposed sources are odd or even functions of offset. This can be seen in the corresponding entries of the decomposition operator. By analytically determining the one-way source vector $\tilde{\mathbf{b}}$ for each of the above sources, we find that the longitudinal waves created by the f_1, J_1^e and J_2^m sources are ray parameter dependent (i.e. odd), while the transverse waves are ray parameter independent (i.e. even). An f_3 source has the opposite behaviour, it creates ray parameter dependent transverse waves and ray parameter independent longitudinal waves. Note that the above listed sources are only a subset of the sources seen in Eq. (3-7): it would also be possible to define source vectors corresponding to, for example, the bulk deformation rate $\tilde{h}_{ij}$ or a vertical electric current source $\tilde{J}_3^e$. All two-way wavefield sources excite all eight one-way wavefields, but to varying degrees.
We will also limit the two-way wavefields that will be recorded: we choose receivers corresponding to measurements of the horizontal (v_1^s) and vertical (v_3^s) solid particle velocities, as well as the x_2 component of the magnetic field (H_2) and the x_1 component of the electric field (E_1). This corresponds to an array of horizontal geophones, vertical geophones, electric antennas, and magnetometers.

5-4 Transmission experiment

This section will detail the results of one-way and two-way transmission experiments. Here we will introduce the medium parameters of both the medium that is used in this section (Medium A) and the medium that will be introduced in the succeeding sections (Medium B). The parameters of the media correspond to those used by Shaw (2005) and De Ridder (2007) and are presented in Table 5-1. All other characteristic parameters, such as the elastic parameters, bulk conductivity and static coupling coefficient, are calculated from the values given in Table 5-1, using the equations of Chapter 2. De Ridder et al. (2009) relates Medium A to a porous, clean, water-saturated sandstone of low salinity; Medium B is also a clean sandstone, but of lower porosity and containing a conductive pore fluid.

Table 5-1: Medium characteristics of Media A and B.

Medium Parameter	Symbol	Medium A	Medium B
Porosity	ϕ	40 %	20 %
Permittivity of the fluid	ϵ^f	$80\epsilon_0$	$80\epsilon_0$
Permittivity of the solid	ϵ^s	$4\epsilon_0$	$4\epsilon_0$
Fluid density	ρ_f	1.0×10^3 kg m^{-3}	1.0×10^3 kg m^{-3}
Solid density	ρ_s	2.7×10^3 kg m^{-3}	2.7×10^3 kg m^{-3}
Shear modulus	G_{fr}	9.0×10^9 N m^{-2}	9.0×10^9 N m^{-2}
Viscosity	η	1.0×10^{-3} N s m^{-2}	1.0×10^{-3} N s m^{-2}
Rock permeability	k	1.3×10^{-12} m^2	1.6×10^{-12} m^2
Tortuosity	α_∞	3.0	3.0
Bulk modulus of framework of grains	K^{fr}	4.0×10^9 N m^2	4.0×10^9 N m^2
Bulk modulus of solid	K^s	4.0×10^{10} N m^2	4.0×10^{10} N m^2
Bulk modulus of fluid	K_f	2.2×10^9 N m^2	2.2×10^9 N m^2
Electrolyte concentration	C	1.0×10^{-4} Mol L^{-1}	1.0×10^{-2} Mol L^{-1}

The velocities of the four one-way wavefields of the P-SV-TM system are determined from the Equations of Section 3-2, where it was seen that the real parts of the complex velocities represent the real phase velocities while the imaginary parts are related to the wavefield attenuation. The real and imaginary parts of the complex velocities are plotted in Figure 5-2 for the longitudinal seismic waves and Figure 5-3 for the transverse seismic and electromagnetic waves. The highly dispersive nature of the slow P-wave and the EM wave can be recognized from the strong frequency-dependency of their wave velocities.

5-4-1 One-way transmission model

The geometry of the transmission model is shown in Figure 5-4. The model consists of a homogeneous layer with medium parameters corresponding to those of Medium A. As depicted, the source is located 197 m below the receiver line. In this simple example we will record the one-way wavefields generated by one-way sources. Since there are no interfaces in this homogeneous model, no conversions between any of the wave types will occur and only the same type of wavefield as was used for the source is recorded. For example, when using an upgoing fast P-wave as a source we will record the upgoing fast P-wave at the receiver. Figure 5-5 shows the response of the three measured one-way wavefields due to their respective sources. In each figure the arrival time corresponds to the one-way travel time; it can be clearly recognized that the electromagnetic wave has the highest velocity, followed by the fast P-wave and then the vertically polarized shear wave. The velocity of the wavefields can also be observed in the moveout of the sections. The electromagnetic wave

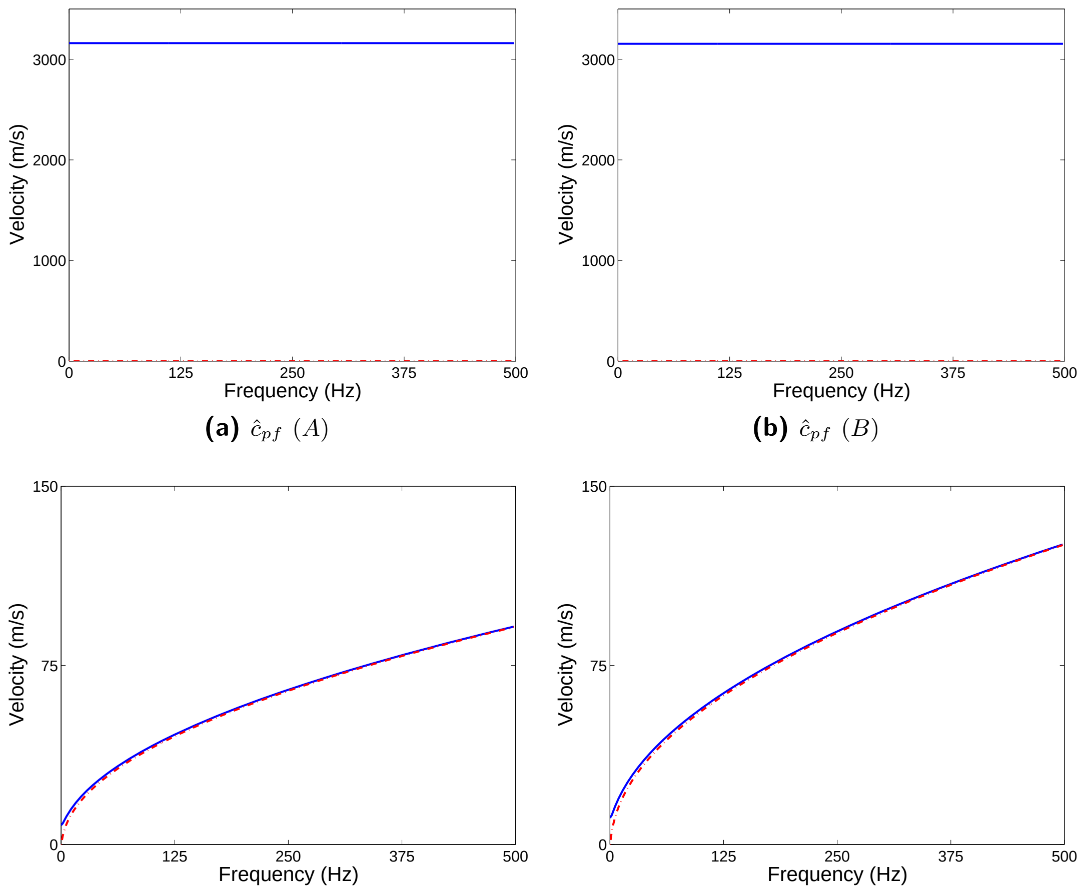

(a) $\hat{c}_{pf}$ (A) **(b)** $\hat{c}_{pf}$ (B) **(c)** $\hat{c}_{ps}$ (A) **(d)** $\hat{c}_{ps}$ (B)

Figure 5-2: Real (solid blue line) and imaginary (dashed red line) parts of the complex wave velocities of the longitudinal waves in Medium A (left column) and Medium B (right column). The upper panels correspond to the fast P-wave, while the lower panels correspond to the slow P-wave.

arrives essentially at all horizontally aligned receivers instantaneously, whereas the slower vertically polarized shear wave has increased hyperbolicity compared to both the EM wave and the fast P-wave.

5-4-2 Two-way transmission model

For modelling two-way sources and receivers, we implement the composition and decomposition operators of Chapter 3. The two-way sources are decomposed at the source level into one-way wavefields. These one-way wavefields are propagated to the receiver level, where they are composed back into the recorded two-way wavefields. Due to seismoelectric source coupling, each of the four two-way sources, presented in Section 5-3, will excite all of the one-way wavefields. Since the geometry of the transmission model is held the same as in the previous one-way wavefield case, we can examine which components of the two-way wavefields are due

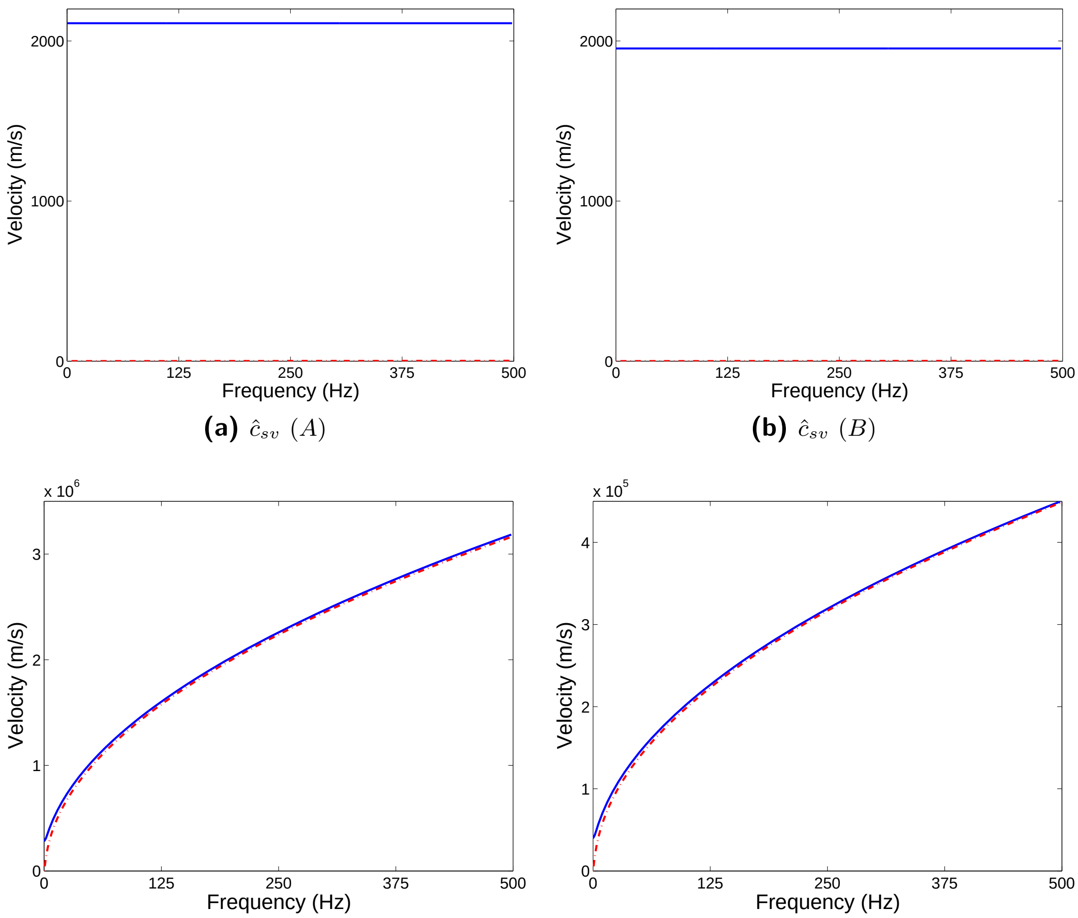

(a) $\hat{c}_{sv}\ (A)$ **(b)** $\hat{c}_{sv}\ (B)$

(c) $\hat{c}_{tm}\ (A)$ **(d)** $\hat{c}_{tm}\ (B)$

Figure 5-3: Real (solid blue line) and imaginary (dashed red line) parts of the complex wave velocities of the transverse waves in Medium A (left column) and Medium B (right column). The upper panels correspond to the vertically polarized shear wave, while the lower panels correspond to the transverse magnetic polarized electromagnetic wave.

to the different one-way wavefields. As explained in Chapter 3, all of the receivers, except for the H_2 receiver, are composed from a combination of all one-way wavefields. The magnitude and angle dependency of the contributions are calculated from the values of the corresponding eigenvectors. We can determine that the composition of transverse waves into the v_1^s, E_1 and H_2 receivers is ray parameter independent (i.e. even), whereas it is ray parameter dependent (i.e. odd) for the v_3^s receiver. These relations are exchanged for the longitudinal waves: the polarity of the longitudinal waves recorded by the v_3^s receiver are ray parameter independent, while they are ray parameter dependent for the v_1^s and E_1 receivers.
In Figure 5-6 we show recordings of v_1^s, v_3^s, E_1 and H_2 due to an external force on the bulk and fluid phases in the x_1 direction, f_1. The seismic sensors clearly display both the fast P-wave and the SV-wave; the magnitude of the source-coupled TM-wave is too weak to be seen. We can observe that the v_1^s receiver is relatively more sensitive to the SV-wave than the v_3^s receiver. As discussed in Chapter 1, the P-wave carries an electric field, known as the coseismic field, along with it as part of the material response. This coseismic electric

Figure 5-4: Source located 197 m below the receivers. Both source and receivers are located in Medium A.

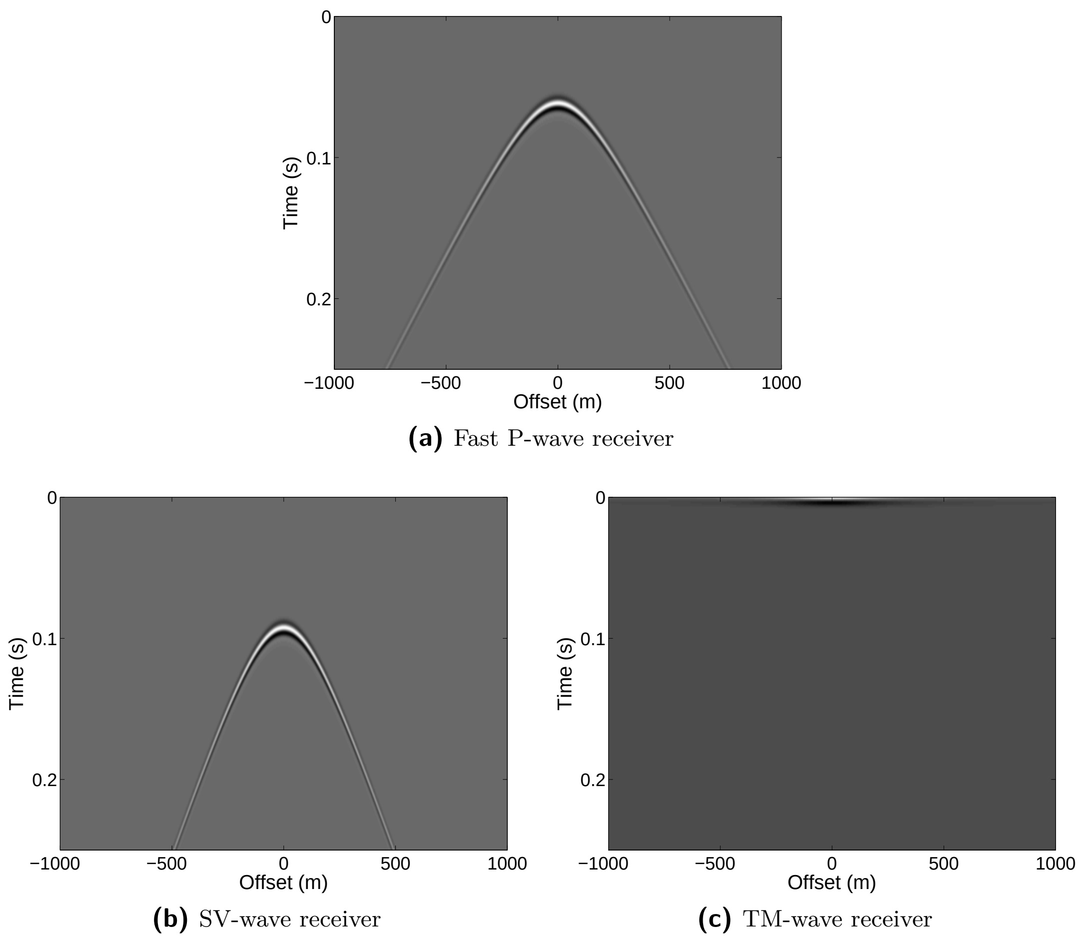

Figure 5-5: Transmission model one-way wavefield measurements of (a) fast P-wave, (b) SV-wave and (c) TM-wave, due to their respective sources.

field can be seen in the E_1 section, Figure 5-6c. Due to the relatively large amplitude of the electric field associated with the P-wave, neither the small induced electric field of the shear wave nor the electric field of the direct TM-wave are visible. Since coseismic magnetic fields are only weakly associated with a propagating shear wave (Haines and Pride, 2006), we are able to view both the magnetic field of the shear wave and the magnetic field of the TM-wave in Figure 5-6d. By factoring in the ray parameter dependency of the source with the ray parameter dependency of the receiver type, the polarities of the displayed sections can be explained. For example, when an f_1 source is decomposed into one-way wavefields, the resulting longitudinal waves are ray parameter dependent, while the transverse waves are not. These one-way wavefields are then propagated to the receiver location where they are composed into the desired two-way wavefield. If the receiver type also has a ray parameter factor in its composition of the longitudinal waves (as is the case for the v_1^s receiver), the signs of the two ray parameter terms cancel and the polarity of the recording wavefield is independent of the incidence angle. In other words, the product of two odd functions is an even function. Continuing on with this example, if the receiver type does not have a ray parameter dependency in its composition of longitudinal waves (i.e. the v_3^s receiver), then the sign of the ray parameter remains and the polarity will switch at zero offset. Simply put, the product of an odd function and an even function is an odd function. These remarks explain why the v_3^s receiver displays a polairty change, whereas the v_1^s, E_1 and H_2 receivers do not. Similar reasoning can be applied to the recordings resulting from an f_3 source, Figure 5-7, to understand why the v_3^s receiver shows a single polarity, whereas the x_1 and x_2 aligned receivers (v_1^s, E_1 and H_2) record the polarity of the propagating one-way wavefields. The relative magnitude of the P-wave is again greater for the v_3^s receiver than for the v_1^s receiver.

Recall that an electric current source will cause the movement of diffuse-layer counter ions, leading to the build up of pressure-gradients and the generation of a P-wave disturbance (Pride, 1994). The P-wave generated by an J_1^e source can be seen in the seismic receivers of Figure 5-8. As known from electromagnetic theory, a current source will produce magnetic fields, creating the response of the recorded magnetic field seen in Figure 5-8d. The second electromagnetic source that we consider is a J_2^m source. The recordings associated with the magnetic source are presented in Figure 5-9. It can be clearly recognized that the source generates a vertically polarized shear wave and an electric field.

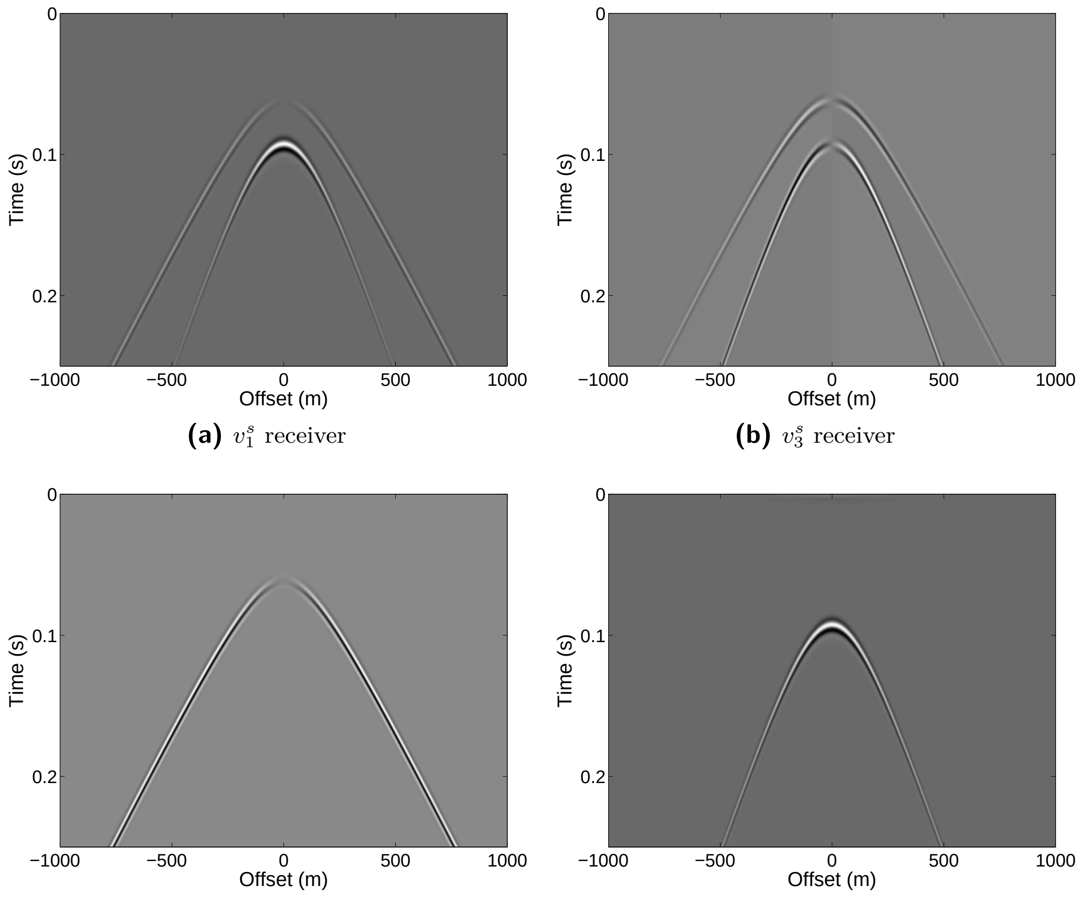

(a) v_1^s receiver

(b) v_3^s receiver

(c) E_1 receiver

(d) H_2 receiver

Figure 5-6: Transmission model two-way wavefield measurements of (a) v_1^s, (b) v_3^s, (c) E_1 and (d) H_2 due to an f_1 source.

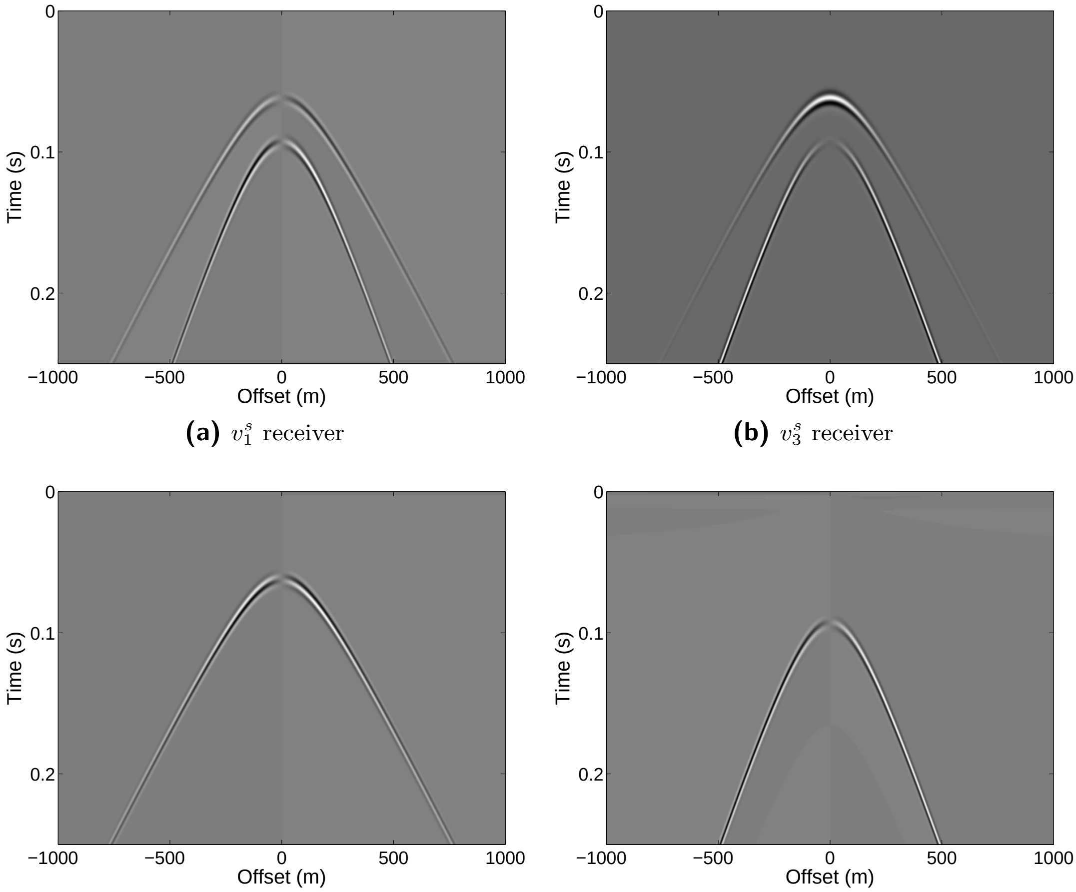

(a) v_1^s receiver

(b) v_3^s receiver

(c) E_1 receiver

(d) H_2 receiver

Figure 5-7: Transmission model two-way wavefield measurements of (a) v_1^s, (b) v_3^s, (c) E_1 and (d) H_2 due to an f_3 source.

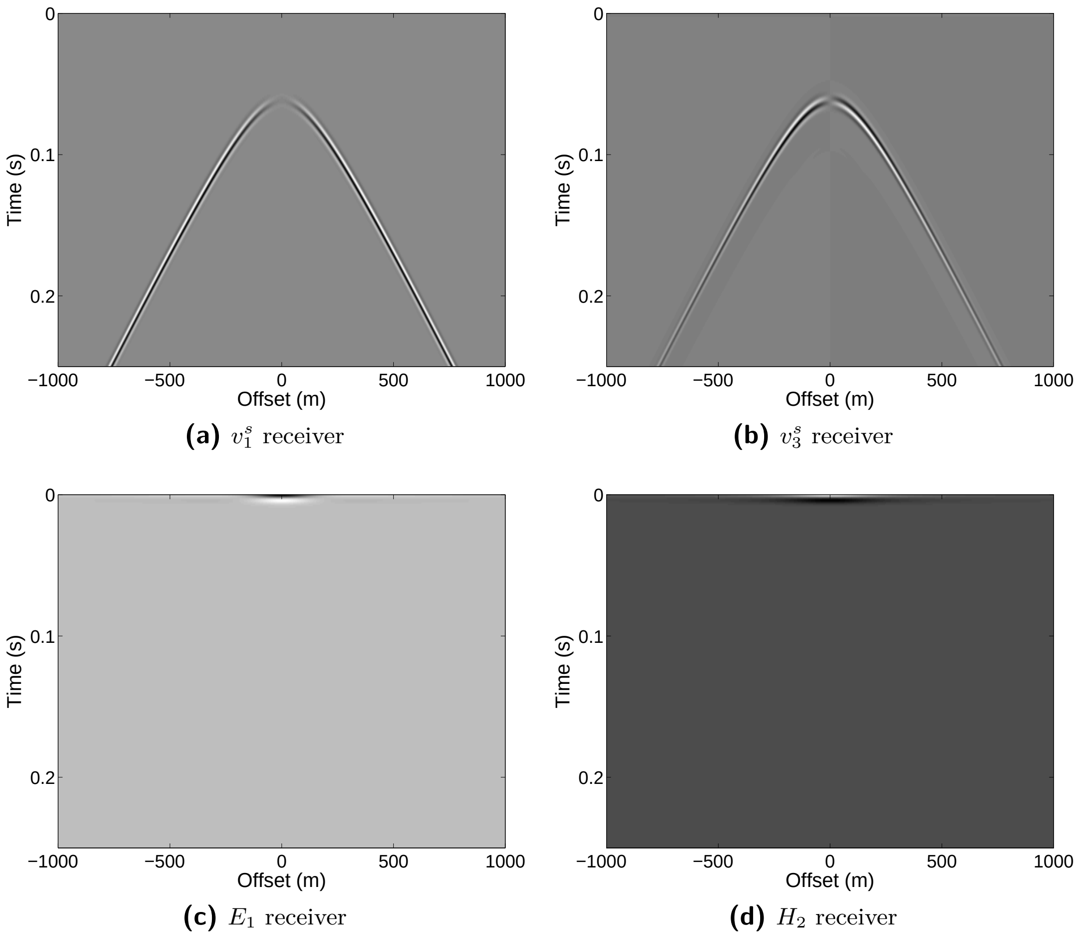

Figure 5-8: Transmission model two-way wavefield measurements of (a) v_1^s, (b) v_3^s, (c) E_1 and (d) H_2 due to an J_1^e source.

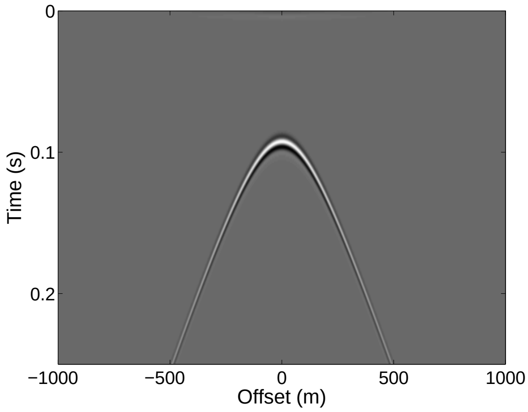

(a) v_1^s receiver

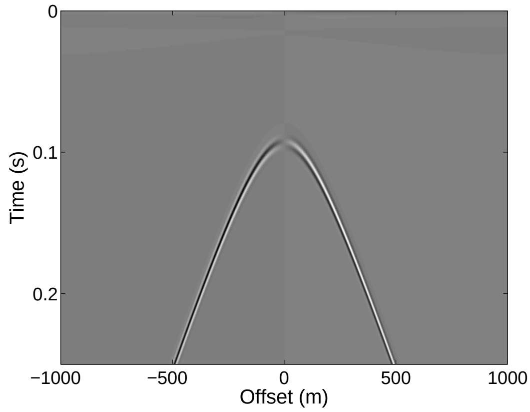

(b) v_3^s receiver

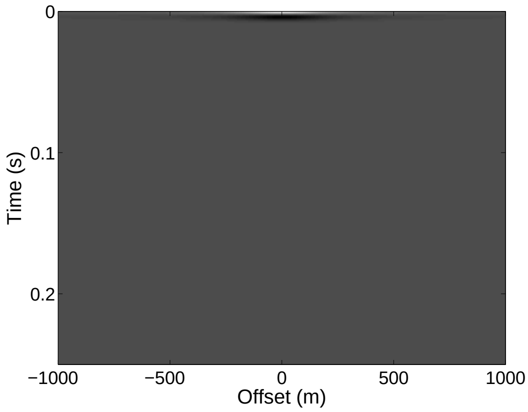

(c) E_1 receiver

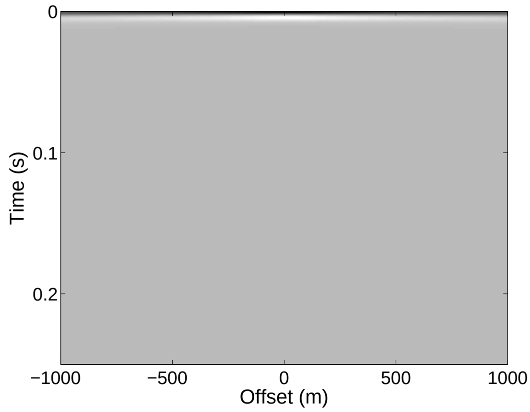

(d) H_2 receiver

Figure 5-9: Transmission model two-way wavefield measurements of (a) v_1^s, (b) v_3^s, (c) E_1 and (d) H_2 due to a J_2^m source.

5-5 Reflection experiments

We proceed here to a reflection experiment. The geometry of the experiment is shown in Figure 5-10, with the source located 1 m below the receivers which are 99 m above the interface between the two half-spaces. The distance from the receivers to the interface was chosen such that they would be 1 m below the free surface that will be introduced in the second half of this section. In this reflection experiment, the wavefield propagates downwards, reflects from the interface and returns to the receivers, covering a distance of 197 m at zero-offset.

In Figure 5-11, we plot the reflection coefficients of the interface between Medium A and

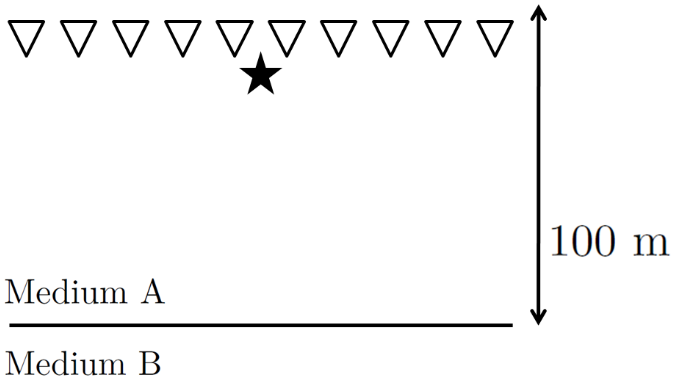

Figure 5-10: Geometry of the reflection experiment. The source is located 1 m below the receiver line and the receiver line is 99 m above the interface. The upper half-space has a thickness of 100 m and possesses medium parameters corresponding to Medium A, whereas the lower half-space consists of Medium B.

Medium B. We only present the reflection coefficients corresponding to conversions between seismic and electromagnetic waves, and vice versa. The horizontal axis represents the ray parameter (s/m) times the modulus of the velocity of the outgoing wave (m/s), while the vertical axis denotes the modulus of the reflection coefficient. Considering the fact that we use a plane wave approximation, we can express the ray parameter as a function of the ray's propagation angle (θ) and complex velocity:

$$p_1 = \frac{\sin(\theta)}{\hat{c}}. \tag{5-10}$$

Horizontal axis, $p_1|\hat{c}|$, values between zero and one correspond to reflection angles from zero to ninety degrees, respectively, and incidence angles less than the critical angle. At the critical angle, when $p_1|\hat{c}| = 1$, the outgoing waves are critically refracted, propagating along the interface. Horizontal axis values greater than one, $p_1|\hat{c}| \geq 1$, represent the creation of evanescent waves, i.e. waves that are bound to the surface and exponentially decrease in amplitude with distance, created when the incidence angle is greater than the critical angle. The angle of incidence is related to the reflection angle through Snell's law,

$$\frac{\sin\theta_i}{\sin\theta_r} = \frac{c_i}{c_r}, \tag{5-11}$$

where i and r represent the incident and reflected waves. Since the electromagnetic wave velocity is much greater than the seismic wave velocity, we can approximate this equation for seismoelectric conversions as

$$\sin\theta_{\mathrm{em}} = \sin\theta_{\mathrm{s}} c_{\mathrm{em}}, \tag{5-12}$$

where the subscripts 's' and 'em' stand for seismic and electromagnetic, respectively. From this equation, we can see that for a seismic-to-electromagnetic conversion, only a small range of incidence angles will generate a homogeneous EM-wave. However, if we consider electromagnetic-to-seismic conversions, we can deduce that a large range of incidence angles will generate a vertically propagating seismic wave.

Since the reflection coefficients show only a weak dependency on frequency (van der Burg, 2002), the results are solely presented at the centre frequency of the source wavelet. As can be seen in the figure, the magnitude of the reflection coefficients remains the same when the ingoing and outgoing waves are interchanged. This is a consequence of having flux-normalized the one-way system. At normal incidence, as discussed in Section 4-5-1, the reflection coefficient for $Pf \leftrightarrow TM$ is zero, whereas the SV-TM system remains coupled. Except for at normal incidence, the reflection coefficients of the $Pf \leftrightarrow TM$ conversions are greater than for the $SV \leftrightarrow TM$ conversions.

5-5-1 One-way reflection model

Once again we will start by looking at the one-way wavefields generated by one-way sources. The downgoing one-way wavefields will undergo seismoelectric conversions at the interface, producing four transmitted and four reflected waves. The relative amplitudes of the waves depend on the reflection and transmission coefficients of the interface, which are related to the angle of incidence and wave types of the ingoing and outgoing waves, as shown before. Since our interest is in seismoelectric coupling, we will solely display the source and receiver pairs that provide information on this coupling. For the one-way fast P-wave and SV-wave sources, we will display recordings of the TM-wave. Vice-versa, with a TM-wave source, we will record mechanical motion as captured by the fast P-wave and SV-wave receivers.

In Figure 5-12, two sections are displayed, corresponding to fast P-wave and SV-wave sources with a TM-wave receiver. At normal incidence, the P- and SV-TM systems are decoupled and there is no conversion between longitudinal waves and transverse waves. However, the SV and TM systems do remain coupled, such that seismoelectric conversion still occurs. The arrival times of the TM-waves in Figure 5-12 correspond to the one-way seismic travel times from the source to the interface; it is clear that the fast P-wave has a higher velocity than the SV-wave. The weak hyperbolic events that have the same arrival time as the Pf-TM and SV-TM reflections are associated with the impingment of the seismic waves on the interface. When a seismic wavefront impinges on a horizontal interface, the resulting charge asymmetry generates a homogeneous electromagnetic wave that propagates perpendicularly away from the interface, i.e. in the upgoing and downgoing directions. As the wavefront continues to propagate, the angle of incidence between the wavefront and the horizontal interface increases. Based on Snell's Law, we can determine that the critical angle occurs at very small deviations from normal incidence. At angles greater than the critical angle, the electromagnetic wavefields will be evanescent (Shaw, 2005). Thus, the hyperbolic events seen in Figure 5-12, correspond to the radiation of energy from evanescent electromagnetic wavefields.

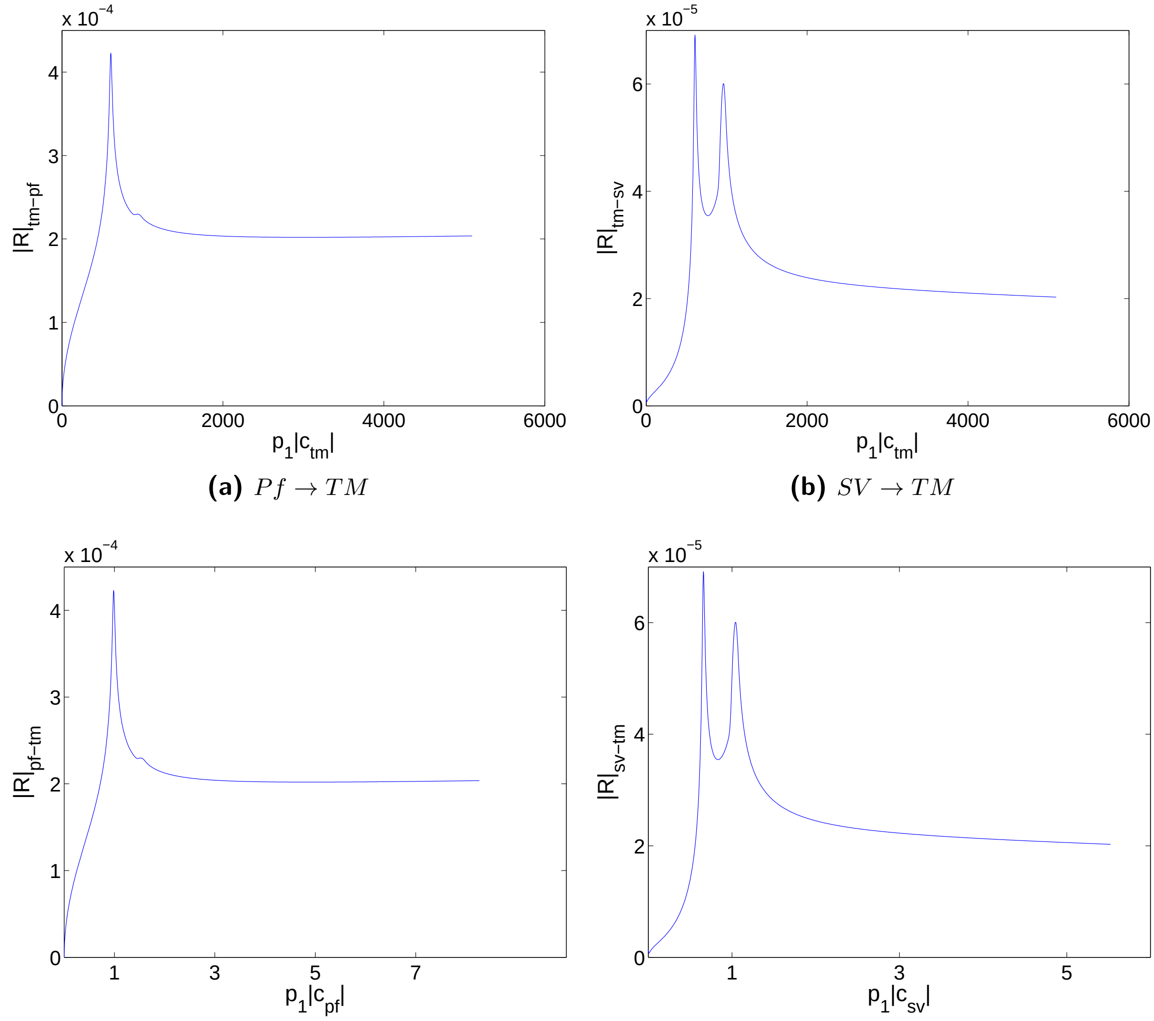

(a) $Pf \rightarrow TM$ **(b)** $SV \rightarrow TM$

(c) $TM \rightarrow Pf$ **(d)** $TM \rightarrow SV$

Figure 5-11: Reflection coefficients corresponding to conversions between seismic and electromagnetic waves, for a wave in Medium A incident on the interface between Medium A and Medium B. The velocity on the horizontal axis represents the velocity of the outgoing wave. (a) and (b) show the reflection coefficients for conversions from incident fast P- and SV-waves, respectively, to an outgoing TM-wave. (c) and (d) show the reflection coefficients for conversions from incident TM-waves to outgoing fast P- and SV-waves, respectively.

With a TM-wave source, we record the fast P-waves and SV-waves seen in Figure 5-13. The TM-wave arrives at all points on the interface simultaneously, each of which act as a point source for seismic waves, thereby generating an upgoing seismic plane wave. The one-way travel times now represent the travel time from the interface to the receivers. We can again note the arrival of a hyperbolic event with the linear interface response, having a similar cause as discussed before. In the case of electromagnetic-to-seismic conversions, Snell's Law indicates that vertically propagating seismic waves are generated at almost all angles of incidence. However, at far offsets the seismic waves that are generated are evanescent in nature (Shaw, 2005). We will use the term interface response to refer to both the electromagnetic

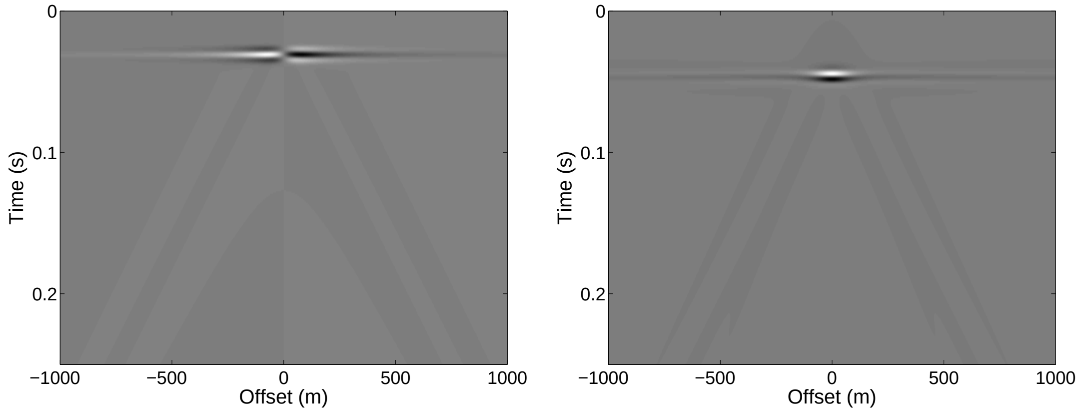

(a) Fast P-wave source **(b)** SV-wave source

Figure 5-12: Reflection model one-way wavefield measurements of TM-waves due to (a) fast P-wave and (b) SV-wave sources.

wave generated at an interface due to a seismic source and to the seismic plane wave generated simultaneously at all points on an interface due to an electromagnetic source; the context will distinguish between the two types.

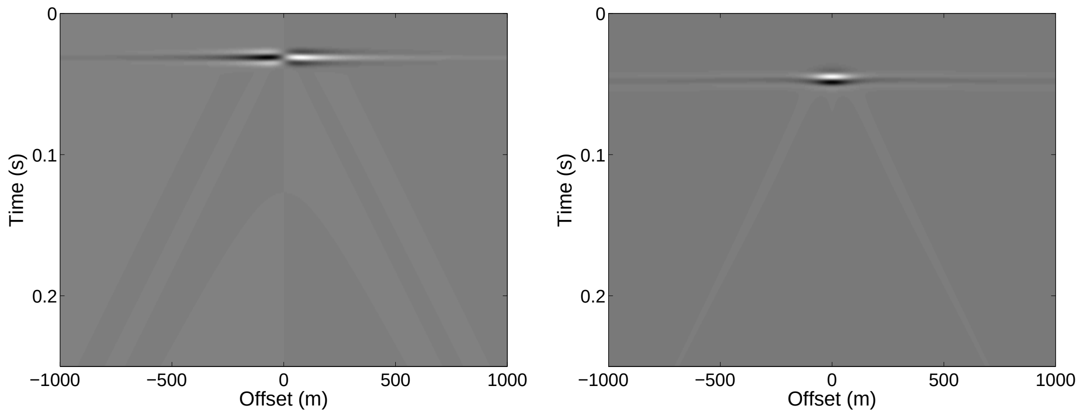

(a) Fast P-wave receiver **(b)** SV-wave receiver

Figure 5-13: Reflection model one-way wavefield measurements of (a) fast P-waves and (b) SV-waves due to a TM-wave source.

One-way reciprocity theorem

Reciprocity theorems interrelate the quantities of two admissable physical states that occur in a given domain. Simply stated, they predict the invariance of the material response, which manifests as the propagation of the wavefield, to interchanging the source and receiver types and locations (Wapenaar et al., 2001). Reciprocity theorems can be applied under certain conditions to both one- and two-way wavefields (Wapenaar, 1996). To ensure that the reciprocity principle could be applied to the one-way propagators of our laterally invariant

model, we flux-normalized the eigenvectors and the resulting one-way wavefields (Wapenaar, 1998). For a more in-depth explanation of reciprocity theorems for electromagnetic and elastodynamic one-way wavefields, the reader is referred to Wapenaar et al. (2001).
If we compare Figures 5-12 and 5-13, we observe that the same wavefields are recorded when the source and receiver types are switched. The opposite polarities that are observed when comparing the $Pf \leftrightarrow TM$ pair (Figures 5-12a and 5-13a) are a consequence of not laterally switching the source and receiver locations. This could be easily implemented by switching the directions of positive and negative offset in one of the figures, however, the presence of reciprocity is clear. The slight radiation pattern discrepancy seen in the $SV \leftrightarrow TM$ pair, Figures 5-12b and 5-13b, is a consequence of not vertically switching the source and receiver locations, such that there was a 3 m propagation distance difference between the two simulations. When both the source-receiver type and locations are interchanged, exact reciprocity is observed. Although not depicted, the reciprocity theorem also holds for elastodynamic one-way wavefields, in which SV-wave motion due to the reflection of a fast P-wave source is recorded, and vice versa.

5-5-2 Two-way reflection model

The two-way wavefield sources are physically multidirectional, producing both upgoing and downgoing waves. Since the source is positioned directly underneath the receiver line, any upgoing waves generated by the source would saturate the receiver response and mask the desired signal of the reflected waves. To ensure retrieval of the reflected waves, we applied a mute to the upgoing waves generated by the two-way wavefield sources. In Figure 5-14, we see measurements of E_1 and H_2 due to an external force in the x_1 direction. Both sections show five independent arrivals, the first of which represents the almost instantaneous TM-TM reflection. This is followed by two interface responses, corresponding to the one-way travel times of the Pf- and SV-waves, which are 0.031 seconds and 0.047 seconds, respectively, where $c_{pf} = 3160$ m/s and $c_{sv} = 2111$ m/s. The first hyperbolic arrival in the left panel is the coseismic field of the Pf-Pf reflection, arriving at the two-way fast P-wave travel time; the second represents the coseismic field of the SV-Pf reflection. In the right panel, the hyperbolic arrivals are both the coseismic fields of SV-wave arrivals. The first corresponds to the coseismic field of the Pf-SV reflection; the second, to the coseismic field of the SV-SV reflection. A close look at the hyperbola representing the SV-SV reflection shows a faint event diverging at an offset of approximately $\pm$ 250 m and continuing with a faster velocity. The offset at which it diverges corresponds to the critical angle of the SV-wave to fast P-wave conversion for both transmission and reflection. Therefore, this event can be attributed to a downgoing SV-wave that critically refracts along the interface at the fast P-wave velocities of the upper and lower media, before emerging from the interface at the critical angle as an SV-wave. With the vertically oriented seismic force source we record the sections shown in Figure 5-15. We observe the same events as using the f_1 source. However, with a vertically oriented force, the incident P-wave component is now of greater magnitude leading to a more defined Pf-TM reflection.

In Figures 5-16 and 5-17, we see the horizontal and vertical motions resulting from the reflections from an electric current source and a magnetic source, respectively. At zero time, all receivers record the solid motions associated with the TM-TM reflection. The next arrival in all four sections of these figures is the TM-Pf (and Pf-TM) reflection, arriving at the one-

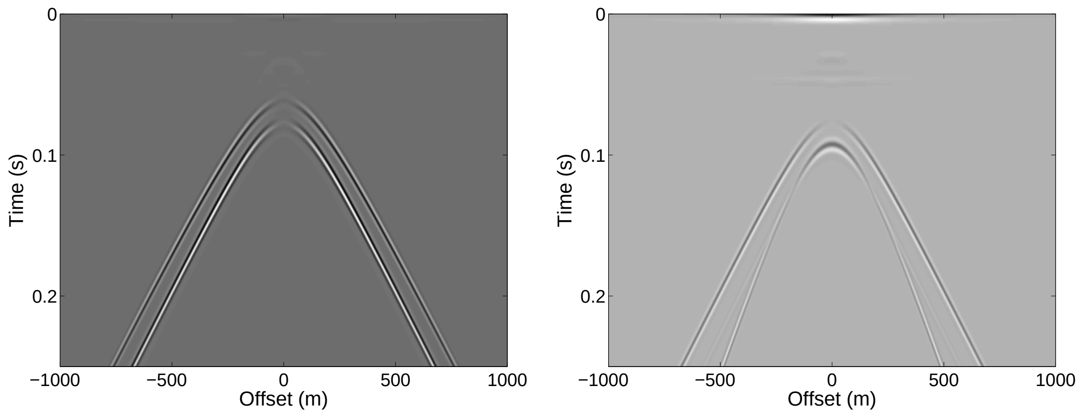

(a) E_1 receiver **(b)** H_2 receiver

Figure 5-14: Reflection model two-way wavefield measurements of (a) E_1 and (b) H_1 due to an f_1 source.

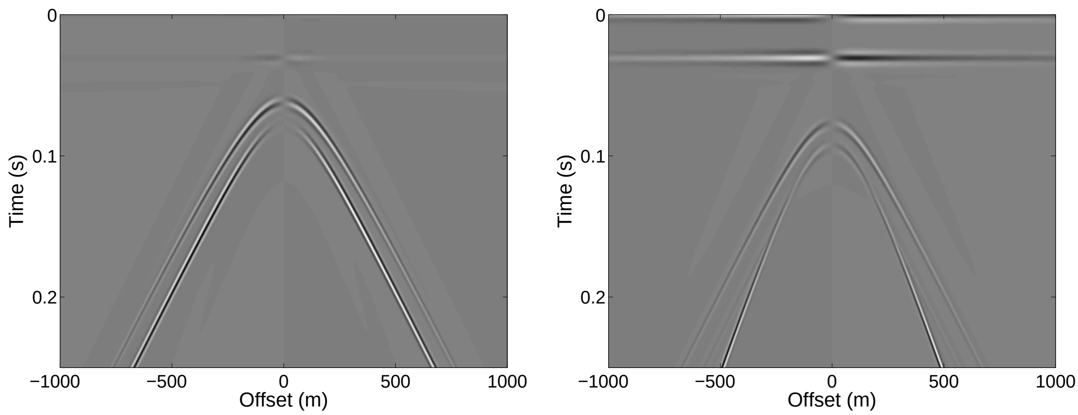

(a) E_1 receiver **(b)** H_2 receiver

Figure 5-15: Reflection model two-way wavefield measurements of (a) E_1 and (b) H_1 due to an f_3 source.

way P-wave travel time. As previously mentioned, the vertically oriented seismic receiver is more sensitive to P-wave motion and thus records a larger TM-Pf amplitude. In the J_2^m source and v_1^s and v_3^s receiver sections (Figure 5-17), we can detect the TM-SV (SV-TM) reflections, lagging the analogous P-wave reflections by approximately 0.01 s.

Two-way reciprocity theorem

Pride and Haartsen (1996) and Wapenaar (2003) derived reciprocity theorems for the two-way wavefields of the seismoelectric system in 3-D. The convolution-type reciprocity theorem for seismoelectric waves, under the assumption that the medium parameters of the two admissable

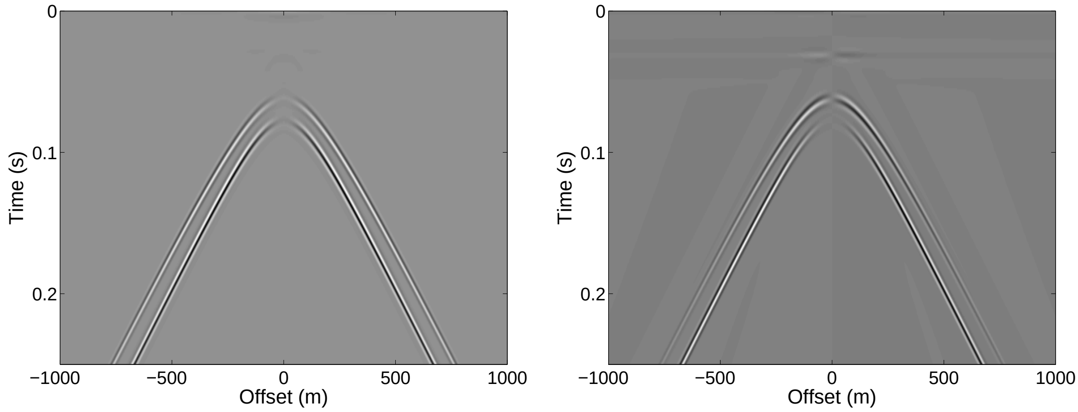

(a) v_1^s receiver **(b)** v_3^s receiver

Figure 5-16: Reflection model two-way wavefield measurements of (a) v_1^s and (b) v_3^s due to an J_1^e source.

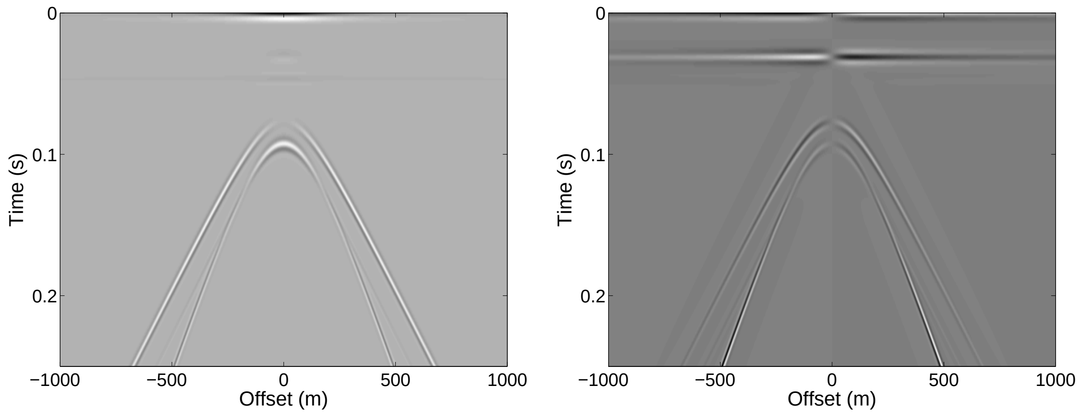

(a) v_1^s receiver **(b)** v_3^s receiver

Figure 5-17: Reflection model two-way wavefield measurements (a) v_1^s and (b) v_3^s due to a J_2^m source.

physical states are identical, is given by

$$\begin{aligned}
&\oint_{\partial D} \left[\epsilon_{ijk}\hat{E}_{i,A}\hat{H}_{k,B} - \epsilon_{ijk}\hat{H}_{k,A}\hat{E}_{i,B} - \hat{v}^s_{i,A}\hat{\tau}^b_{ij,B} + \hat{\tau}^b_{ij,A}\hat{v}^s_{i,B} + \hat{w}_{j,A}\hat{p}_B - \hat{p}_A\hat{w}_{j,B}\right] \mathrm{n}_j \mathrm{d}^2\mathbf{x} \\
&= \int_D \Big[\hat{J}^m_{k,A}\hat{H}_{k,B} - \hat{H}_{k,A}\hat{J}^m_{k,B} - \hat{J}^e_{i,A}\hat{E}_{i,B} + \hat{E}_{i,A}\hat{J}^e_{i,B} \\
&\qquad -\hat{f}^b_{i,A}\hat{v}^s_{i,B} + \hat{v}^s_{i,A}\hat{f}^b_{i,B} - \hat{f}^f_{j,A}\hat{w}_{j,B} + \hat{w}_{j,A}\hat{f}^f_{j,B}\Big] \mathrm{d}^3\mathbf{x},
\end{aligned} \tag{5-13}$$

where the subscripts A and B distinguish between the two states. By considering the medium at and outside the surface ∂D to be an unbounded homogeneous isotropic lossless solid and the wavefields of both state A and B to be causally related to the sources in D, the left-hand side of the above equation can be set to zero (Wapenaar, 2003). Furthermore, in 2-D, the volume domain D and its surface ∂D reduce to a surface domain S and its boundary ∂S, respectively. Source-receiver reciprocity relations can be determined from the terms on the right-hand side by considering the desired source functions in the two states and equating the remaining terms. For example, we will consider the source in state A to be an impulsive electric current source in the x_1 direction, occuring at zero time and located at $\mathbf{x} = \mathbf{x}_A$,

$$\hat{J}^e_{1,A}(\mathbf{x}, \omega) = \hat{s}_A(\omega)\delta(\mathbf{x} - \mathbf{x}_A), \tag{5-14}$$

where $\hat{s}$ is the source spectrum. The source in state B is an impulsive force source in the x_3 direction, with the forces on the bulk and fluid phases being equal, such that $\hat{f}^b_{3,B} = \hat{f}^f_{3,B} = \hat{s}_B(\omega)\delta(\mathbf{x}-\mathbf{x}_B)$. If all other sources are set to zero, we obtain the following reciprocity relation

$$\hat{E}_{1,B}(\mathbf{x}_A, \omega)/\hat{s}_B(\omega) = [\hat{v}^s_{3,A}(\mathbf{x}_B, \omega) + \hat{w}_{3,A}(\mathbf{x}_B, \omega)]/\hat{s}_A(\omega). \tag{5-15}$$

In Figure 5-18, we compare measurements of the above wavefields due to the sources specified for states A and B. The exact amplitude match between the $\pm$ offsets of the recorded electric field due to a vertical force source and the $\mp$ offsets of the recorded vertical motion due to an electric current source numerically confirms the validity of the above reciprocity relation. Although not presented, reciprocity was verified for other source-receiver pairs.

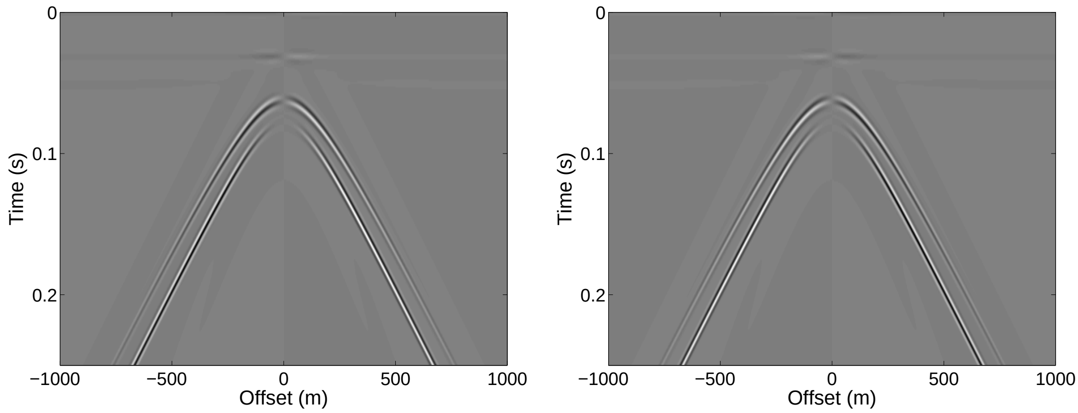

(a) E_1 receiver **(b)** v^s_3 and w_3 receiver

Figure 5-18: Seismoelectric two-way wavefield reciprocity. (a) dispays a recording of the x_1 electric field due to a force in the x_3 direction; (b) displays the recorded velocity in the x_3 direction due to an electric current oriented in the x_1 direction.

5-5-3 One-way reflection model with free surface

In Chapter 4 we determined the downgoing reflection matrix at the pressure-free surface. In this section, we implement this free surface into the previous reflection model, such that the free surface is located 1 m above the receivers (see Figure 5-19). With the presence of a free surface we expect to see multiple arrivals as a result of waves being reflected between the lower layer and the free surface.

To better understand the nature of the seismoelectric conversions at the additional interface,

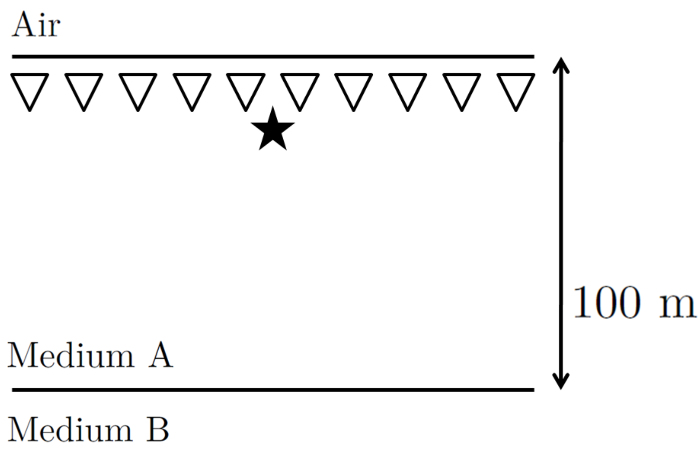

Figure 5-19: Geometry of the reflection experiment with a free surface. The receiver line is located 1 m below the free surface and 1 m above the source location. The distance from the free surface to the interface is 100 m. The upper half-space consists of Medium A and the lower half-space of Medium B.

we plot the reflection coefficients for an upgoing wave in Medium A incident on the free surface (see Figure 5-20). Although the reflection coefficient of the $SV \leftrightarrow TM$ conversion at normal incidence is small, it remains non-zero, as expected. It is also clear that there are stronger conversions between SV- and TM-waves than fast P- and TM-waves at subcritical incidence angles.

In Figure 5-21a, we see a recording of the TM-wave due to a downgoing fast P-wave source. The first event is a strong interface response generated at the lower interface by the downgoing P-wave, as seen previously in the absence of a free surface. The strong hyperbolic events are again interface responses, despite their non-linear nature. The first of the two strong hyperbolic events corresponds to a free surface interface response due to an upgoing Pf-Pf reflection, whereas the slower arrival corresponds to a free surface interface response due to an upgoing Pf-SV reflection. As previously explained, an electromagnetic interface response is not only created when a seismic wave first impinges on an interface, it continues to be generated at increasing offsets while the seismic wavefront at zero-offset propagates past the interface. Since the receivers are placed in near proximity to the free surface, they directly record the electromagnetic energy radiated from each point on the length of the free surface. Therefore, the interface response of the seismic-to-electromagnetic conversions at the free surface are recorded by the receivers with the same hyperbolicity as the incident seismic waves themselves. When the distance between the interface and the receivers is increased,

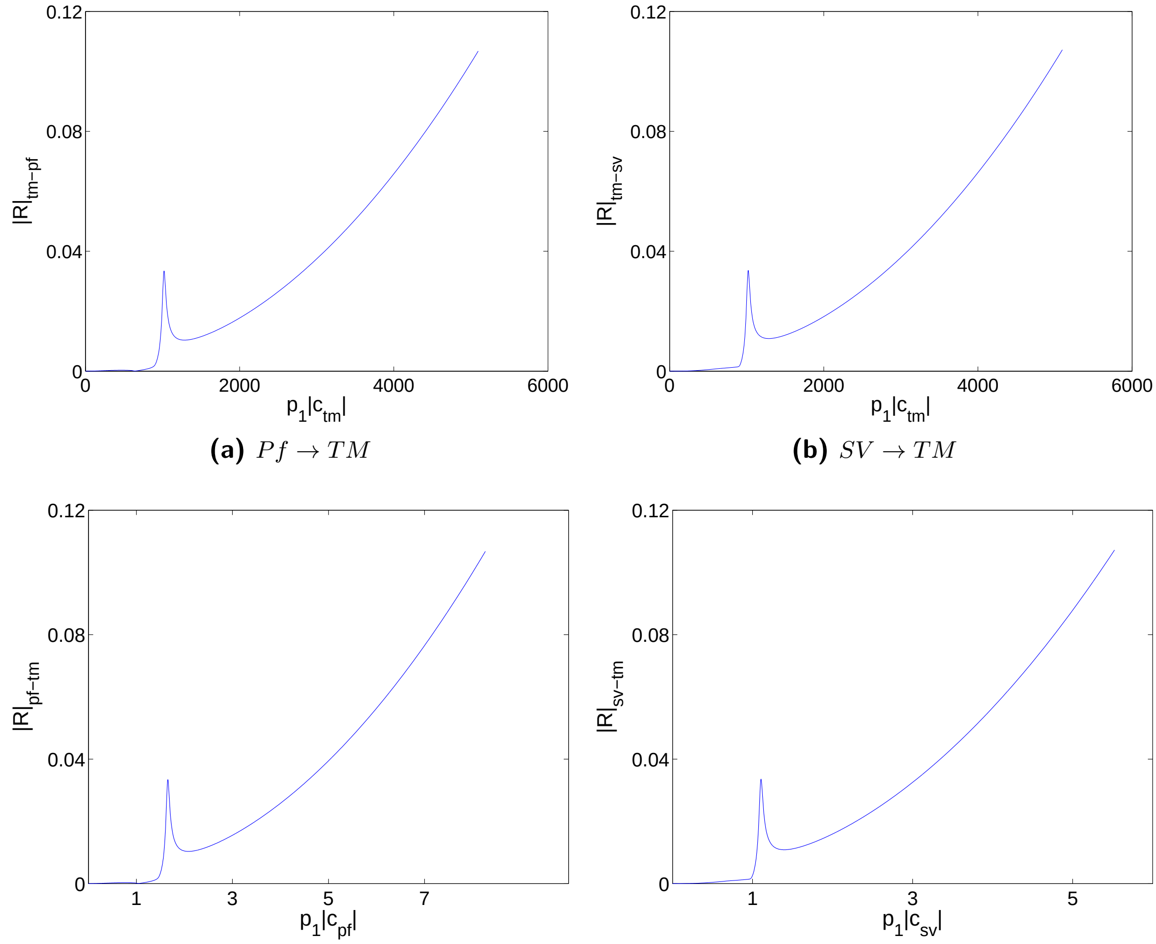

(a) $Pf \rightarrow TM$ **(b)** $SV \rightarrow TM$

(c) $TM \rightarrow Pf$ **(d)** $TM \rightarrow SV$

Figure 5-20: Reflection coefficients corresponding to conversions between seismic and electromagnetic waves, for an upgoing wave in Medium A incident on the free surface. The velocity on the horizontal axis represents the velocity of the outgoing wave. (a) and (b) show the reflection coefficients for conversions from incident fast P- and SV-waves, respectively, to an outgoing TM-wave. (c) and (d) show the reflection coefficients for conversions from incident TM-waves to outgoing fast P- and SV-waves, respectively.

the evanescent nature of the electromagnetic waves generated at non-normal incidence angles would result in the hyperbolicity of the interface response quickly decaying, leaving only a strong linear interface response. This can be seen in Figure 5-12a, where the receivers are located 100 m from the interface.

The TM-wave section, Figure 5-21a, shows multiple linear interface responses being generated at one-way P-wave travel time intervals and further hyperbolic interface responses radiating from the free surface. Figure 5-21b displays the TM-waves recorded due to an SV-wave source. At 0.05 s we observe the interface response created at the lower interface by the source seismic wave. Since the reflection coefficient for the SV- to TM-wave conversion at the interface between Medium A and Medium B (see Figure 5-11) is an order of magnitude lower than for the Pf- to TM-wave conversion, the recorded interface response is significantly weaker.

At this interface, upgoing P- and SV-waves are also generated. The interface response of the free surface from these waves are seen at the SV-Pf and SV-SV travel times, respectively.

In Figure 5-22, we display recordings of the fast P-wave and SV-wave due to a TM-wave

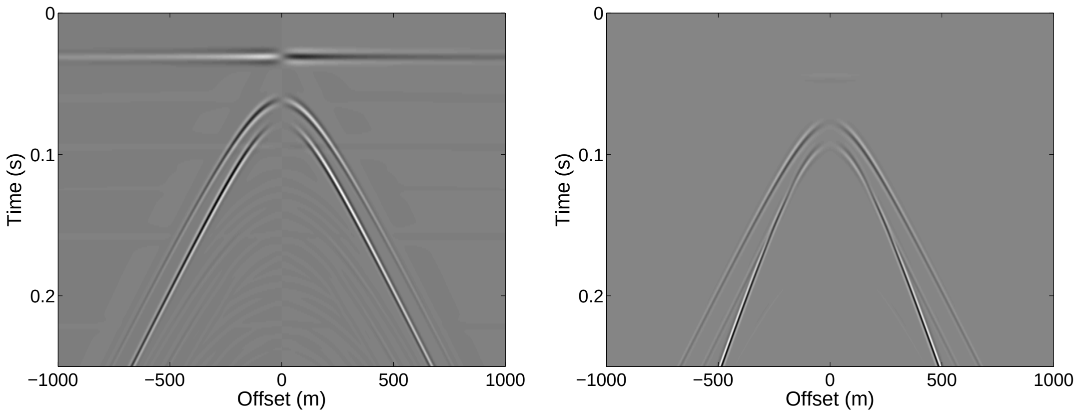

(a) Fast P-wave source **(b)** SV-wave source

Figure 5-21: Reflection model with free surface one-way wavefield measurements of TM-waves due to (a) fast P-wave and (b) SV-wave sources.

source. In both sections there is a weak arrival at zero time that represents the seismic waves generated at the free surface from the almost instantaneous TM-TM reflection. The strong event at 0.03 s in Figure 5-21a is the TM-Pf reflection from the lower interface. Multiples of this event are seen with decreasing amplitudes at two-way P-wave travel time intervals. In the SV-wave section, Figure 5-21b, we also observe an event at 0.03 s. We can attribute this observation to the conversion of the upgoing TM-Pf reflection to a downgoing SV-wave at the free surface. At 0.047 s, the one-way travel time of the SV-wave, we record the upgoing SV-wave converted at the lower interface from the source TM-wave. The first multiple of this wave is recorded at approximately 1.5 s, a two-way travel time increment.

5-5-4 Two-way reflection model with free surface

Now we will look at the effect of the free surface on the two-way wavefields. Once again, upgoing waves created at the source will be muted, such that the receivers will not record a direct wave or a source ghost. Figure 5-23 shows the inline component of the electric field and the crossline component of the magnetic field due to an inline force source. Due to the proximity of the receivers to the free surface, the hyperbolic arrivals are a superposition of four events: the coseismic field of the primary reflected upgoing seismic wave, the coseismic fields of the downgoing P- and SV-waves reflected or converted from the free surface and the electromagnetic interface response created at the free surface. The amplitude of the recorded hyperbolic arrival is dependent on the strength of the primary upgoing wave, as well as the magnitudes and signs of the relevant reflection coefficients. In both panels of Figure 5-23, the weak event at zero time is a recording of the TM-TM reflection. The three hyperbolic events correspond to the coseismic fields of the Pf-Pf, Pf-SV (and SV-Pf) and SV-SV reflections, respectively. As previously mentioned, these events have additional free surface contributions,

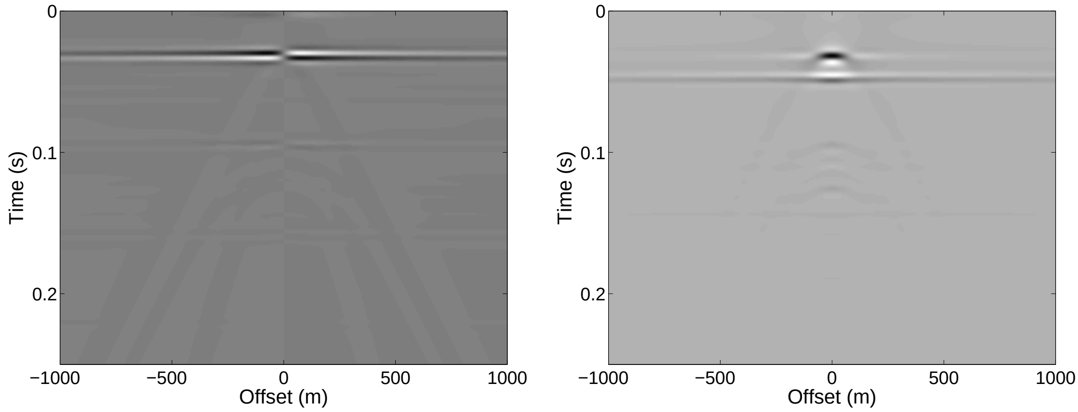

(a) Fast P-wave receiver **(b)** SV-wave receiver

Figure 5-22: Reflection model with free surface one-way wavefield measurements of (a) fast P-waves and (b) SV-waves due to a TM-wave source.

i.e. the event that we refer to as the coseismic field of the Pf-Pf reflection also has Pf-Pf-Pf, Pf-Pf-SV and Pf-Pf-TM components. The same clear hyperbolic events are seen in Figure 5-24, when a vertically oriented force is applied. However, in the recordings corresponding to this source, we are able to observe the interface response of the lower layer resulting from the downgoing fast P-wave. The reason that this event (and further interface responses from the lower layer) are visible is a consequence of both the amplitude of the downgoing fast P-wave of the f_3 source and the reflection coefficient for Pf-TM being larger than for the f_1 source and SV-TM, respectively. With both sources, we also observe internal multiples at increased travel times.

In Figure 5-25, we see recordings of the v_1^s and v_3^s wavefields due to an electric current source.

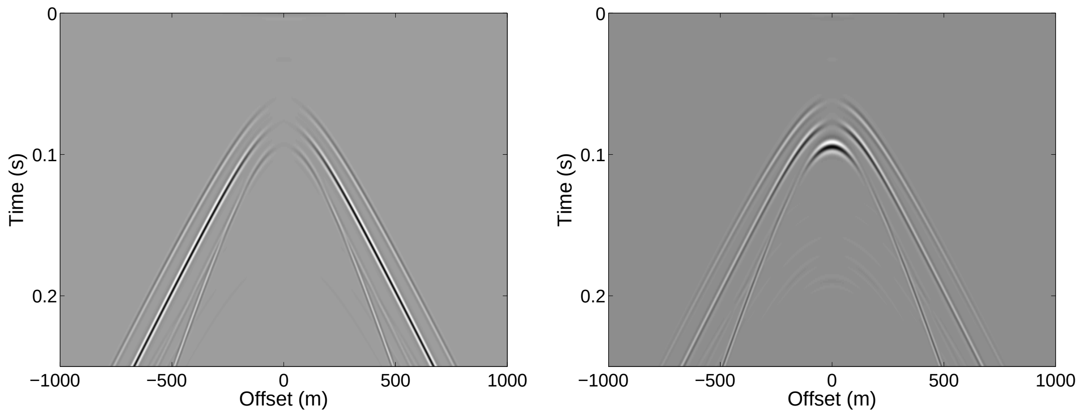

(a) E_1 receiver **(b)** H_2 receiver

Figure 5-23: Reflection model with free surface two-way wavefield measurements of (a) E_1 and (b) H_2 due to an f_1 source.

If we compare the left panel to the previously discussed reflection model without a free surface (Figure 5-16), we see that the presence of the free surface has strengthened the first arrival

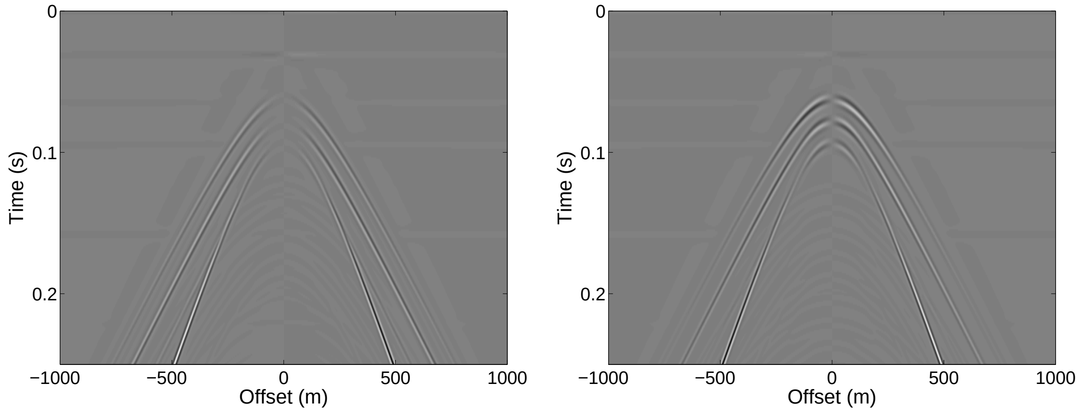

(a) E_1 receiver **(b)** H_2 receiver

Figure 5-24: Reflection model with free surface two-way wavefield measurements of (a) E_1 and (b) H_2 due to an f_3 source.

due to the superposition of the upgoing TM-Pf (and Pf-TM) reflection with the free surface converted reflections (e.g. TM-Pf-SV). The right panel displays the v_3^s wavefield and shows the numerous seismoelectric conversions occurring due to reflected waves repeatedly encountering the two interfaces.

In the case of a magnetic source, Figure 5-26, longitudinal waves are primarily activated. Five distinct events are recorded by the v_1^s receiver. The first event is the TM-TM reflection and its associated free surface conversions. This is followed by two interface responses: the TM-Pf reflection and the TM-SV (and SV-TM) reflection, and their free surface conversions. The two hyperbolic events that are recorded are the SV-Pf and the SV-SV reflections. The measurements of the v_3^s receiver are shown in Figure 5-26b; multiple seismoelectric conversions are clearly visible. The dominant linear event is the interface response of the lower interface, arriving at the one-way fast P-wave travel time.

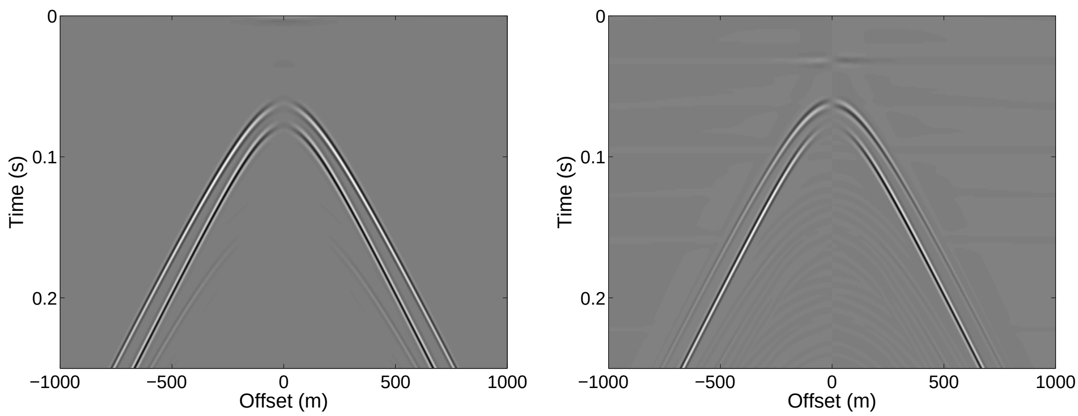

(a) v_1^s receiver **(b)** v_3^s receiver

Figure 5-25: Reflection model with free surface two-way wavefield measurements of (a) v_1^s and (b) v_3^s due to an J_1^e source.

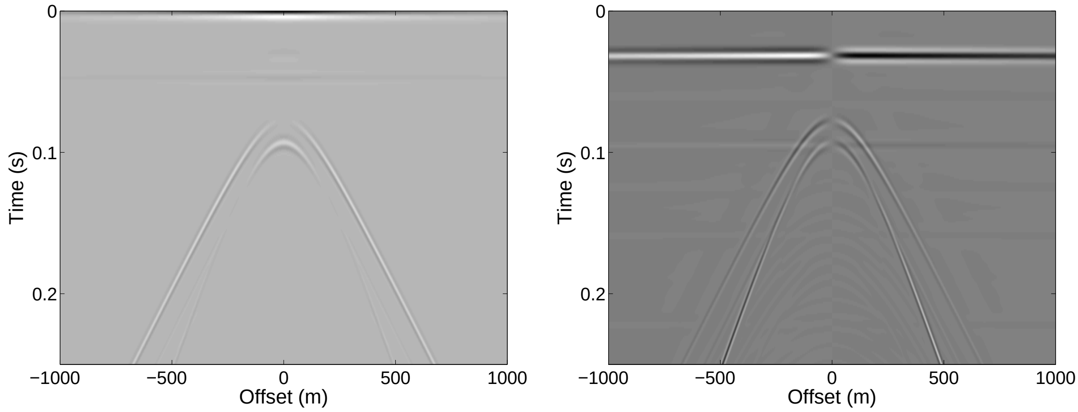

(a) v_1^s receiver **(b)** v_3^s receiver

Figure 5-26: Reflection model with free surface two-way wavefield measurements of (a) v_1^s and (b) v_3^s due to a J_2^m source.

5-6 Radiation pattern of interface response

In the above simulations of two-way seismic sources in a layered medium, we have clearly observed the presence of three electromagnetic signals: first, the EM wave that is generated at the source and is reflected at the interface as an EM wave; second, the independently propagating EM wave generated at an interface due to an incident seismic wave; and third, the coseismic EM field associated with propagating seismic waves. The third observation is generally of the greatest magnitude (Garambois and Dietrich, 2001) but only provides information on the fluid properties of the subsurface in the immediate vicinity of the receivers. The second observation, the interface response, is generally considered to be of greatest interest due to its creation at subsurface interfaces, however, it is both weak and rapidly attenuated. The rapid attenuation is due to spherical spreading of the radiated electromagnetic energy. To examine the relation between the recorded amplitude and the depth of the interface, we vary the depth of the interface and look at resulting changes in the recorded amplitude. In Figure 5-27, we plot the Amplitude Versus Offset (AVO) behaviour at a range of depths, as measured by an E_1 receiver with a P-wave source function. The interface response is created at the interface between Medium A and Medium B and, for this case of a horizontal planar interface separating two porous media, can be approximated by a vertical electric dipole (Thompson and Gist, 1993). The interface between the two media is successively moved through depths from 30 m to 130 m at 20 m intervals, while the source and receiver locations are kept constant. The rapid decay in the amplitudes of the measured electromagnetic signals with depth are clearly visible in Figure 5-27 and can be attributed to recording within the "near-field" of the generated EM field. The offset of the maximum amplitude increases as the depth of the seismoelectric conversion increases. We also notice a widening of the lobes due to the increased geometrical spreading of the wavefront with depth. We see that an analysis of the AVO behaviour of the interface response could provide information on the depth of the target interface. The normal moveout of the interface response could also lead to an estimate on the subsurface EM wave velocity (Gharibi et al., 2003).

Thompson and Gist (1993) found that the electric field of the interface response can be represented by an electric multiple. However, they also noted that since the first Fresnel zone has the greatest contribution to the radiation, following Fresnel zones can be neglected. The radiation of the first Fresnel zone, for a seismoelectric interface response, shows a simple dipole symmetry (Thompson and Gist, 1993; Garambois and Dietrich, 2001). We can thus compare the modelled interface response to the electric field radiated from a vertical dipole through the following formula (Griffiths, 1999),

$$E_x = \frac{d}{4\pi\hat{\varepsilon}_{\mathcal{L}}}\frac{3x_1 z}{r^5}, \tag{5-16}$$

where $r = \sqrt{x_1^2 + z^2}$ describes the radius, d denotes the bipolar moment of the dipole, and $\hat{\varepsilon}_{\mathcal{L}}$ is the modified effective electric permittivity of the medium. In Figure 5-28, we compare the radiation pattern measured by the inline component of the electric field, due to an interface at 100 m depth, with the radiation pattern of a true vertical dipole. Since we cannot theoretically ascertain the value of the bipolar moment that should be used, we adjust the value such that the maximum of the two curves is identical. The radiation patterns are in good agreement, although the dipole approximation has a more pronounced decrease in amplitude with source-receiver offset. One possible explanation for this observation is that the approximation with

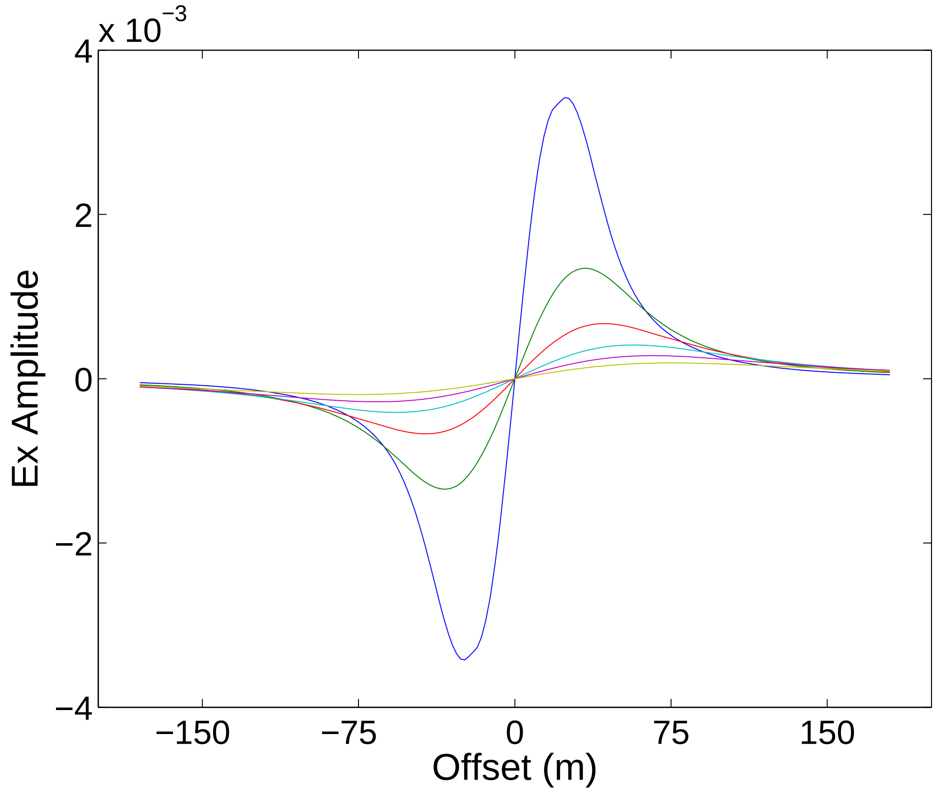

Figure 5-27: Radiation pattern of the inline component of the electric field generated by a downgoing fast P-wave incident on the interface separating Medium A from Medium B. The amplitude of the field decreases as the depth of the interface increases. The five responses in decreasing amplitude correspond to depths of 30 m (blue), 50 m (green), 70 m (red), 90 m (turquoise), 110 m (magenta) and 130 m (yellow), respectively.

a vertical electric dipole neglects contributions from additional seismoelectric conversions occuring along the interface.

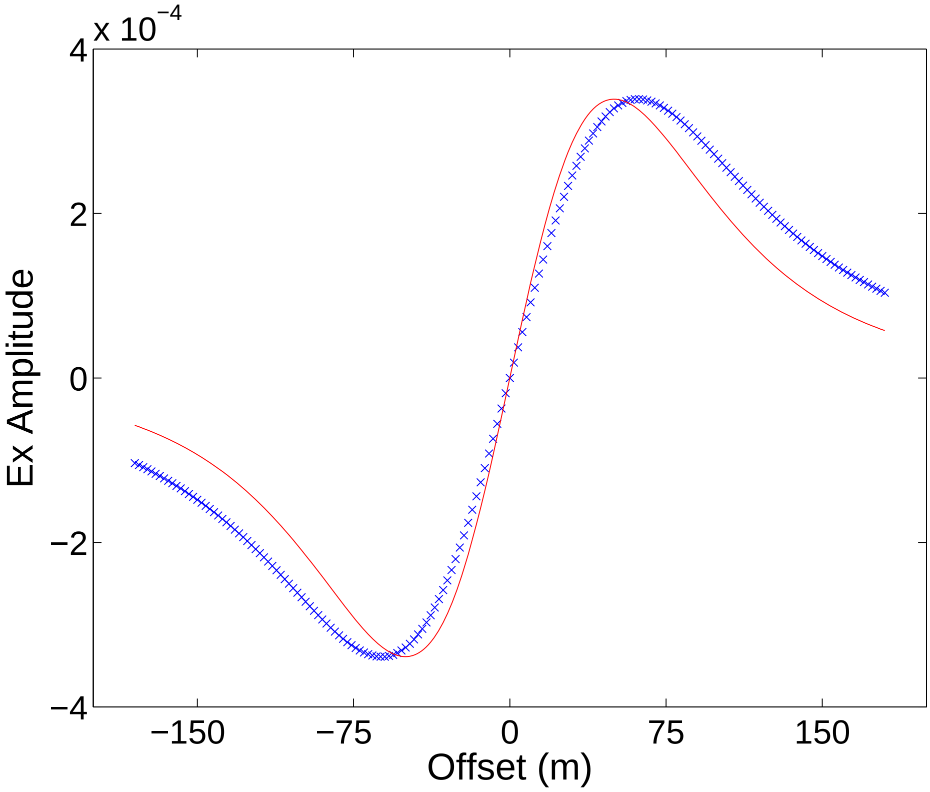

Figure 5-28: Comparison of the radiation pattern of the inline component of the electric field generated by a downgoing fast P-wave with the theoretical electric field radiated by a vertical dipole. The strength of the vertical dipole has been scaled to the maximum of the interface response. Both the interface and dipole are located at 100 m depth.

5-7 VESP

To maximize the strength of the recorded signal, it is desireable to have the receivers located as close as possible to the layer of interest. This mitigates the strong attenuation of the interface response. To this end, Vertical ElectroSeismic Profiling (VESP) has been suggested as one potential use of electroseismics. By carrying out VESP, the receivers can be placed in near proximity to the target layers and thus one can recover a stronger signal than would be recorded at the surface.

The survey geometry of the VESP model used in the numerical modelling is shown in Figure 5-29. A 60 m thick layer with lower porosity and higher conductivity (Medium B) is placed

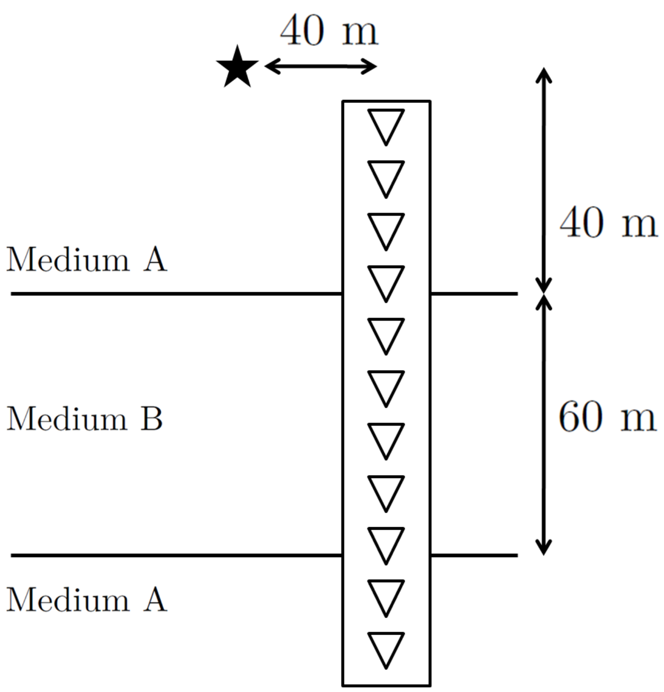

Figure 5-29: Three-layer model with first layer at 40 m and second layer at 100 m. The vertical receiver line is offset 40 m from the source position and begins at 9 m depth. Receivers are spaced every 5 m down to a total depth of 159 m.

between two layers with the same medium parameters (Medium A). The source is located 40 m above the upper interface. The vertical receiver line has a 40 m lateral offset from the source location and extends from 9 to 159 m depth with a spacing of 5 m. We record both one-way and two-way wavefields; in both cases the source emits a downgoing fast P-wave, corresponding to a spherically symmetric explosion.

5-7-1 One-way wavefields

We record the upgoing and downgoing constituents of the fast P-wave, the SV-wave and the TM-wave. When the downgoing source P-wave hits the first interface, it will generate all eight one-way wavefields. The downgoing wavefields will then undergo a further conversion at the second interface, each generating a further eight one-way wavefields. In Figure 5-30, the recorded one-way wavefields are displayed. Note that all amplitudes are scaled to the maximum amplitudes of each respective section. The fast P-wave section, Figure 5-30a, shows the source wavelet at 0.01 s before it propagates through the layered model. When it reaches the first interface at 40 m, there is a reflection with a polarity switch due to the negative sign of the reflection coefficient at that interface. The majority of the energy remains within the transmitted wave, which undergoes another reflection once it reaches the second interface. At 44 m and 0.06 s, we can see a multiple as the wave that was upward reflected from the lower interface is downward reflected from the upper interface. At each point that the wave is incident on an interface, energy is split between the four upgoing and the four downgoing one-way wavefields that are created. In Figure 5-30b, we see the SV-waves resulting from converted energy of the P-wave source. The first conversion occurs at 40 m and 0.015 s, when a fraction of the initial P-wave energy is converted into upgoing and downgoing SV-waves. The P-wave continues propagating through the layer (not seen in this figure) and generates another converted SV-wave at 100 m depth and 0.035 s. The SV-wave created at the first interface undergoes the expected reflection and transmission at the second interface. In the electromagnetic section, Figure 5-30c, we see the creation of two interface responses. The first interface response is created when the source P-wave traverses the upper interface at 0.015 s; this response is immediately propagated through the upper and middle media. As expected, the strength of the electromagnetic signal is rapidly attenuated. The amplitude of the response is clearly greater in the second medium due to its decreased effective electric permittivity $\hat{\varepsilon}_{\mathcal{L}}$ which, as seen in the above equation for the strength of a vertical electric dipole, is a governing parameter in the strength of the observed electromagnetic signal. The second interface response, seen at 0.055 s, is generated when an upgoing fast P-wave is incident on the upper interface after being reflected from the lower boundary. Since the P-wave has lost energy during its propagation, the amplitude of the second interface response is considerably lower.

5-7-2 Two-way wavefields

The two-way wavefields that we record are composed from the one-way wavefields that were discussed in the previous section. We again consider four receivers: two that measure motion in the inline and vertical direction and two that record the electric and magnetic fields in the inline and crossline directions, respectively. In the v_1^s and v_3^s receivers of Figure 5-31, we see a combination of the direct, reflected and transmitted P-wave and the reflected and transmitted converted SV-waves and converted TM-waves. The shear waves can be more clearly recognized on the v_1^s section; e.g. the Pf-SV conversion at the first interface propagating downwards with the velocity of the shear wave and arriving at the final receiver at a travel time of 0.75 s. As discussed before, the v_3^s receiver is more sensitive to P-wave arrivals, as evidenced by the clear Pf-Pf reflection from the second interface. The interface responses are not visible in these figures due to the overwhelming amplitudes of the seismic waves.

Figure 5-32 displays the recordings of the E_1 and H_2 receivers. The first events seen in the E_1 recordings are the coseismic fields of the downgoing fast P-wave source. When this P-wave reaches the interface it creates an independently propagating electromagnetic signal, which travels through the second layer instantaneously, arriving at all the receivers in

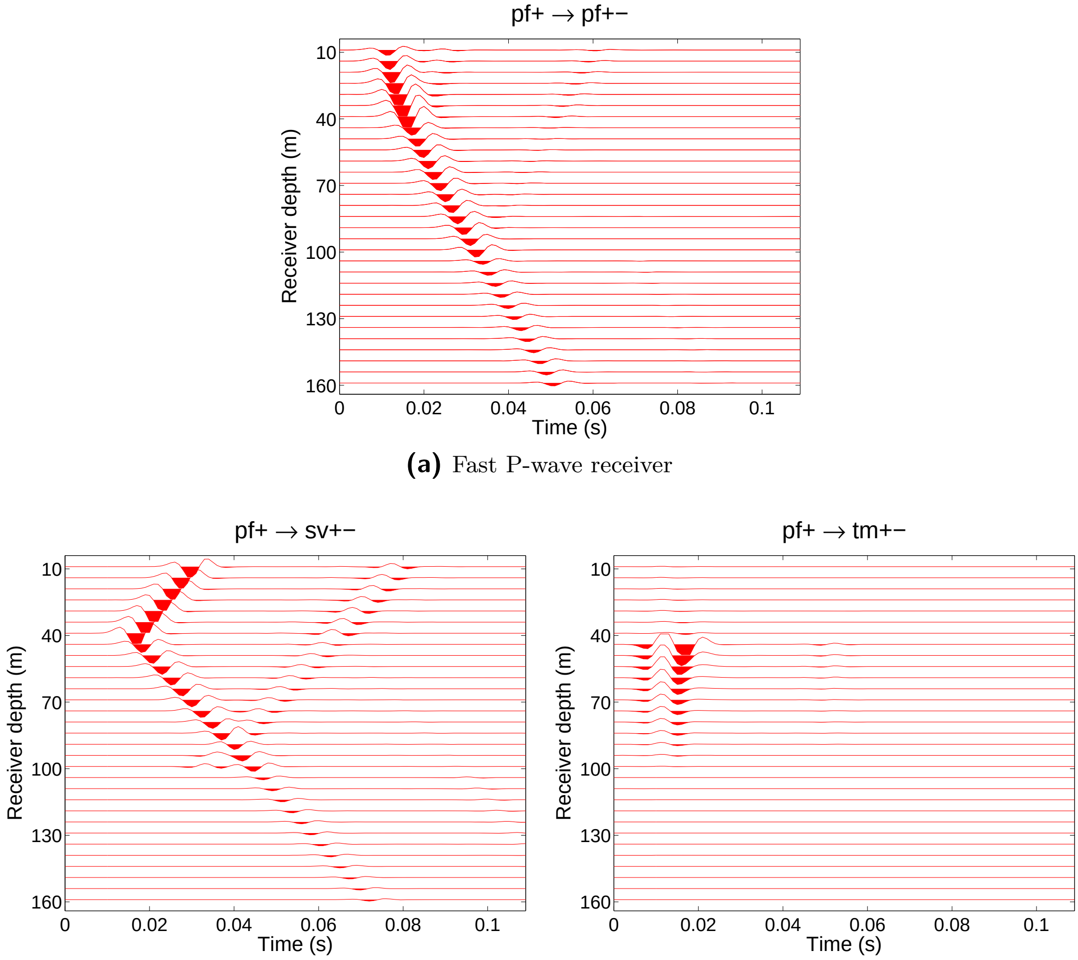

(a) Fast P-wave receiver

(b) SV-wave receiver

(c) TM-wave receiver

Figure 5-30: VESP one-way wavefield measurements of (a) fast P-waves, (b) SV-waves and (c) TM-waves due to a fast P-wave source.

Medium B simultaneously. As observed from the TM-wave recordings, the amplitude of the interface response rapidly decreases with depth. In both sections, we can also observe the electromagnetic signal of the second interface response, created by the upgoing fast P-wave impinging on the upper interface at a time of 0.055 s.

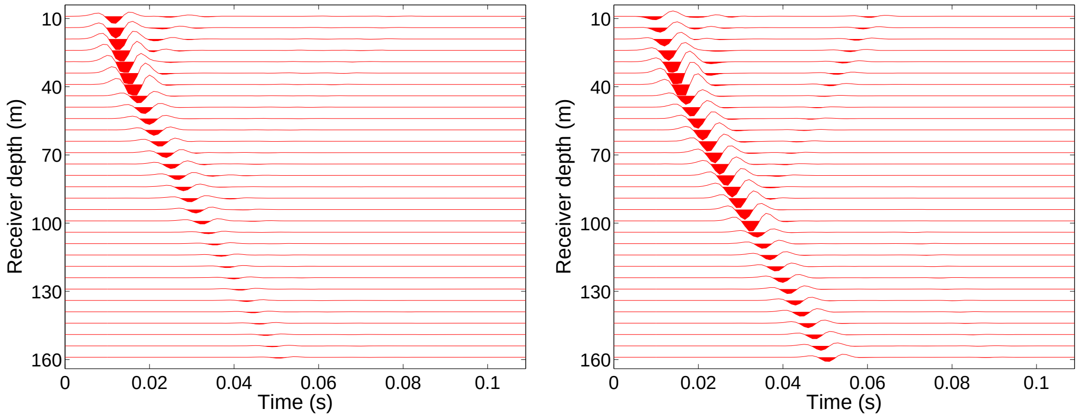

(a) v_1^s receiver **(b)** v_3^s receiver

Figure 5-31: VESP two-way wavefield measurements of (a) v_1^s and (b) v_3^s due to a fast P-wave source.

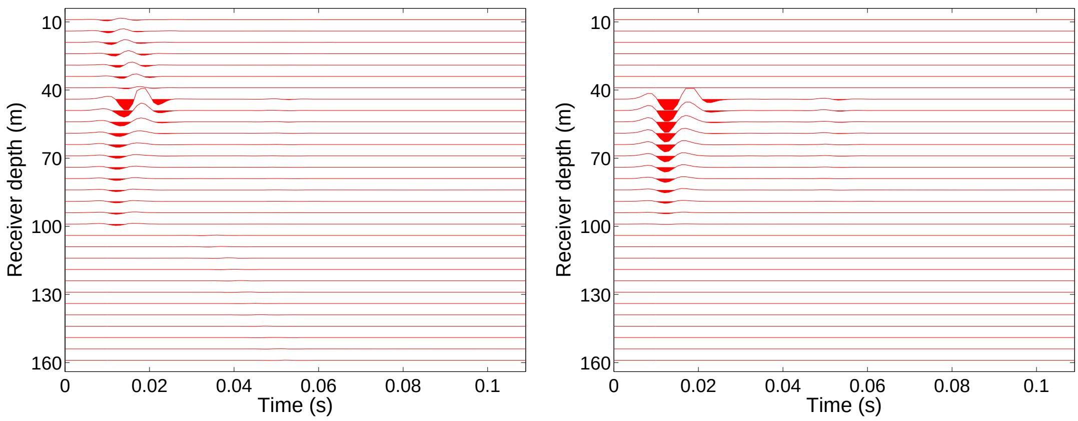

(a) E_1 receiver **(b)** H_2 receiver

Figure 5-32: VESP two-way wavefield measurements of (a)E_1 and (b)H_2 due to a fast P-wave source.

5-8 Aquifer monitoring

The sensitivity of the seismoelectric method to pore fluid properties, such as ion concentration and viscosity, makes it well suited to the monitoring of aquifers (Garambois and Dietrich, 2002; Dupuis et al., 2007). In this section we will simulate changes to the fluid properties of a saturated sandstone reservoir. Garambois and Dietrich (2002) performed a global sensitivity study and found porosity, permeability, fluid salinity and fluid viscosity to be the most influential parameters in seismoelectric conversions. The changes we will consider will be a change in ion concentration, corresponding to a salt intrusion into the aquifer, and changes in the fluid's dielectric permittivity, viscosity and density, all corresponding to the influx of a contaminant. The geometry of the experiment, shown in Figure 5-10, will be the same as for the reflection experiments of Section 5-5, however with changes to the medium parameters. The upper layer will represent the vadose (unsaturated) zone and the lower layer, the saturated zone. We will take both layers to be members of the same geological unit, thus having the same medium parameters, with the exception of the conductivity. We model a porosity of 30%, a rock permeability of 1×10^{-12} m^2, and an electrolyte concentration of 1.0×10^{-4} Mol L^{-1}. The conductivity of the upper layer will be fixed to 10% less than that of the initial saturated layer. All other medium parameters correspond to those of Medium A (see Table 5-1).

The scenarios that we are considering are shown in Table 5-2; the values chosen for the medium parameters of the contaminated lower layer are approximated to 20% and 40% saturation by an unspecific nonaqueous phase liquid (NAPL) (Carcione et al., 2003), the largest class of groundwater contaminants (Sneddon et al., 2000). Figure 5-33 shows changes in

Table 5-2: Aquifer contamination parameters

Scenario	C (Mol L^{-1})	ϵ_r^f	η (N s m^{-2})	ρ_f (kg m^{-3})
Initial state, t_0	1.0×10^{-4}	80	1.0×10^{-3}	1.00×10^3
Salt intrusion, t_{s1}	2.0×10^{-4}	80	1.0×10^{-3}	1.00×10^3
Salt intrusion, t_{s2}	1.0×10^{-2}	80	1.0×10^{-3}	1.00×10^3
Salt intrusion, t_{s3}	1.0	80	1.0×10^{-3}	1.00×10^3
Contaminant, t_{c1}	1.0×10^{-4}	44	0.9×10^{-3}	1.04×10^3
Contaminant, t_{c2}	1.0×10^{-4}	14	0.8×10^{-3}	1.08×10^3

the amplitude of the interface response due to alterations in the fluid composition of the saturated layer. It is clear that an increase in ion concentration has a larger effect on the interface response than changes in a combination of the dielectric permittivity, viscosity and fluid density. Even an increase in the salt concentration by 1.0×10^{-4} Mol L^{-1} shows a marked change in the radiation pattern. Due to the complex medium parameter dependency of seismoelectric conversions, it is possible that the combination of fluid chemistry alterations induced by the presence of a contaminant will, to some degree, cancel each other out, thereby reducing the overall amplitude change of the interface response. Furthermore, the ability to successfully detect these changes in the fluid properties of the aquifer would be dependent on the sensitivity of the recording instrumentation.

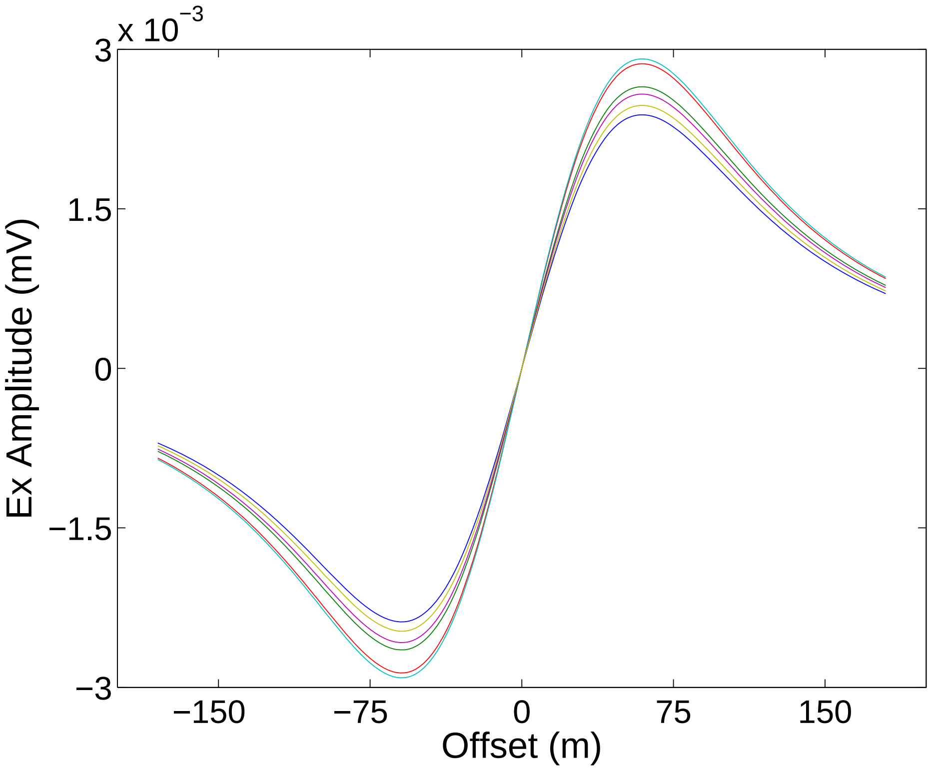

Figure 5-33: Variation of interface response due to the contamination of an aquifer. The five responses in increasing amplitude correspond to t_0 (blue), t_{c1} (yellow), t_{c2} (magenta), t_{s1} (green), t_{s2} (red), and t_{s3} (turquoise) of Table 5-2, respectively.

Chapter 6

Conclusions

We have applied the principle of flux-normalization to the seismoelectric system. The flux-normalized composition and decomposition matrices were implemented into a reflection formalism that characterized the wavefield at the receiver level of a horizontally layered medium as a function of an arbitrarily located source. By virtue of having flux-normalized the system, we were able to symbolically replace inverse operators with transpose operators. A second benefit of having derived a flux-normalized system was the ability to apply reciprocity theorems to one-way propagators.

Modelling of the seismoelectric system was found to be subject to problems of numerical instability. The numerical instability was a consequence of the inherently different scales of elastodynamic and electromagnetic wave propagation. Matrix operations on matrices containing the combined systems were subject to round-off errors due to the limited accuracy of double precision floating-point arithmetic. The errors accreted over the large volume of calculations that was required to numerically model the system, such that it was necessary to forego the implementation of the aforementioned transpose operators to improve stability.

In the modelling, we built up from a basic transmission model to a more complex three-layer geometry, with the presence of a free surface. We observed seismoelectric conversions occuring at the interfaces of our reflection model, such that each incident wavefield generated up to eight independently propagating wavefields. By virtue of having flux-normalized the system, we were able to apply reciprocity theorems to both the one-way and two-way wavefields, confirming that the recorded wavefields were invariant to a switch of the source and receiver types and locations. As expected, the amplitude of the interface response was highly dependent on the depth of the interface and could be approximated by a vertical electric dipole. The rapid decay in the amplitude of the interface response can be attributed to geometrical spreading of the electromagnetic field, a consequence of the receivers being positioned within the electromagnetic near field.

A P-wave source force simulates a spherically symmetric explosion and was used as an idealistic source function for further test geometries. A model of Vertical ElectroSeismic Profiling was implemented, allowing the receivers to be placed in near proximity to subsurface layers, thereby recovering a stronger seismoelectric conversion. As one suggested application of seismoelectrics has been for the monitoring of aquifers, we carried out simulations on the contamination of an aquifer. There was a clearly observable change in the interface response when the fluid properties of the underlying medium were changed. A small change in the ion concentration (e.g. salinity) of the aquifer caused a marked increase in the amplitude of the generated interface response.

Bibliography

Airy, G. B. "On the Phenomena of Newton's Rings when formed between two transparent Substances of different refractive Powers." *The London and Edinburgh Philosophical Magazine and Journal of Science* 2.VII (1833): 20–30.

Biot, M. A. "Theory of Propagation of Elastic Waves in a Fluid-Saturated Porous Solid. I. Low-Frequency Range." *The Journal of the Acoustical Society of America* 28.2 (1956): 168–178.

Boyce, W. E. and Di Prima, R. C. *Elementary differential equations and boundary value problems.* John Wiley & Sons, Inc., 1969.

Bracewell, R. N. *The Fourier Transform and its Applications.* McGraw-Hill, 1999, 3rd ed.

Carcione, J., Seriani, G., and Gei, D. "Acoustic and electromagnetic properties of soils saturated with salt water and NAPL." *Journal of Applied Geophysics* 52.4 (2003): 177–191.

De Ridder, S. A. L. *Simulation of Interferometric Seismo-electric Green's Function Recovery.* M.sc., Delft University of Technology, 2007.

De Ridder, S. A. L., Slob, E., and Wapenaar, C. P. A. "Interferometric seismoelectric Green's function representations." *Geophysical Journal International* 178.3 (2009): 1289–1304.

Deresiewicz, H. and Skalak, R. "On uniqueness in dynamic poroelasticity." *Bulletin of the Seismological Society of America* 53.4 (1963): 783–788.

Dupuis, J. C., Butler, K. E., and Kepic, A. W. "Seismoelectric imaging of the vadose zone of a sand aquifer." *Geophysics* 72.6 (2007): A81–A85.

Fokkema, J. T. and Ziolkowski, Anton. "The critical reflection theorem." *Geophysics* 52.7 (1987): 965–972.

Frasier, C. W. "Discrete Time Solution of Plane P-Sv Waves in a Plane Layered Medium." *Geophysics* 35.2 (1970): 197–219.

Frenkel, J. "On the theory of seismic and seismoelectric phenomena in a moist soil." *Physics* 3.5 (1944): 230–241.

Garambois, S. and Dietrich, M. "Seismoelectric wave conversions in porous media: Field measurements and transfer function analysis." *Geophysics* 66.5 (2001): 1417–1430.

———. "Full waveform numerical simulations of seismoelectromagnetic wave conversions in fluid-saturated stratified porous media." *Journal of Geophysical Research* 107.B7 (2002): 1–19.

Gentle, J. E. *Computational Statistics.* New York: Springer Science and Business Media, 2009.

Gharibi, M., Bentley, L. R., and Stewart, R. R. "Seismoelectric monitoring of producing oilfields : A review." Tech. Rep. 1994, CREWES, Calgary, 2003.

Griffiths, D. J. *Introduction to Electrodynamics.* New Jersey: Prentice-Hall, Inc., 1999, 3rd ed.

Haartsen, M. W. and Pride, S. R. "Electroseismic waves from point sources in layered media." *Journal of Geophysical Research* 102.B11 (1997): 24745–24769.

Haines, S. S. and Pride, S. R. "Seismoelectric numerical modeling on a grid." *Geophysics* 71.6 (2006): N57–N65.

Haines, S. S., Pride, S. R., Klemperer, S. L., and Biondi, B. "Seismoelectric imaging of shallow targets." *Geophysics* 72.2 (2007): G9–G20.

Hiemenz, P. C. and Rajagopalan, R. *Principles of colloid and surface chemistry.* New York: CRC Press, 1997, 3rd ed.

Hornbostel, S. C. and Thompson, A. H. "Waveform design for electroseismic exploration." *Geophysics* 72.2 (2007): Q1–Q10.

Johnson, D. L. "Scaling function for dynamic permeability in porous media." *Physical Review Letters* 63.5 (1989): 580–580.

Loseth, L. O., Pedersen, H. M., Ursin, B., Amundsen, L., and Ellingsrud, S. "Low-frequency electromagnetic fields in applied geophysics: Waves or diffusion?" *Geophysics* 71.4 (2006): W29–W40.

Lyklema, J. *Fundamentals of Interface and Colloid Science: Solid-Liquid Interfaces.* Academic Press, 1995.

Press, W. H., Teukolsky, S. A., Vetterling, W. T., and Flannery, B. P. *Numerical Recipes: The Art of Scientific Computing.* Hong Kong: Cambridge University Press, 2007, 3rd ed.

Pride, S. R. "Governing equations for the coupled electromagnetics and acoustics of porous media." *Physical Review B* 50.21 (1994): 678–696.

Pride, S. R. and Garambois, S. "The role of Biot slow waves in electroseismic wave phenomena." *The Journal of the Acoustical Society of America* 111.2 (2002): 697–706.

———. “Electroseismic Wave Theory of Frenkel and More Recent Developments.” *Journal of Engineering Mechanics* 131.9 (2005): 898–907.

Pride, S. R. and Haartsen, M. W. “Electroseismic wave properties.” *The Journal of the Acoustical Society of America* 100.3 (1996): 1301–1315.

Pride, S. R. and Morgan, F. D. “Electrokinetic dissipation induced by seismic waves.” *Geophysics* 56.7 (1991): 914–925.

Russell, R. D., Butler, K. E., Kepic, A. W., and Maxwell, M. “Seismoelectric exploration.” *The Leading Edge* 16.

Schoemaker, F. C. *Electrokinetic conversion*. Ph.d., Delft University of Technology, 2011.

Schoemaker, F. C., Grobbe, N., Schakel, M. D., De Ridder, S. A. L., and Slob, E. “Experimental Validation of the Electrokinetic Theory and Development of Seismoelectric Interferometry by Cross-Correlation.” *International Journal of Geophysics* Submitted.

Shaw, A. F. R. *The seismo-electric method and its sensitivity to subsurface contrasts*. Ph.d., Delft University of Technology, 2005.

Slob, E. “Interferometry by Deconvolution of Multicomponent Multioffset GPR Data.” *IEEE Transactions on Geoscience and Remote Sensing* 47.3 (2009): 828–838.

Sneddon, K. W., Olhoeft, G. R., and Powers, M. H. “Determining and Mapping DNAPL Saturation Values from Noninvasive GPR Measurements.” *Symposium on the Application of Geophysics to Engineering and Environmental Problems* : 293–302.

Thompson, A. H. and Gist, G. A. “Geophysical applications of electrokinetic conversion.” *The Leading Edge* 12.12 (1993): 1169–1173.

Thompson, R. R. “The seismic electric effect.” *Geophysics* 1.3 (1936): 327–335.

Ursin, B. “Review of elastic and electromagnetic wave propagation in horizontally layered media.” *Geophysics* 48.8 (1983): 1063–1081.

van der Burg, D. W. *Source Decomposition and Receiver Composition for Electro-Kinetic Measurements*. Ph.D. thesis, Delft University of Technology, 2002.

Wapenaar, C. P. A. “Reciprocity theorems for two-way and one-way wave vectors: A comparison.” *The Journal of the Acoustical Society of America* 100.6 (1996): 3508–3518.

———. “Reciprocity properties of one-way propagators.” *Geophysics* 63.4 (1998): 1795–1798.

———. “Reciprocity theorems for seismoelectric waves.” *Journal of Seismic Exploration* 12: 103–112.

Wapenaar, C. P. A. and Berkhout, A. J. *Elastic Wave Field Extrapolation*. Amsterdam: Elsevier, 1989.

Wapenaar, C. P. A., Dillen, M. W. P., and Fokkema, J. T. “Reciprocity theorems for electromagnetic or acoustic one-way wave fields in dissipative inhomogeneous media.” *Radio Science* 36.5 (2001): 851– 863.

Wapenaar, C. P. A. and Grimbergen, J. L. T. "Reciprocity theorems for one-way wavefields." *Geophysical Journal International* 127.1 (1996): 169–177.

Wenzlau, F. and Mueller, T. M. "Finite-difference modeling of wave propagation and diffusion in poroelastic media." *Geophysics* 74.4 (2009): T55–T66.